INFORMATION TO USERS

This manuscript has been reproduced from the microfilm master. UMI films the text directly from the original or copy submitted. Thus, some thesis and dissertation copies are in typewriter face, while others may be from any type of computer printer.

The quality of this reproduction is dependent upon the quality of the copy submitted. Broken or indistinct print, colored or poor quality illustrations and photographs, print bleedthrough, substandard margins, and improper alignment can adversely affect reproduction.

In the unlikely event that the author did not send UMI a complete manuscript and there are missing pages, these will be noted. Also, if unauthorized copyright material had to be removed, a note will indicate the deletion.

Oversize materials (e.g., maps, drawings, charts) are reproduced by sectioning the original, beginning at the upper left-hand corner and continuing from left to right in equal sections with small overlaps. Each original is also photographed in one exposure and is included in reduced form at the back of the book.

Photographs included in the original manuscript have been reproduced xerographically in this copy. Higher quality 6" x 9" black and white photographic prints are available for any photographs or illustrations appearing in this copy for an additional charge. Contact UMI directly to order.

UMI

A Bell & Howell Information Company
300 North Zeeb Road, Ann Arbor MI 48106-1346 USA
313/761-4700 800/521-0600

Control of Flexible-Link Manipulator

Sicheng Yu ©

November 20, 1997

This thesis is accepted Natarajan. K

A THESIS SUBMITTED IN PARTIAL FULFILLMENT OF THE
REQUIREMENTS OF THE M.Sc.Eng. DEGREE
IN
CONTROL ENGINEERING
FACULTY OF ENGINEERING
LAKEHEAD UNIVERSITY
THUNDER BAY, ONTARIO
CANADA

ABSTRACT

Flexible-link manipulator has many advantages over classic rigid body manipulator in industrial and space applications. However, it also poses high requirements on controller design, to ensure the accurate tip position tracking and suppression of tip deflection/vibration.

This thesis sets up the model, both linear sections and nonlinear sections, for a typical apparatus. It discusses, by simulations and experiments, the solutions for these control problems. PD controller plus conditional I control is found effective on rigid body tracking control, and P controller with second-order lowpass filter proves effective on the suppression of deflection/vibration. Optimized PIDP controllers are experimentally implemented and the system performances are shown.

Further this thesis discusses a LQR controller which uses a ninth-order full state feedback. Experimental results using the LQR controllers show an improvement over the PIDP controller, particularly in the suppression of flexible beam deflection.

OVERVIEW OF THESIS

Chapter 1 has a comparative study of previous literature on this topic after introduction of the flexible-link manipulator. Chapter 2 introduces the experimental setup for this thesis and builds its linear/nonlinear model. In Chapter 3 further exploration is undertaken to search for an optimal PIDP controller and corresponding experimental results are given. Chapter 4 discusses LQR controller as a straight derivation and improvement on PIDP controller in Chapter 3. Also Variable Structure Sliding Mode Control (VSSMC) is explored briefly in this chapter. Finally in Chapter 5 the work is summarized and suggestions for future work are presented.

ACKNOWLEDGMENTS

I gratefully dedicate this work to my supervisor Dr. K. Natarajan for his support and guidance. This work would have proved impossible without his extensive knowledge and responsible supervision. I would also like to thank my Co-supervisor Dr. F. Karray for suggesting the area of research and early guidance.

This work owes a lot to the efforts of many former researchers. Thanks are also due to my classmate, Mr. O. Sobieraj, for his encouragement and discussion.

Contents

List of Figures

Chapter 1

Overview of Topic

This chapter introduces flexible-link manipulator control and describes problems faced. A literature survey to display work done already and to expose questions not yet explored in this area is provided. At the end of this chapter, an overview of the thesis is outlined.

1.1 Flexible-link Manipulators

Today's robots share a common feature of being bulky. Such robots have several drawbacks: they operate at low speed; they have low payload-to-weight ratio and high energy consumption. These drawbacks cause poor productivity and efficiency. Growing number of space and technical applications call for lighter, smarter robots. The advantages of such lightweight manipulators include faster response, lower energy consumption, smaller actuators, trimmer mechanical design and lower transportation costs. To satisfy such performance requirements, robots must be built ever lighter, and this will eventually lead to flexibility of links.

Controller design solutions to minimize the effects of the elastic (flexible body) displacements in light robots are highly demanded in the industrial and/or space applications which require accurate trajectory control. This thesis discusses some

solutions to the problem of single flexible link manipulator control. It evaluates controllers by experimental implementation on a flexible-link apparatus built at Lakehead University.

Figure 1-1 shows the coordinates adopted for the flexible link manipulator.

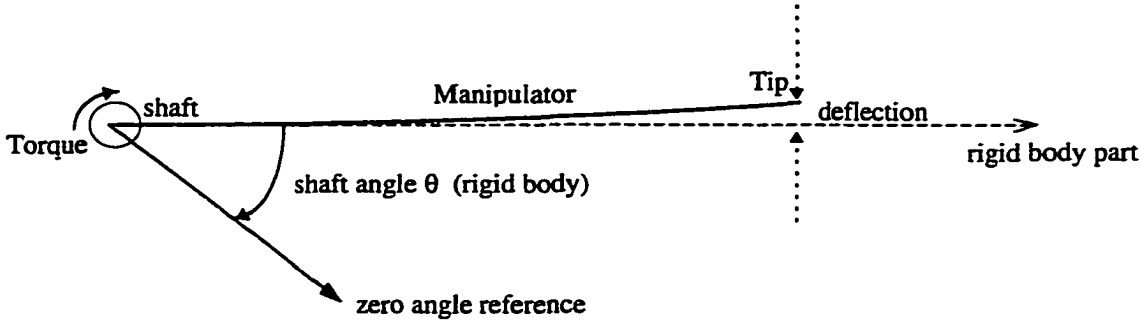

Figure 1-1 Coordinates of flexible-link manipulator

1.2 Problem Description

Flexible lightweight robots, though having a series of potential advantages over the conventional rigid robots, have posed more stringent requirements on their control systems. The problems to be solved and their causes include:

1. The bending of a flexible beam, which makes accurate position control of the tip difficult. There are highly vibratory poles with low damping factors in the process (plant) transfer function. From a system point of view flexing manifests itself through these vibratory poles (closely packed lightly damped modes).

2. When flexible-link manipulators carry payloads which are unknown or varying, the controllers need to be tuned to maintain endpoint accuracy and performance.

3. In a single-link flexible robot arm, the sensors and actuators are located at different points of the arm. They are thus noncollocated, such kinds of systems are difficult to stabilize and control, and the attainable performance is limited [2].

1.3 Literature Survey

At present, studies in the modeling and control of flexible-link manipulators have reached a high level of maturity. This is due primarily to numerous works in the last four years from a theoretical viewpoint and due to numerous works in the last decade from a simulation viewpoint and to a lesser extent experimental evaluation. Theoretical studies in modeling flexible-link robots abound. Some key references are found in [1]. Most of them consider beam models, however, the composite actuator-beam model is different from such beam models.

Equally numerous are the various approaches that have appeared in the literature for controller designs [2,3,4,5,6,7]. A great number of these works have dealt with simulation studies only, and some have developed quite elaborate and complex control schemes [7].

On the other hand several basic laboratory setups have demonstrated the effectiveness and ineffectiveness of relatively simple algorithms for flexible manipulator control. While most experimental studies have focused on single-link manipulators, or multilink manipulators with a single flexible link, such setups have served as valuable testbeds for modeling, system identification, and controller design. Some of the most visible experimental efforts have been in the work of Yurkovich et al. [9,10,11,12,14], Schmitz and Canon [2, 19], Franklin[20], Book et al. [21, 22] and several others. In [3], the use of measurements from a linear accelerometer for use in vibration compensation of the robot endpoint was shown to be extremely successful, proving the concepts of acceleration feedback for flexible-link manipulator control. The use of acceleration feedback has appeal from an engineering design viewpoint, due to its ease of implementation, relatively low cost, and advantages of structure-mounted sensing.

Other simulation and experimental studies on nonadaptive controller designs were done, by W. T. Qian and C. C. H. Ma [6]; Robert H. Cannon, and Eric Schmitz [2]; Y. Aoustin, C. Chevallereau, A. Glumineau and C. H. Moog [4]. Controllers investigated in their work include: Proportional & Derivative Control (PD), Variable Structure Sliding Mode Control (VSSMC), Linear Quadratic Gaussian (LQG), Linear Quadratic Regulator (LQR), Singular Perturbation Method (SPM) etc.. Their results reveal that simpler controllers, like PD and LQG, have more promise than complicated controllers like VSSMC in the case of flexible-structure control [2, 4, 6]. Also Singular Perturbation Method is proved to be effective particularly on trajectory tracking [4]. Relatively slow system response is a main drawback of these results.

System identification studies have also been carried out on the flexible link manipulator. Besides the traditional time domain and frequency domain system identification methods, S. Yurkovich and A. P. Tzes pioneered a new method [10,11,12], called Time-varying Transfer Function Estimation (TTFE) developed for identification in the frequency domain. TTFE updates the frequency components in the time domain through recursive adaptation algorithm, such as recursive least squares or least mean squares. The adjacent frequency components need not necessarily be independent, so that a smoothing of the transfer function is realized [12]. The main conclusion of their work [10] is that, schemes based on time domain estimation methods are not particularly well-suited for estimation in flexible structure systems, primarily due to characteristics of lightly damped, closely-packed modes, the presence of unmodeled high frequency components and requirements of fast sampling.

Broadly the previous literature on flexible link control can be summarized in Figure 1-2:

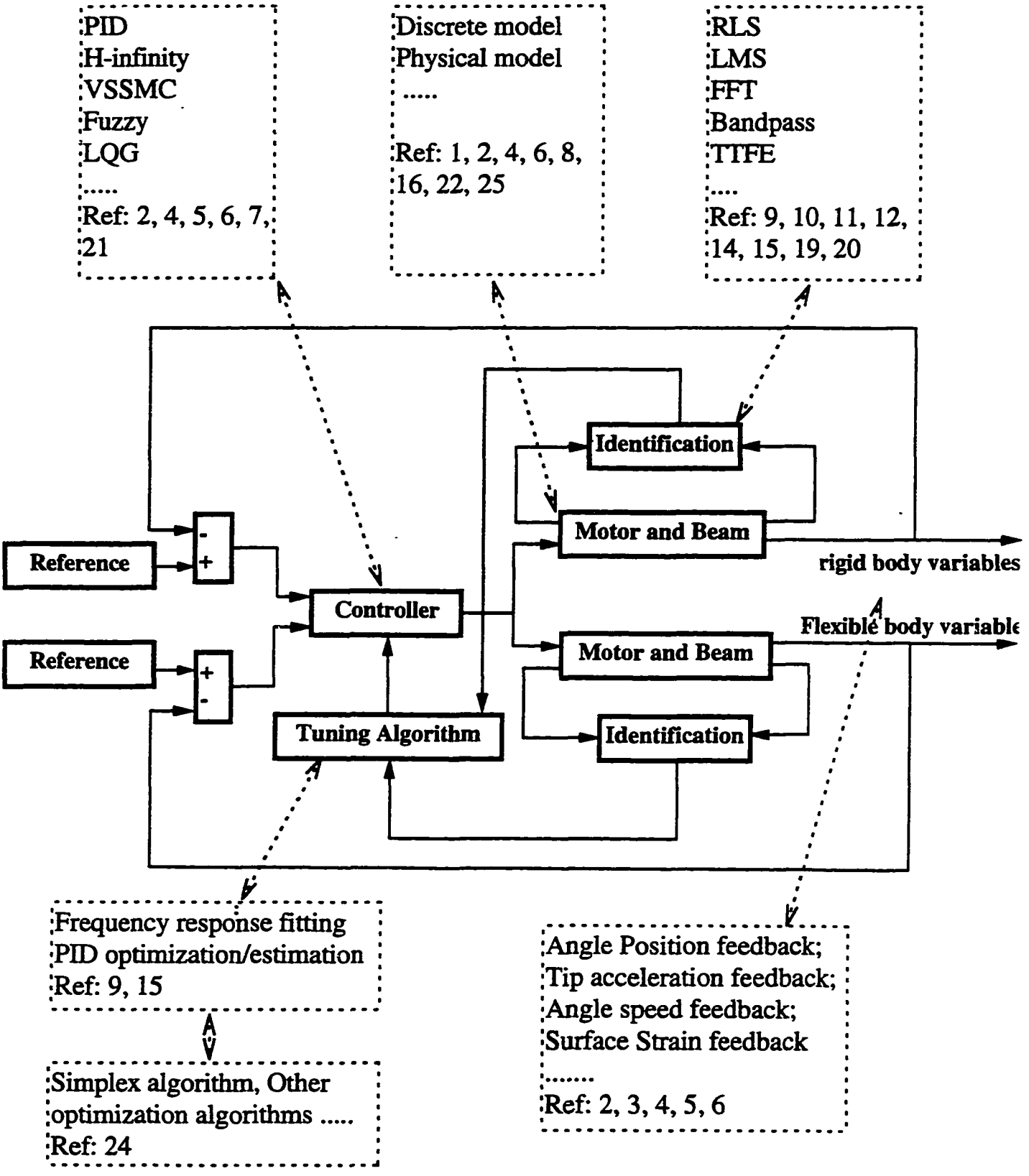

Figure 1-2 Literature survey in control of flexible-link manipulator

1.4 Overview of Thesis

Despite the work in the literature, experimental results on flexible link control are far from satisfactory in the following aspects:

1. Most work done in the literature is by simulation. Experimental work has to be done, in order to verify these models and controller designs, to take into account constraints on the controller effort and nonlinear effects such as friction and backlash, to provide more accurate control of tip position, faster speed of system response and better control of beam oscillations and deflection

2. Nonlinear sections in the flexible-link manipulator system, like friction and gear hitting due to backlash, significantly influence system behavior, models for this nonlinear sections are absent in literature.

3. Slow system response is a common drawback of the experimental results shown in previous literature. More effective controllers for trajectory tracking and deflection/vibration suppression are still in demand.

4. Most literature has reported work on single aspects of the control problem, while little effort has been spent on assembling these into a coherent optimal combination.

Some of these aspects will be studied experimentally in this thesis.

Chapter 2

Experimental Setup and System Modeling

In this chapter, an apparatus built at Lakehead University for flexible-link manipulator research is described. Its model (both linear and nonlinear part) is obtained experimentally. Also the methods used to obtain this model from experimental data are presented.

Later in this chapter, how the model parameters change when manipulator carries various payloads is studied.

2.1 Experimental setup

An apparatus was built at Lakehead University for flexible-link manipulator control [8]. Figure 2-1 shows the experimental setup.

The arm is constructed from 6061-T6 aluminum-magnesium-silicon alloy. This is a balanced alloy composed of 1.5% Mg_2Si, 0.25% Cu and 0.25% Cr. The alloy contains additions of magnesium and silicon, which in the heat treated and aged condition precipitate Mg_2Si as a hardening phase. It is an intermediate strength, general purpose structural alloy and is among the most important alloys ever developed [17]. The chromium and copper add increased strength to the aluminum-magnesium-silicon alloy.

The beam is 1m long, 51mm wide and 3mm thick, and has a compensating weight to balance its rotation about the shaft. The flexibility of this manipulator is greater than flexibility in current industrial robots.

The only control input available is the motor torque at the single rotating joint. The applied torque is proportional to the motor current which is controlled. A power electronic amplifier converts command inputs from computer to motor current. Current magnitude and direction control blocks are separately implemented inside the power amplifier. The computer interfaces to the power amplifier (through two different channels of a D/A card) with voltage information for magnitude of motor current and a logic level (high or low) for current direction.

The servo motor used has an integral tachometer on its shaft to measure angle speed. Besides, direct measurement of shaft angle position via a potentiometer on the top of the shaft (Figure 2-1) is available. A set of four strain gauges [18] measure the surface strain on the base (hereafter called "base strain gauge"). A similar set of strain gauges measure the strain at approximately the middle of arm (hereafter called "second strain gauge"). These four signals, namely angle position, angle speed, base & 2nd strain, are signal-processed and are acquired by the computer in the form of digital information through a multiplexed A/D converter.

The computer used to control this arm is a Pentium 166 running Windows 95. The A/D & D/A card is a Keithley MetraByte™ model DAS-1600, which has 2 output channels and 8 bipolar input channels, with 12-bit resolution. The card can handle a maximum sampling rate of 6 k samples/second.

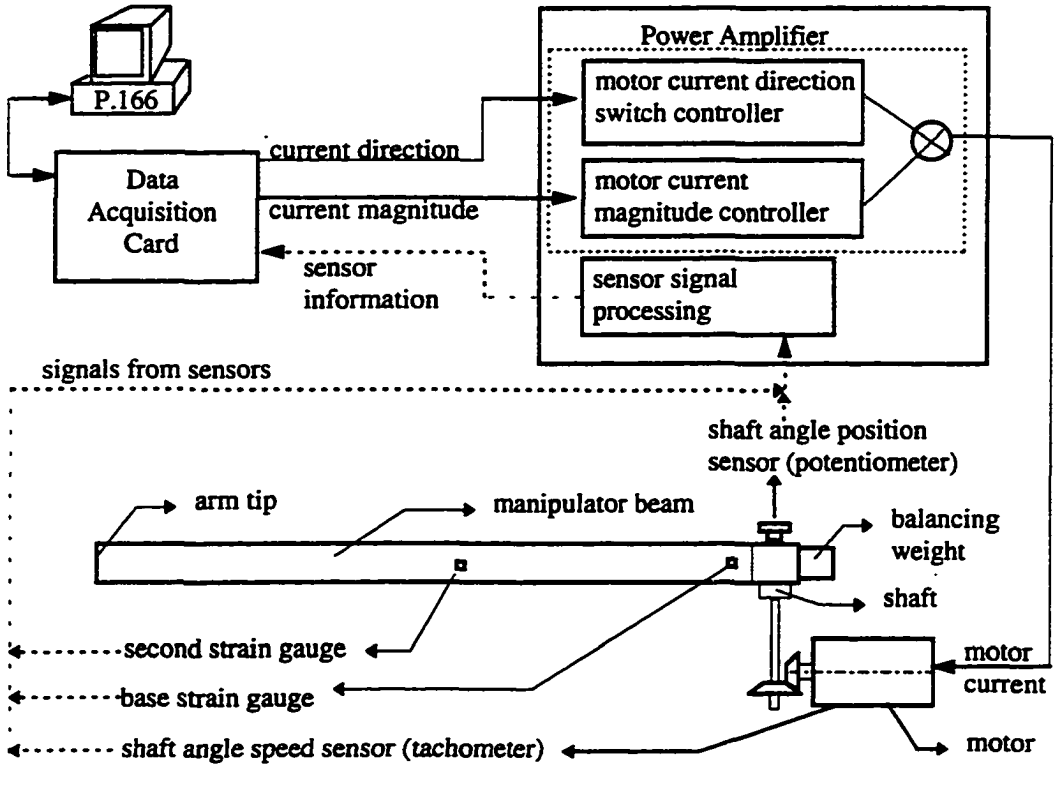

Figure 2-1 Experimental setup

Inside the power amplifier, the motor current control circuit schematic is as follows: (D_1 D_2 D_3 are MOSFET drawer boards)

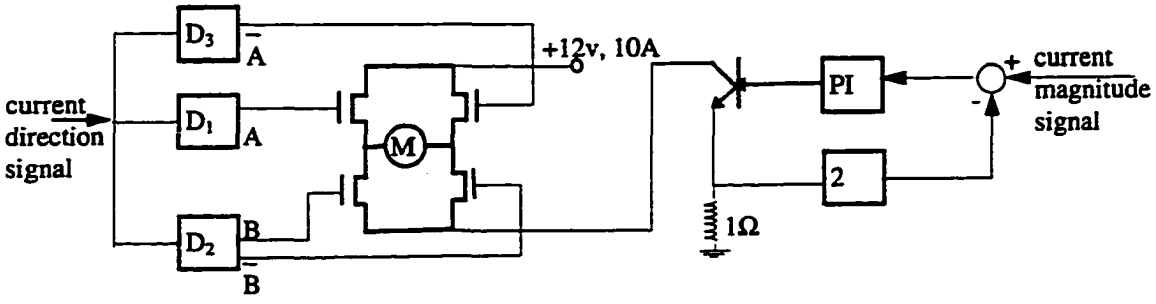

Figure 2-2 Circuits for motor current control

The circuit to process strain gauge sensor signals is an electrical bridge as follows: (R. R+ are strain gauges)

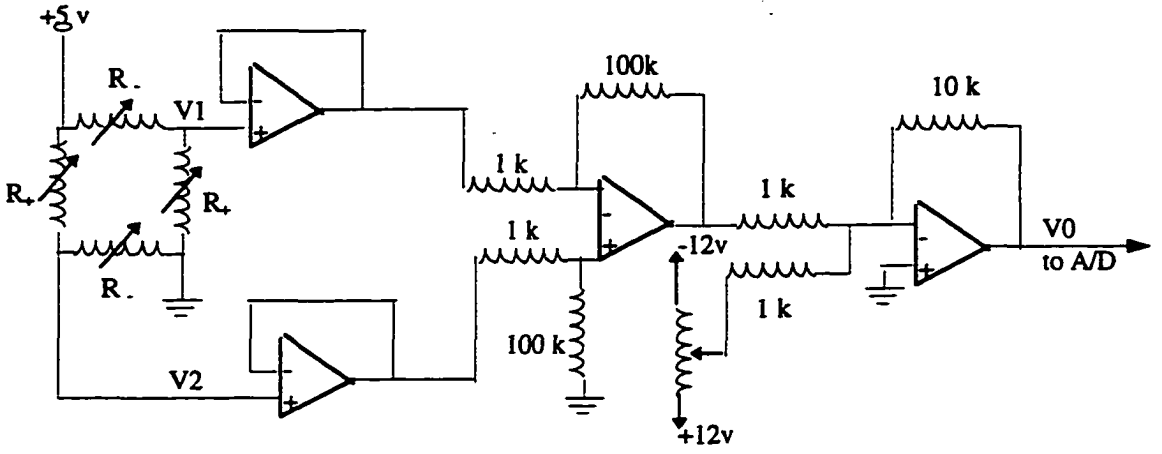

Figure 2-3 Strain gauge signal processing

The circuit to process tachometer output (measuring speed) and potentiometer measuring shaft angle are as follows:

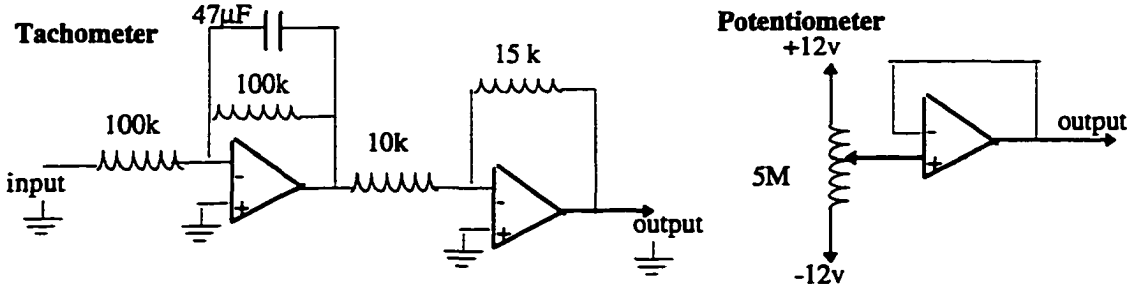

Figure 2-4 Tachometer and pot signal processing

2.2. Modeling

Model of above apparatus may be derived from physical principles with subsequent parameter identification, or it can be obtained experimentally. Models based on physical principles have been derived in the references [4, 5, 6].

In this chapter, both the linear and nonlinear part of system model are obtained experimentally. The schematic of entire system is shown in Figure 2-5:

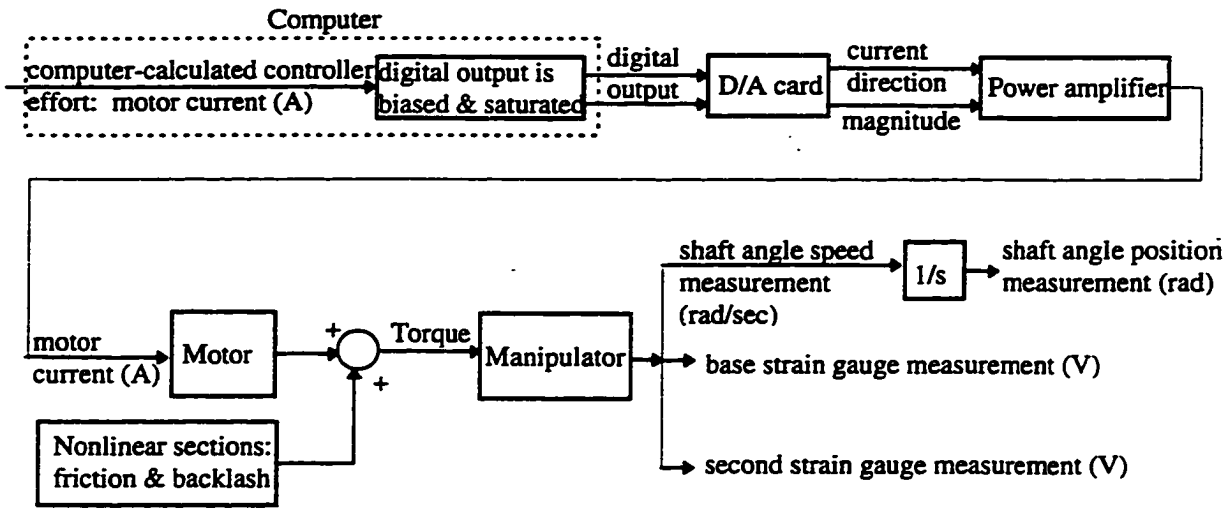

Figure 2-5 Schematic of the flexible-link manipulator system

With reference to Figure 2-5, a mathematical model relating measurements, controller effort and system state space is represented by Equation (2-1):

output (measurements)
$$Y = \begin{bmatrix} y_1 \\ y_2 \\ y_3 \end{bmatrix} = Y_L + Y_N$$

linear part:
$$Y_L = \begin{bmatrix} G_R \\ G_2 \\ G_3 \end{bmatrix} * u = G_L * u$$

nonlinear part:
$$Y_N = G_N(X) \qquad (2\text{-}1)$$

In Equation (2-1), Y is a 3-element output (measurements) consisting of:

y_1 : the rigid body displacement (shaft angle measurement),
y_2 : the base strain gauge measurement,
y_3 : the second strain gauge measurement.
and
X : the system state vector.
u : the motor current reference signal.

The goal of controlling the flexible-link manipulator is to drive y_1 in the commanded trajectory and, to ensure that y_2 and y_3 are adequately zeroed (to ensure that the arm is straight).

The total effective controller effort applied on manipulator consists of torque applied by DC motor along with the effects due to nonlinear friction and gear backlash. Thus the output of system (Y) is comprised of two parts: linear part (Y_L) and nonlinear effects (Y_N), as stated in the first part of Equation (2-1).

The second part of Equation (2-1) presents the model's linear part G_L: relationship between motor current reference u and linear part of the system output Y_L. The three elements of the transfer function matrix G_L are:

G_R : transfer function from effort u to shaft angle position measurement (rigid body)
G_2 : transfer function from effort u to base strain gauge measurement
G_3 : transfer function from effort u to second strain gauge measurement

The third part of Equation (2-1) presents the model's nonlinear part G_N: the cause of system nonlinear effects Y_N, where X represents the state space of the system. (the manipulator position and velocity will influence magnitude of gear hitting momentum due to backlash.)

The model's linear part G_L (G_R G_2 and G_3) is first obtained experimentally in this chapter with the nonlinear part G_N presented later in this chapter.

The methods to obtain G_R G_2 and G_3 are theoretically similar: frequency response of G_R G_2 and G_3 are identified experimentally using bandpass filter method [15]. They are fitted with linear transfer functions of assumed order with unknown parameters. The unknown parameters are obtained by minimizing the error between the fitted and measured frequency response points in a least square sense using a polytope search method [24].

Following sections will report on G_R, G_2 and G_3, and G_N one by one. Also how payloads influence model parameters are then discussed.

2.2.1 Modeling of Rigid Body (G_R) With and Without Payload

This section experimentally obtains G_R : transfer function from motor current u to shaft angle position measurement. Figure 2-6 is the schematic used for acquiring the response of rigid body model. It is a closed-loop system with a PD controller.

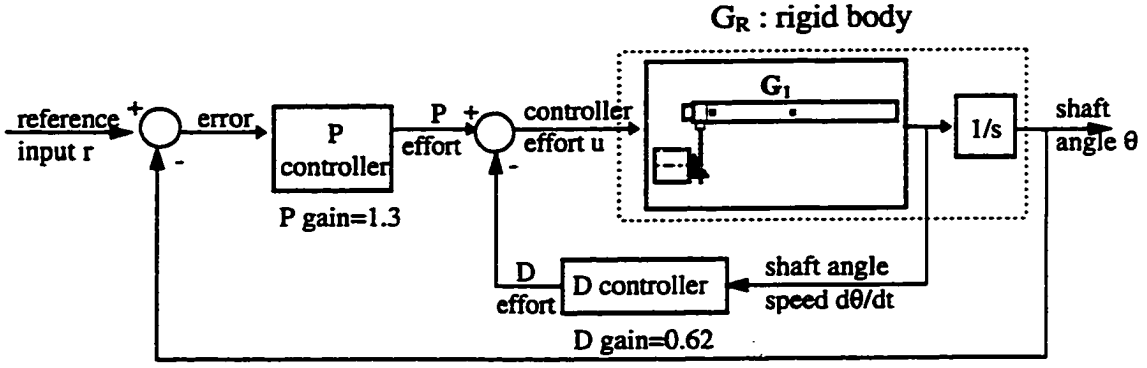

Figure 2-6 Diagram used for closed-loop model identification

Note that G_I in the above figure is the transfer function from controller effort u to shaft angle speed, its relationship with G_R (rigid body) is:

$$G_R = G_I * \frac{1}{s} \qquad (2\text{-}2)$$

Once G_I is obtained, G_R can be derived from Equation (2-2).

The applied reference input r is four periods of square wave with 10s period. The slew (r) is 100°. The period is selected to ensure that the system settles before the next bump is applied. P gain used is 1.3 (A/rad) and D gain is 0.62 (A*sec/rad). System A/D sampling rate is 333 samples/second (3ms period).

Experimentally measured data includes: shaft speed dθ/dt (rad/sec), shaft angle position θ (rad), reference input r (rad) and controller effort u (A). Calculated data includes: error (rad), P effort (A) and D effort (A).

Based on the recorded data in the time-domain, the bandpass filter method [15] is applied off-line to obtain system frequency responses: firstly every frequency component of both input and output signals is filtered out by bandpass filter, then the amplitude & phase value of frequency response from input to output is calculated by comparing the frequency component at both sides using RLS. In Figure 2-6, the frequency response from r to θ, and from u to dθ/dt at harmonics of the excitation input are obtained with this method.

G_l transfer function is experimentally identified by fitting the frequency response from u to $d\theta/dt$. The steps taken to obtain the rigid body transfer function thus are:

Algorithm I:

1. Experimentally measure and record the data in a digital computer with a sampling rate (100 samples/second) which is at least 20 times greater than the bandwidth of the excitation loop;

2. Obtain frequency response from P effort to $d\theta/dt$ (G_a), and frequency response from r to θ (G_b) (Figure 2-6) using bandpass filter method. Note that G_a and G_b are vectors containing complex numbers (amplitude and phase information) at each excitation harmonics;

3. Analytically calculate frequency response from controller effort u to $d\theta/dt$ (G_c) based on G_a obtained in step 2;

4. Fit transfer function G_l to frequency response G_c;

5. Based on G_l, calculate closed-loop transfer function T, and confirm the frequency response with G_b;

Before fitting G_l's linear transfer function, its order is determined. Standard models treat transfer function from torque command to shaft speed as a first-order linear system. However in the present case, the flexibility effects of the beam has to be taken into account on the rigid body motion. As a result, a second-order structure for G_l is fitted, as shown below:

$$G_l = \frac{b_1}{a_1 s^2 + a_2 s + a_3} \qquad (2\text{-}3)$$

The advantages of using second-order structure instead of first-order can be seen in the following experimental results (Figure 2-7), particularly in the accuracy of the phase fitting.

The coefficients b_l a_1 a_2 a_3 in Equation (2-3) are obtained by using the Nelder-Mead [24] optimization method to fit G_l transfer function with experimentally identified frequency response G_c. The optimized second-order transfer function so determined is:

$$G_l = \frac{9.5097}{s^2 + 4.6645s + 4.2001} \qquad (2\text{-}4)$$

and G_R is:

$$G_R = G_1 * \frac{1}{s} = \frac{9.5097}{s^3 + 4.6645s^2 + 4.2001s} \quad (2\text{-}5)$$

If G_1 is chosen as first-order transfer function, then the best fit is:

$$G_1 = \frac{2.0817}{s + 0.8746} \quad (2\text{-}6)$$

The fit of these two transfer functions for G_1 (Equation 2-4, 2-6) along with experimental data are shown in Figure 2-7:

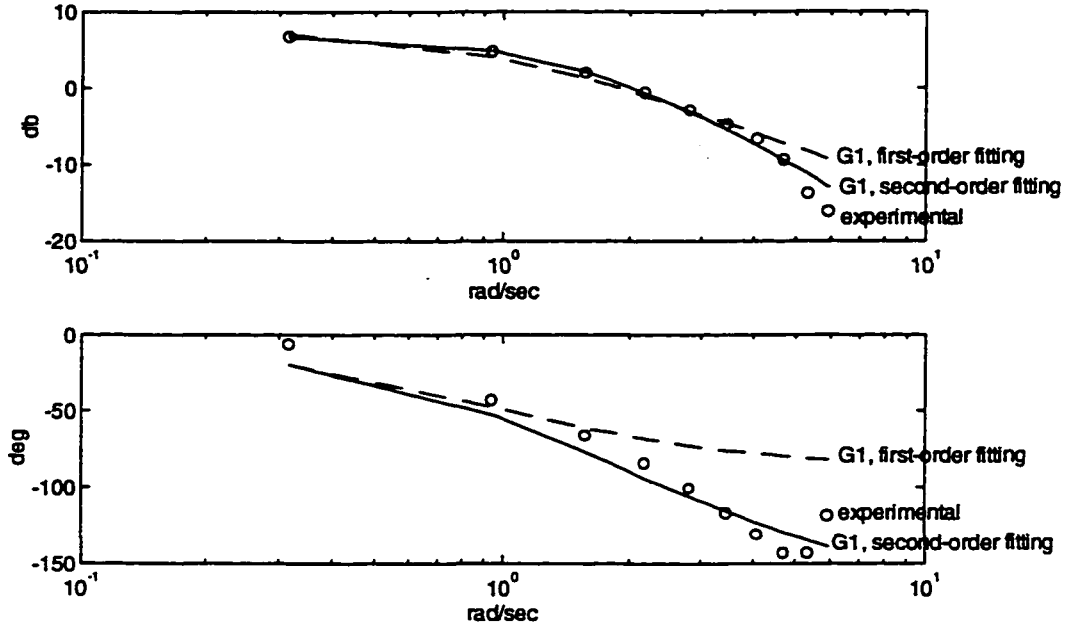

Figure 2-7 First-order (--) and second-order (-) transfer function fitting with experimental results (o)

The second-order transfer function fits the experimental data better than the first-order transfer function. In the identification of G_1 under varying payloads, second-order structure will henceforth be used.

Equation (2-5) is regarded hereafter as the rigid body transfer function.

Additionally, three methods to confirm the predictive ability of this model is provided below.

Firstly, the integration of shaft speed measurement with shaft angle position measurement is shown in Figure 2-8. They match each other well. We thus have confidence about the integral relationship shown in Figure 2-6.

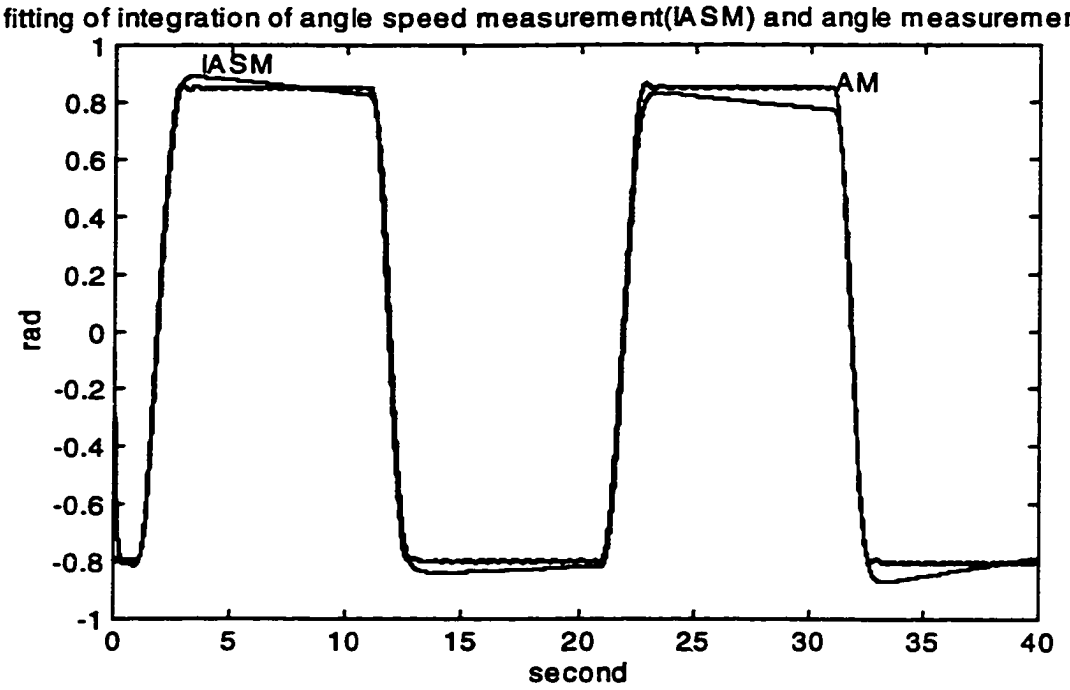

Figure 2-8 Matching of shaft angle speed measurement's integration and shaft angle position measurement

Secondly, experimentally identified G_b (Algorithm I) is compared with calculated closed-loop frequency response based on G_R from Equation (2-5), using the identical P gain(1.3) D gain(0.62) and schematic (Figure 2-6) as applied in experiment. The fit is shown in Figure 2-9:

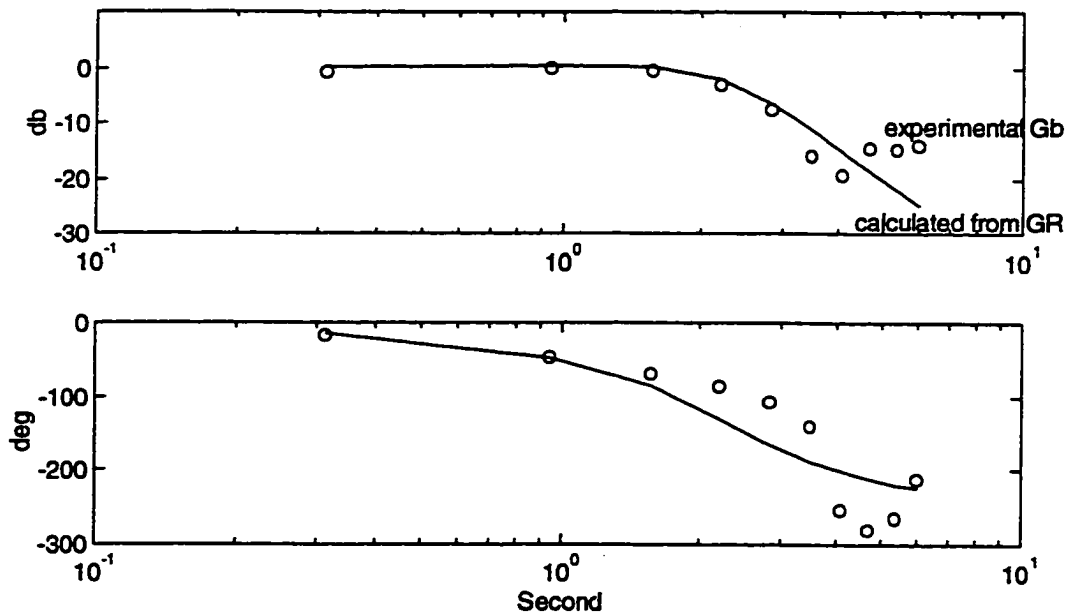

Figure 2-9 Confirming experimental closed-loop frequency response(o) and calculated one(-) based on G_R obtained

Thirdly, closed-loop time-domain response obtained by simulation using G_R and experimental time-domain closed-loop response, with identical controller gain settings (P gain is 1.3 and D gain is 0.62 as in Figure 2-6), are compared in Figure 2-10. A step reference input of 100 degree is applied:

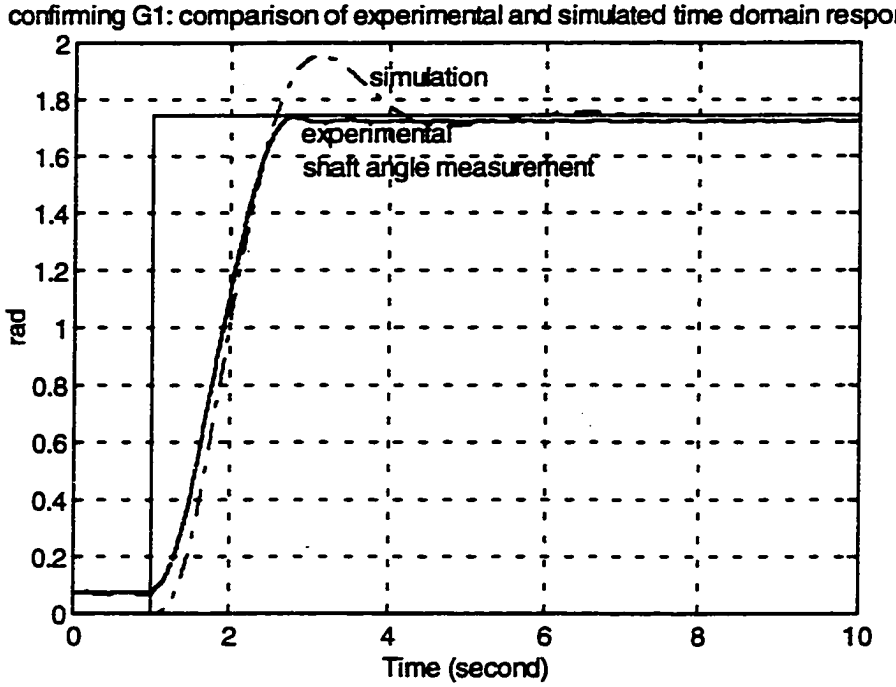

Figure 2-10 Confirming of experimental and simulated time domain response

The two curves match well, except the experimental result doesn't have the 10% overshoot as the simulation does. This mismatch is caused by friction between beam and shaft shoulder. After the nonlinear models are considered (later in this chapter), this mismatch will disappear, and a very close overlapping between the experimental and simulated response can be seen in Figure 2-26.

Models of the rigid body with various payloads are next identified. Different payloads are mounted on the tip of manipulator and system performance is experimentally observed and recorded. The new models with payloads are obtained, using the same procedures (Algorithm I) described earlier to identify the model without payload.

With a payload of 75g, the rigid body transfer function G_1 is:

$$G_1 = \frac{5.6070}{s^2 + 3.5981s + 4.1295} \qquad (2\text{-}7)$$

and its frequency response is:

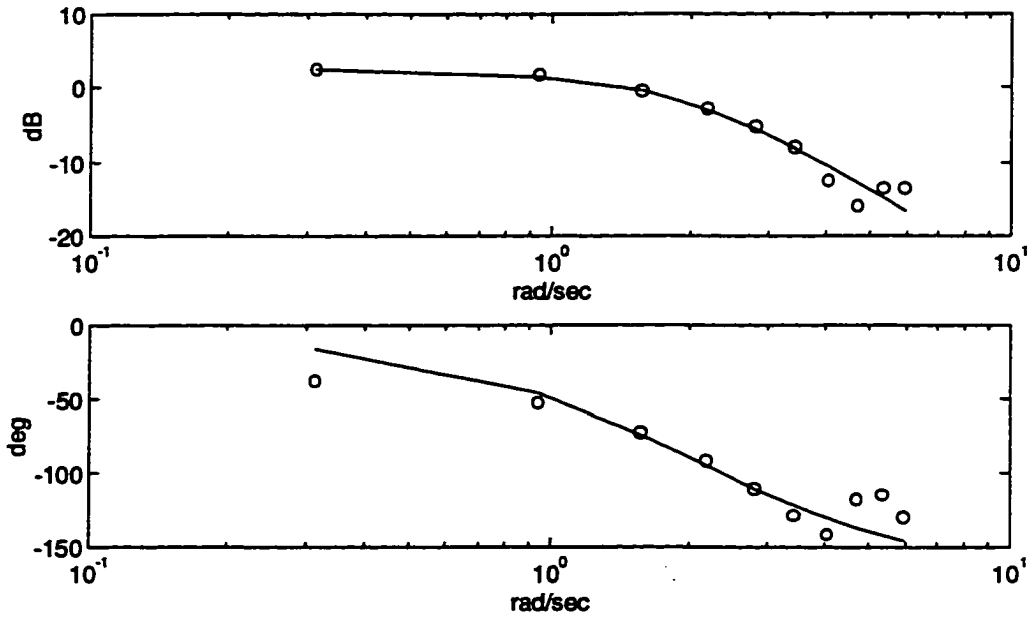

Figure 2-11 G_1 second-order transfer function fitting, with a payload of 75g

With a payload of 150g, the rigid body transfer function G_1 is:

$$G_1 = \frac{3.9938}{s^2 + 3.1329s + 3.6671} \qquad (2\text{-}8)$$

and its frequency response is:

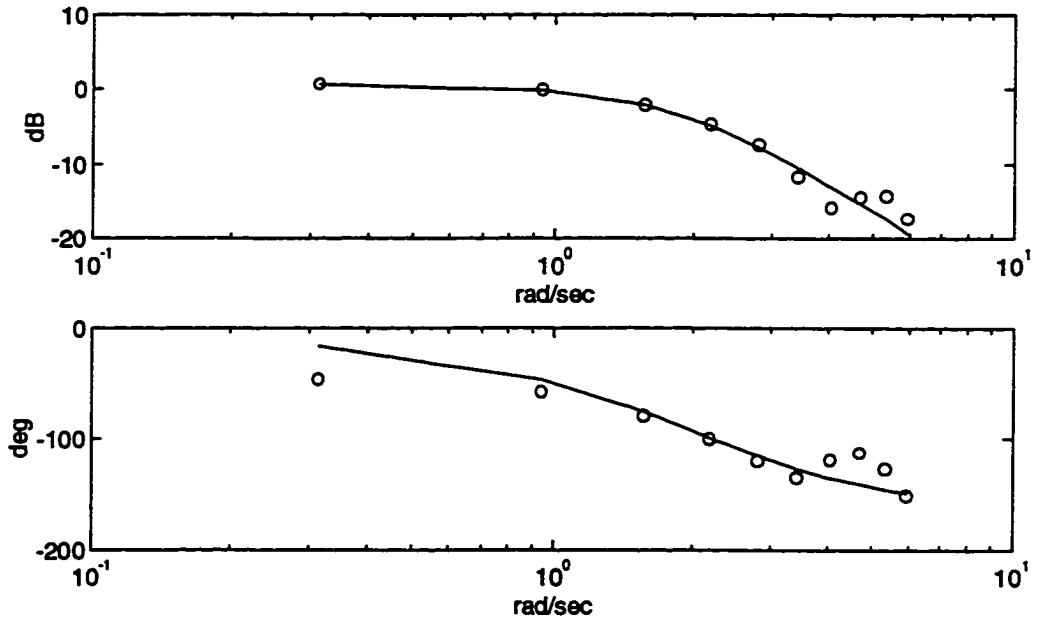

Figure 2-12 G_1 second-order transfer function fitting, with a payload of 150g

With a payload of 380g, the rigid body transfer function G_1 is:

$$G_1 = \frac{1.0463}{s^2 + 1.5837s + 1.7737} \qquad (2\text{-}9)$$

and its frequency response is:

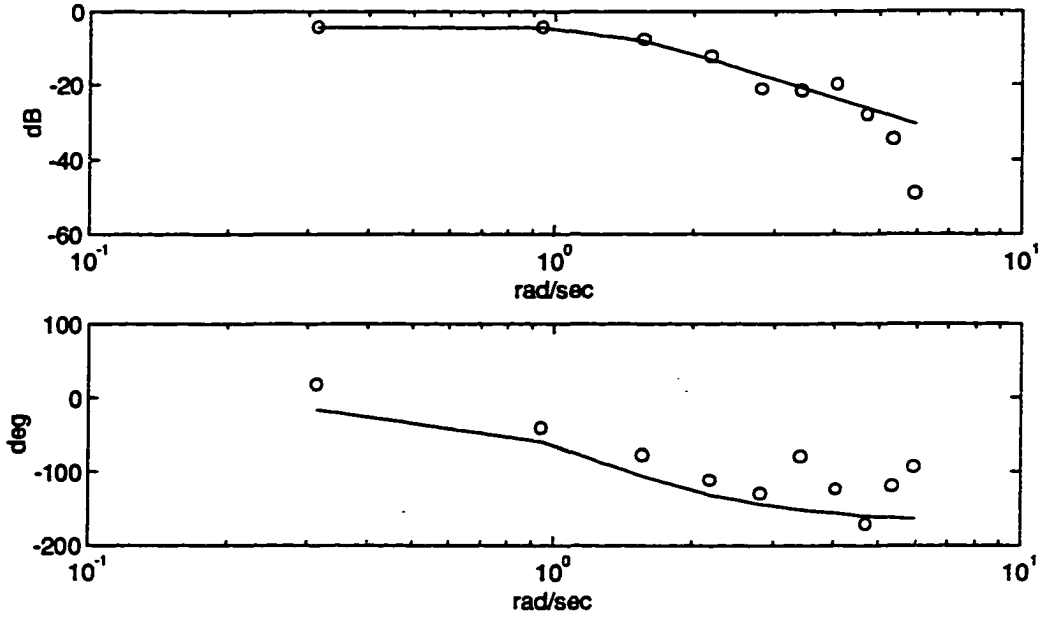

Figure 2-13 G_1 second-order transfer function fitting, with a payload of 380g

Equation 2-4, 2-5, 2-7, 2-8, 2-9 are the results of this section, they will be compared in Section 2.2.4 and conclusions concerning the system model will be drawn.

2.2.2 Modeling of Beam Deflection With and Without Payloads

Strain gauge measurements reflect information on beam deflection/vibration. The goal of this section is to experimentally obtain G_2 and G_3 (Equation 2-1), which are transfer functions from controller effort u to base and second strain gauge measurement respectively. Following Cannon [2], the general model from controller effort to strain gauge measurements on the flexible-link manipulator is taken to be comprised of second-order transfer functions:

$$\sum_{i=1}^{\infty} \frac{A_i \omega_i^2}{s^2 + 2\xi_i \omega_i s + \omega_i^2} \qquad (2\text{-}10)$$

where ω_i is the resonant frequency of i^{th} mode and A_i and ξ_i are the magnitude and damping factor of this mode respectively.

In this section, Equation (2-10) is used as the structural model for G_2 and G_3, and parameters of Equation (2-10) are identified experimentally. Only the modes that are adequately measurable are paid attention.

The methods to obtain G_2 and G_3 are technically the same as that for the case of rigid body model identification, except that frequency responses of G_2 and G_3 are obtained more delicately.

The steps taken to experimentally obtain G_2 and G_3 are:

Algorithm II:

1. Feed in a pure sinusoidal current reference to the motor (current controller), of known amplitude (4A) and frequency;

2. Record four periods of strain gauge output with sampling period of 3ms, use bandpass filter to extract its harmonic at the input frequency, calculate the frequency response (amplitude and phase) at this frequency [15]. (Note that system response is nonlinear, and has harmonics different from input frequency, hence the need for bandpass filtering.)

3. Sweep over frequency range of sinusoidal wave by repeating step 2 on all useful frequency points. The frequency range swept through for identification is [0.5 60] Hz.

4. From the magnitude plot of the frequency response, determine ω_i of the modes by observing peaks, and fit the plot with transfer functions in the form of Equation 2-10. Parameters in Equation 2-10 are identified by the means of optimized fitting as before (Algorithm I);

5. Confirm the transfer function obtained by computing step response from the transfer function and comparing it with experiment.

Following four subsections apply the above steps to obtain G_2 without and with payload, and then G_3 without and with payload respectively.

2.2.2.1 G_2 (Base Strain Gauge) Transfer function Without Payload

Without payload on the arm tip, three oscillation modes, respectively at 8.5 Hz, 22 Hz and 46 Hz, can be observed within swept frequency range.

Figure 2-14 shows the experimentally measured frequency response from motor current input to base strain gauge measurement and, its optimized fitting (Equation 2-11):

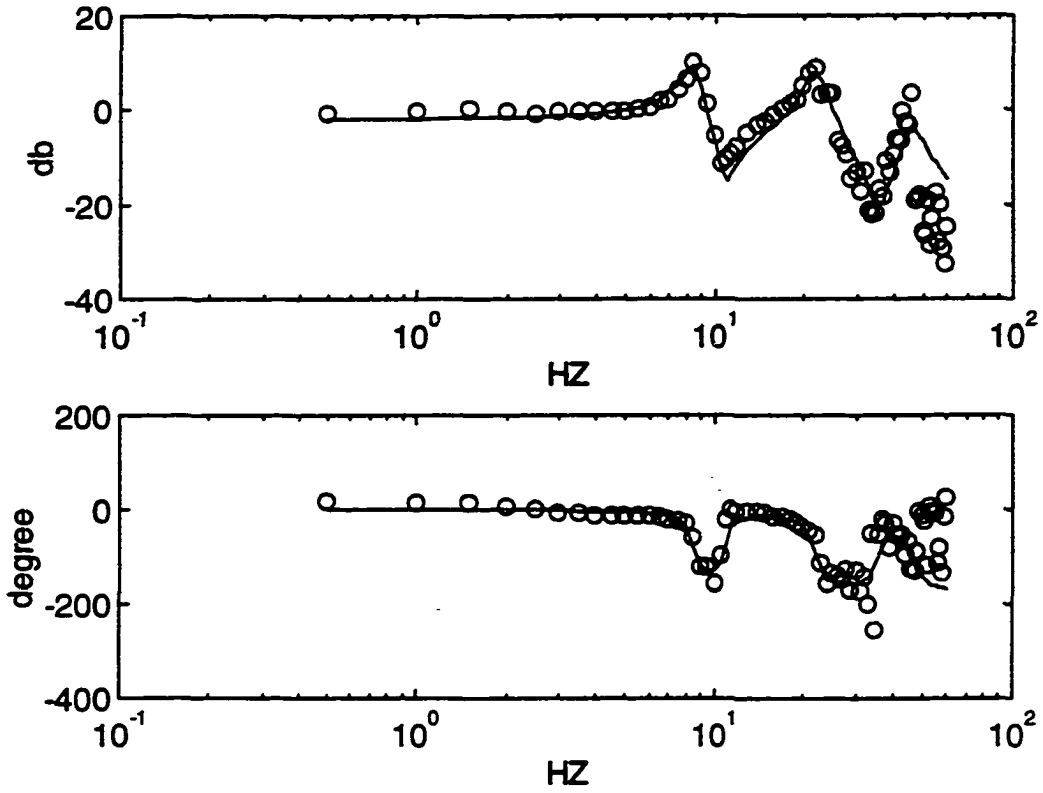

Figure 2-14 Fitting of experimental results (o) with transfer function G_2 (-)

Optimized G_2 fit:

$$G_2 = \frac{A_1\omega_1^2}{s^2 + 2\xi_1\omega_1 s + \omega_1^2} + \frac{A_2\omega_2^2}{s^2 + 2\xi_2\omega_2 s + \omega_2^2} + \frac{A_3\omega_3^2}{s^2 + 2\xi_3\omega_3 s + \omega_3^2}$$

where:

$$\omega_1 = 2*\pi*8.5,\ A_1 = 0.3594,\ \xi_1 = 0.0616,$$

$$\omega_2 = 2*\pi*22,\ A_2 = 0.3537,\ \xi_2 = 0.0681,$$

$$\omega_3 = 2*\pi*46,\ A_3 = 0.0934,\ \xi_3 = 0.0766. \qquad (2\text{-}11)$$

G_2 fits the experimental frequency response well in Figure 2-14. Its confirmation with experimental time-domain response is shown in Figure 2-15. The experiment applies closed-loop PD control on rigid body, with gain values as in Figure 2-6.

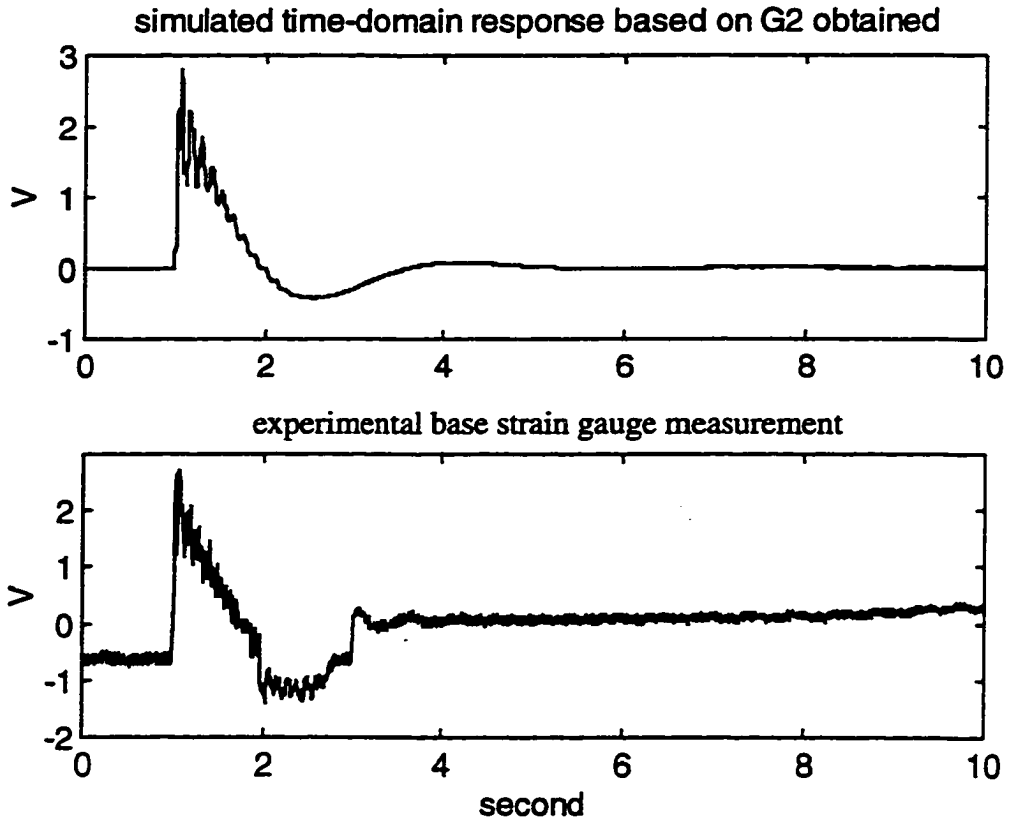

Figure 2-15 confirming G_2 with time-domain measurements

The peaks of the curves fit very well between simulation and experimental results, as shown in above Figure. The dominant oscillatory frequencies in the experimental data also fit the simulations quite well. The mismatch between 2 and 3 seconds in the above figure are due to friction and will be considered later in this chapter.

2.2.2.2 G_2 (Base Strain Gauge) Transfer function With Payload

Model of G_2 in the presence of payloads are also fitted, with the identical method (Algorithm II) as in last section. With a payload of 75g, three oscillation mode can still be observed at the 8.5 Hz, 22 Hz and 42 Hz respectively, but the damping factor and gains of these transfer functions are changed:

$$\omega_1=2*\pi*8.5,\ A_1=0.8464,\ \xi_1=0.0394,$$

$$\omega_2=2*\pi*22,\ A_2=0.3508,\ \xi_2=0.0263,$$

$$\omega_3=2*\pi*42,\ A_3=0.1203,\ \xi_3=0.0147 \qquad (2\text{-}12)$$

The fit between transfer function G_2 (with a payload of 75g) and experimental frequency response is illustrated as below Figure 2-16:

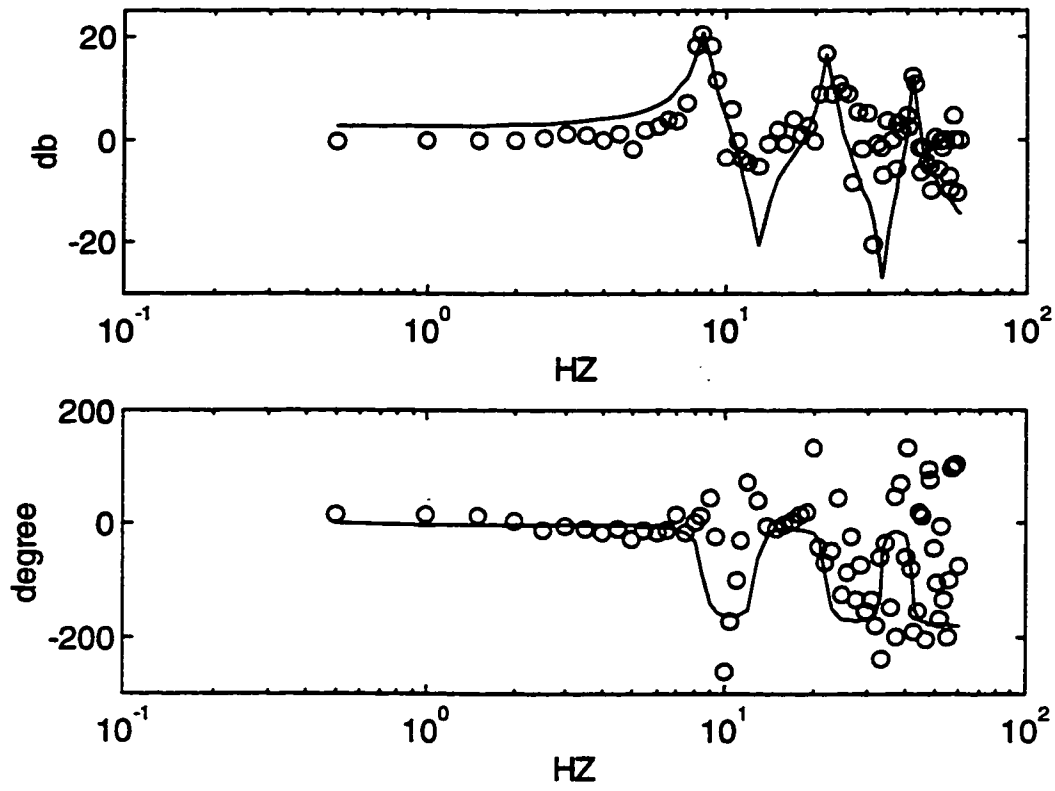

Figure 2-16 Fitting of experimental results (o) with transfer function G_2 (-), with payload 75g

With a payload of 150g, three oscillation modes can be observed at the 8 Hz, 23 Hz and 40 Hz the damping factor and mode magnitude are now:

$$\omega_1=2*\pi*8,\ A_1=1.0688,\ \xi_1=0.0359,$$
$$\omega_2=2*\pi*23,\ A_2=0.3901,\ \xi_2=0.0233$$
$$\omega_3=2*\pi*40,\ A_3=0.0950,\ \xi_3=0.0290 \qquad (2\text{-}13)$$

The fit between transfer function G_2 (with payload 150g) and experimental frequency response is illustrated as below Figure 2-17:

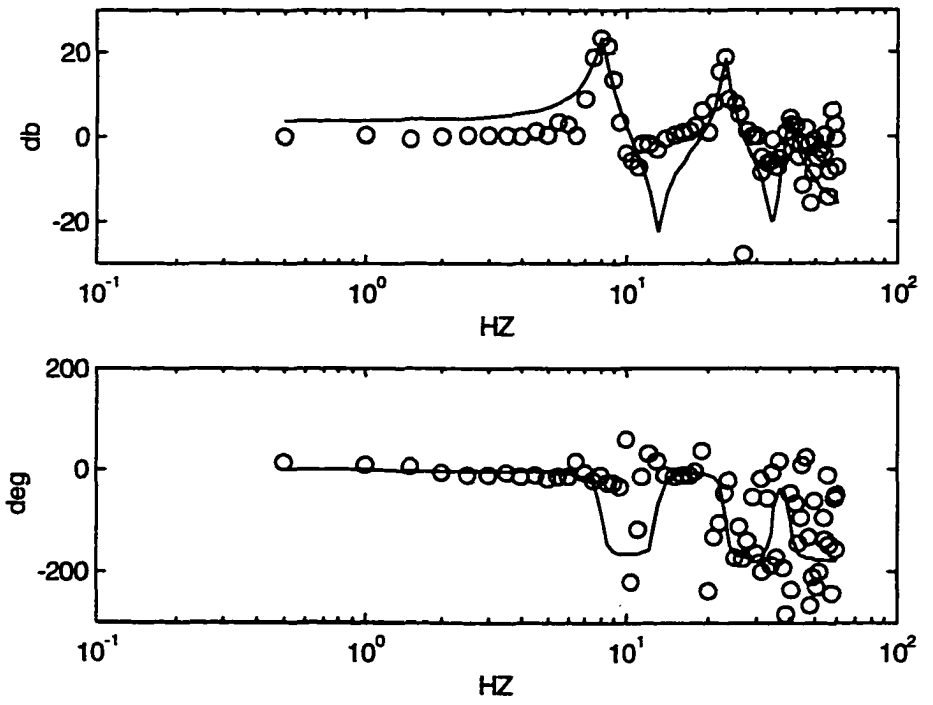

Figure 2-17 Fitting of experimental results (o) with transfer function G_2 (-), with payload 150g

With a payload of 380g, three modes can be observed: 8 Hz, 23 Hz and 42 Hz. The parameters are now:

$$\omega_1=2*\pi*8,\ A_1=0.7330,\ \xi_1=0.0457,$$
$$\omega_2=2*\pi*23,\ A_2=0.7163,\ \xi_2=0.0346,$$
$$\omega_3=2*\pi*42,\ A_3=0.2292,\ \xi_3=0.0539 \qquad (2\text{-}14)$$

The fit between transfer function G_2 (with payload 350g) and experimental frequency response is illustrated as below Figure 2-18:

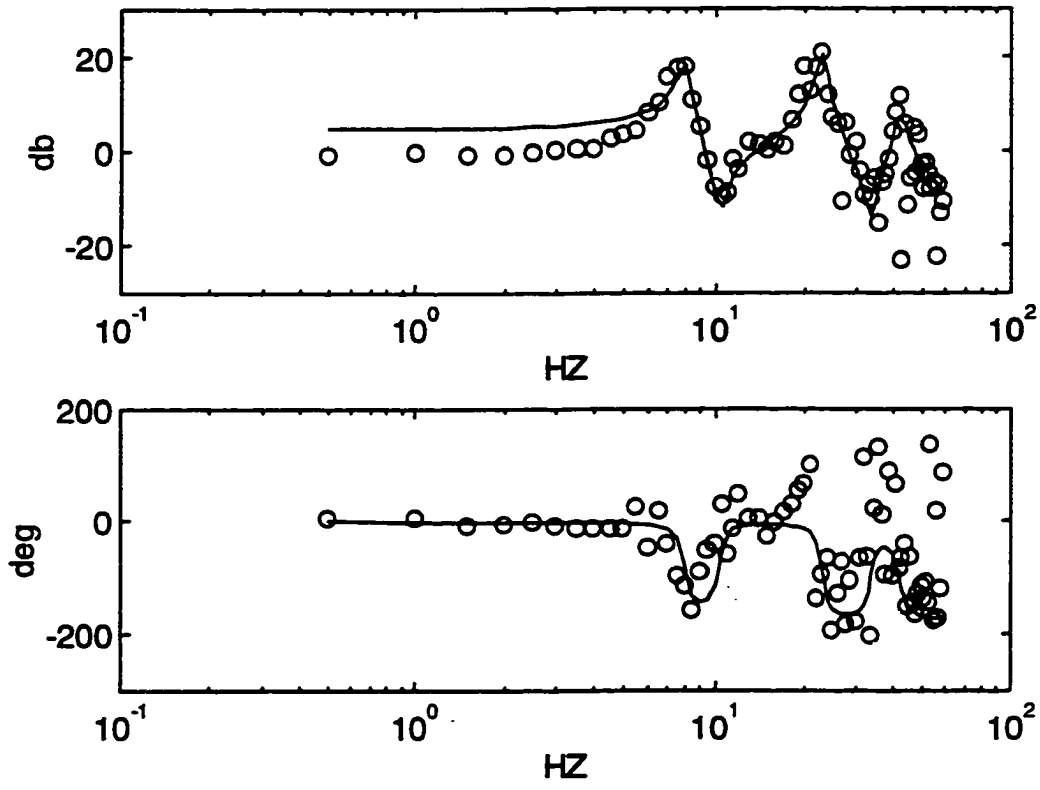

Figure 2-18 Fitting of experimental results (o) with transfer function G_2 (-), with payload 380g

2.2.2.3 G_3 (2nd Strain Gauge) Transfer function Without Payload

Only two mode peaks around 8.5 Hz and 22 Hz can be observed in the frequency response of second strain gauge measurement.

G_3 is fitted in the form below:

$$G_3 = \frac{A_1\omega_1^2}{s^2 + 2\xi_1\omega_1 s + \omega_1^2} + \frac{A_2\omega_2^2}{s^2 + 2\xi_2\omega_2 s + \omega_2^2}$$

without payload, the parameters take the following value:

$$\omega_1 = 2*\pi*8.5,\ A_1 = -0.4975,\ \xi_1 = 0.0857,$$
$$\omega_2 = 2*\pi*21,\ A_2 = 0.2547,\ \xi_2 = 0.0819 \qquad (2\text{-}15)$$

The methods used to fit parameters in Equation (2-15) is identical (Algorithm II) to that used in the last two sections. The fit between the frequency response obtained from transfer function G_3 and experimental frequency response is illustrated in below Figure 2-19:

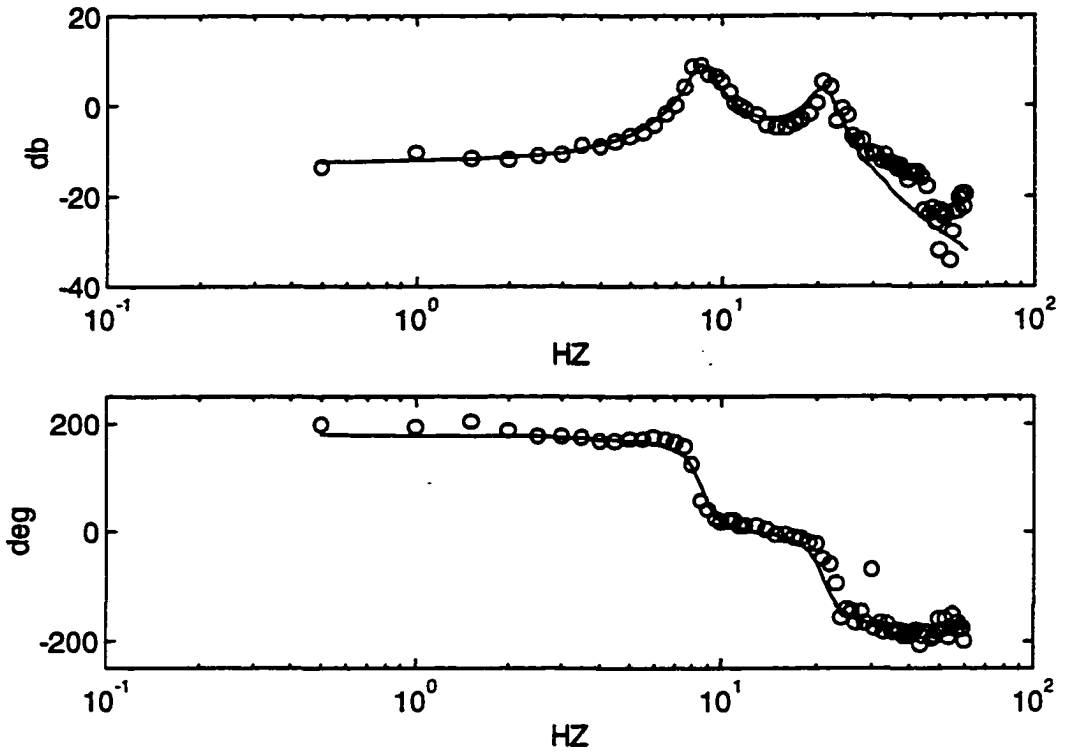

Figure 2-19 Fitting of experimental results (o) with transfer function G_3 (-), without payload

It is observed in the above figure that the fitted model matches the experimentally identified frequency response very well. Also the damping factors at two modes are fairly close. This linear model is confirmed by comparing simulated and experimental time-domain response as in Figure 2-20. The experiment applies closed-loop PD control on rigid body, with the gains setting as in Figure 2-6.

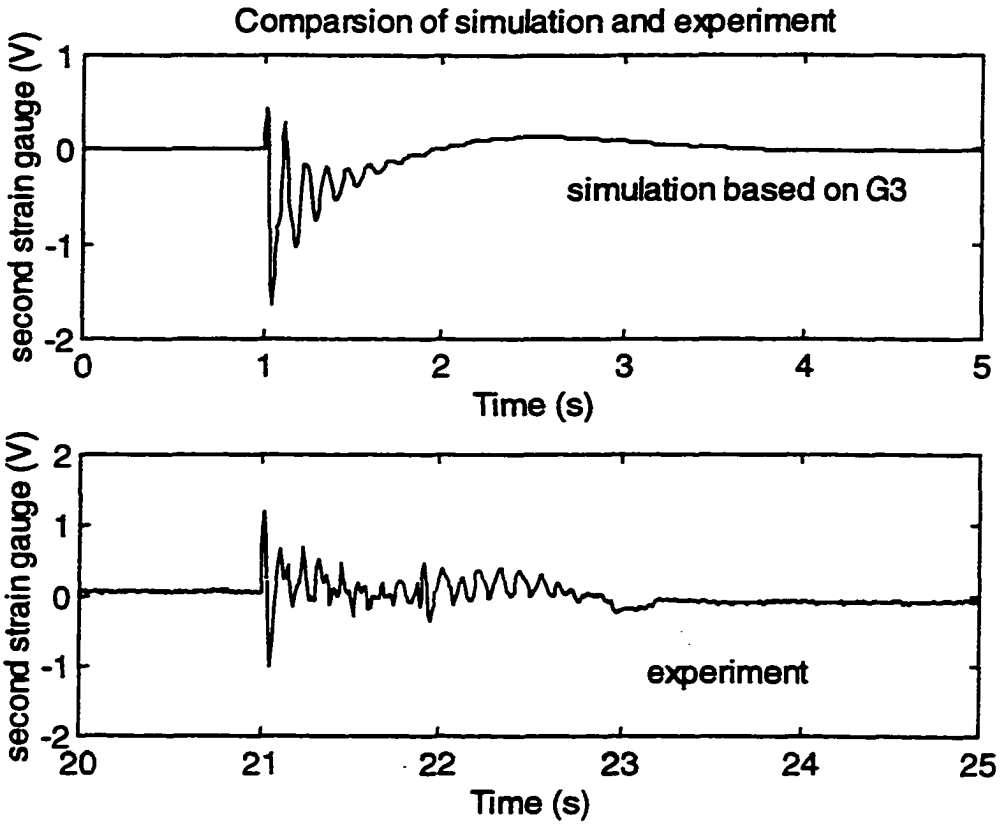

Figure 2-20 Confirming G_3 with experimental time-domain measurement

2.2.2.4 G_3 (2nd Strain Gauge) Transfer function With Payload

In the presence of a payload of 75g, the model parameters change to the following value:

$$\omega_1=2*\pi*8,\ A_1=-1.4220,\ \xi_1=0.0435,$$
$$\omega_2=2*\pi*22,\ A_2=0.8525,\ \xi_2=0.2011 \qquad (2\text{-}16)$$

The fit between simulated and experimental frequency-domain response is illustrated in the Figure 2-21:

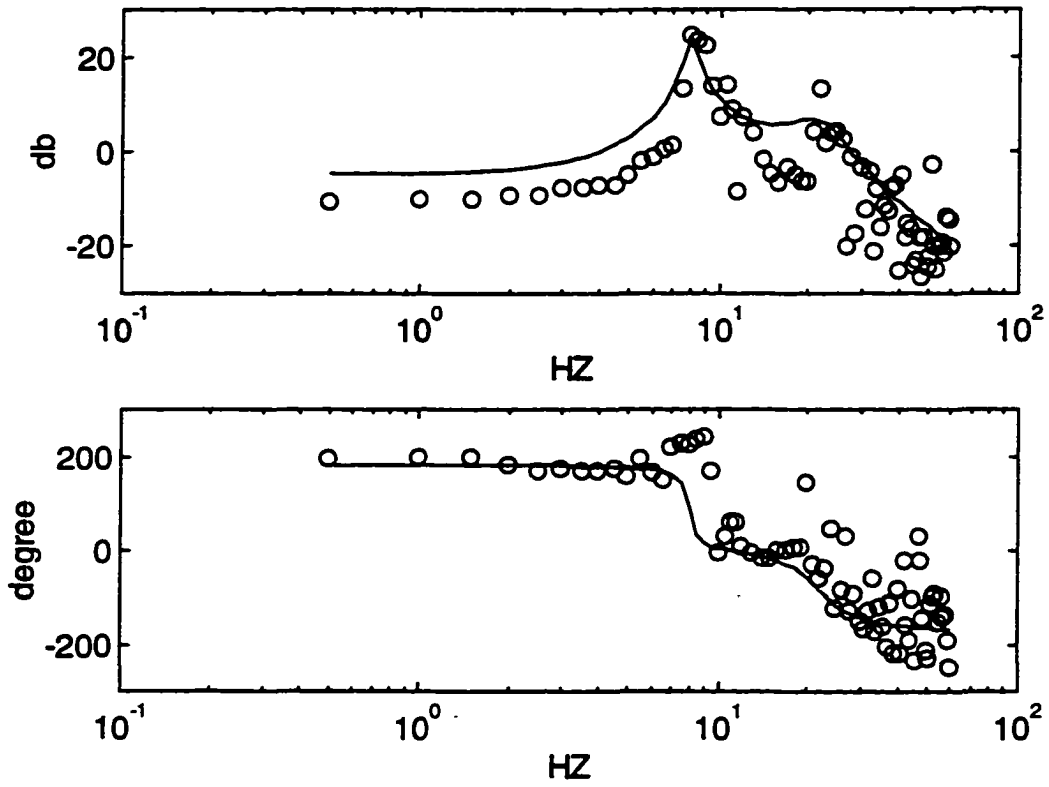

Figure 2-21 Fitting of experimental results (o) with transfer function G_3 (-), with payload of 75g

In the presence of a payload of 150g, the model parameters change to following value:

$$\omega_1=2*\pi*8,\ A_1=-1.4010,\ \xi_1=0.0426,$$
$$\omega_2=2*\pi*23,\ A_2=0.8336,\ \xi_2=0.2071 \qquad (2\text{-}17)$$

The fit between simulated and experimental frequency-domain response is illustrated in Figure 2-22:

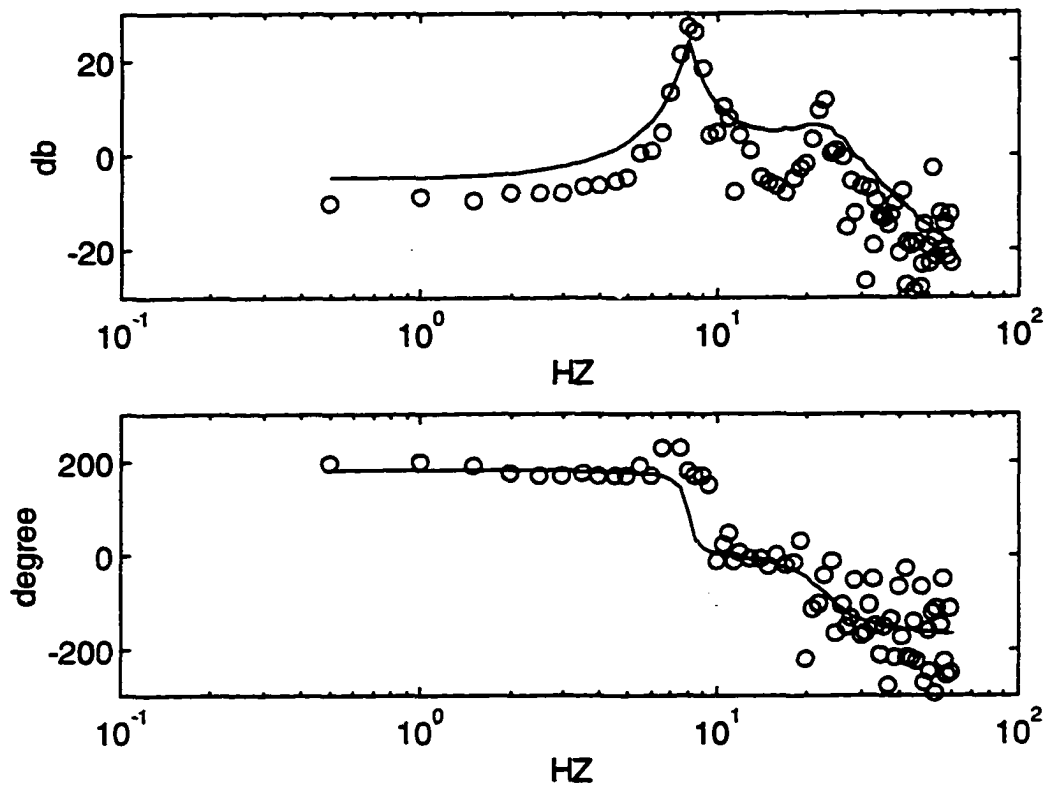

Figure 2-22 Fitting of experimental results (o) with transfer function G_3 (-), with payload of 150g

In the presence of a payload of 380g, the model parameters change to following value:

$$\omega_1=2*\pi*7.5,\ A_1=-2.0682,\ \xi_1=0.0406,$$
$$\omega_2=2*\pi*23,\ A_2=0.3669,\ \xi_2=0.0607 \qquad (2\text{-}18)$$

The fit between simulated and experimental frequency-domain response is illustrated in following Figure 2-23:

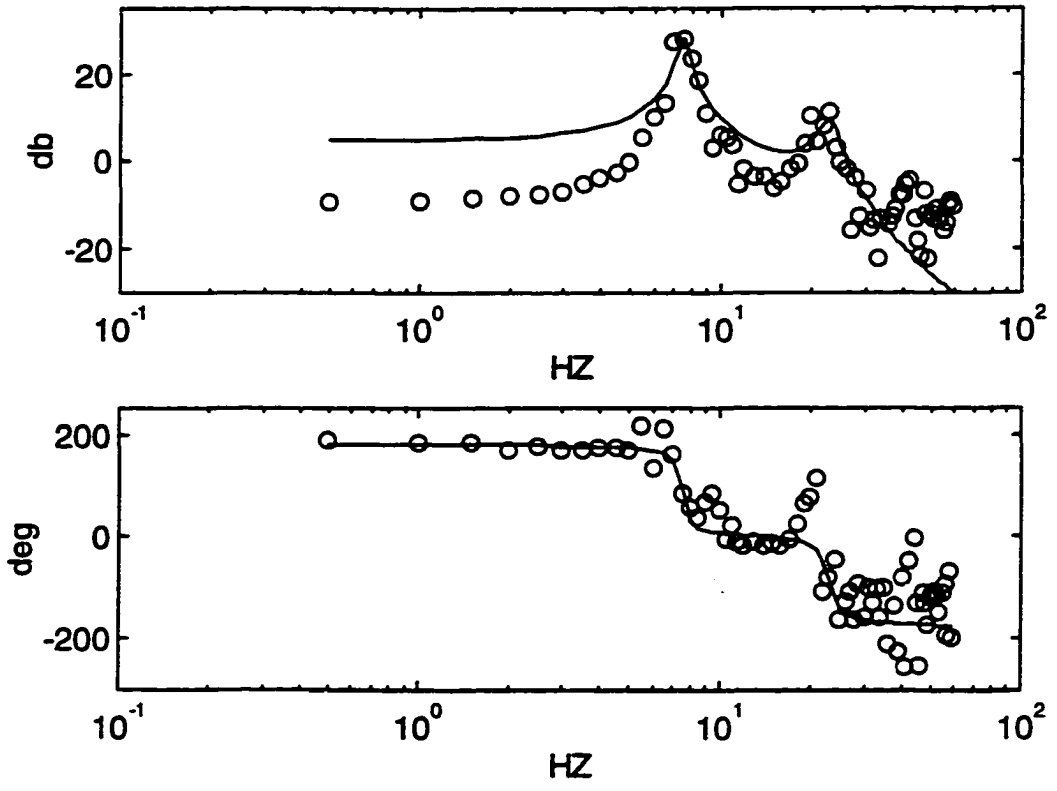

Figure 2-23 Fitting of experimental results (o) with transfer function G_3 (-), with payload of 380g

2.2.3 Modeling of Nonlinear Sections of the Flexible-Link Manipulator

Nonlinear sections, particularly static friction and gear hitting caused by backlash, significantly influence the system performance. The effect of friction can be seen in the comparison of simulated and experimental rigid body response in Figure 2-10: the experimental results and simulations differ around steady state without having the overshoot indicated by simulation. It is obvious that this is caused by friction between manipulator and shaft shoulder: the manipulator stops moving when error is small and controller effort is too small to overcome friction.

A close examination of the comparison of simulated and experimental strain gauge measurements also indicates the influence of nonlinearities particularly backlash (see for e.g. Figure 2-15). Figure 2-24 below is the comparison of second strain gauge response obtained from experiment and simulation use identical schematics. The simulation are done using only the linear models identified earlier:

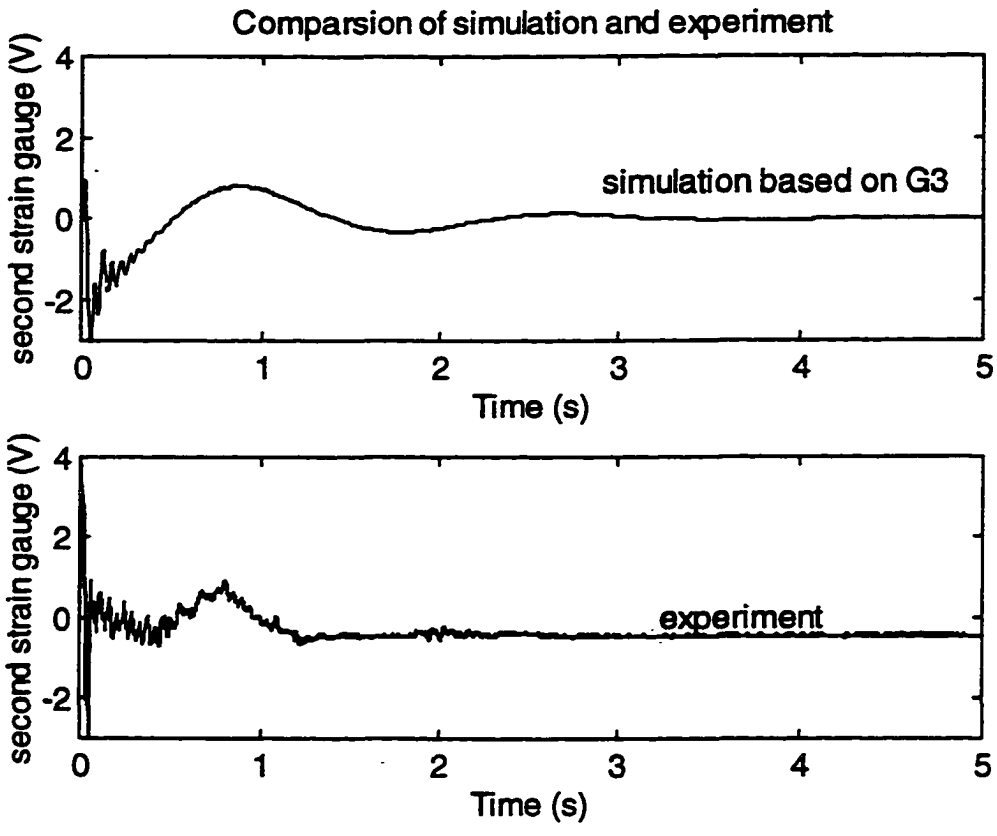

Figure 2-24: Nonlinear effects: comparison of simulated & experimental 2nd gauge response using same schematic

It is observed in Figure 2-24 that the linear model is not able to predict the 22 Hz (second oscillation mode) behavior of second strain gauge response, neither can it explain the experimental measurements in the first 0.5 second.

This thesis presents the models of the two most important nonlinearities: Coulomb friction (static) and gear hitting caused by backlash.

2.2.3.1 Friction

The torque caused by friction between manipulator and shaft shoulder directly applies on the manipulator and significantly influences the movement of the arm.

The friction consists of both viscous friction and Coulomb friction. Viscous friction is proportional to relative movement velocity between manipulator and shaft shoulder, it is already taken into account while identifying the system linear model. Coulomb friction increases along with the increase of DC motor controller effort so that the manipulator is static, beyond which it drops slightly and stays unchanged while the manipulator moves [16, 23]. These effects of friction are illustrated in Figure 2-25:

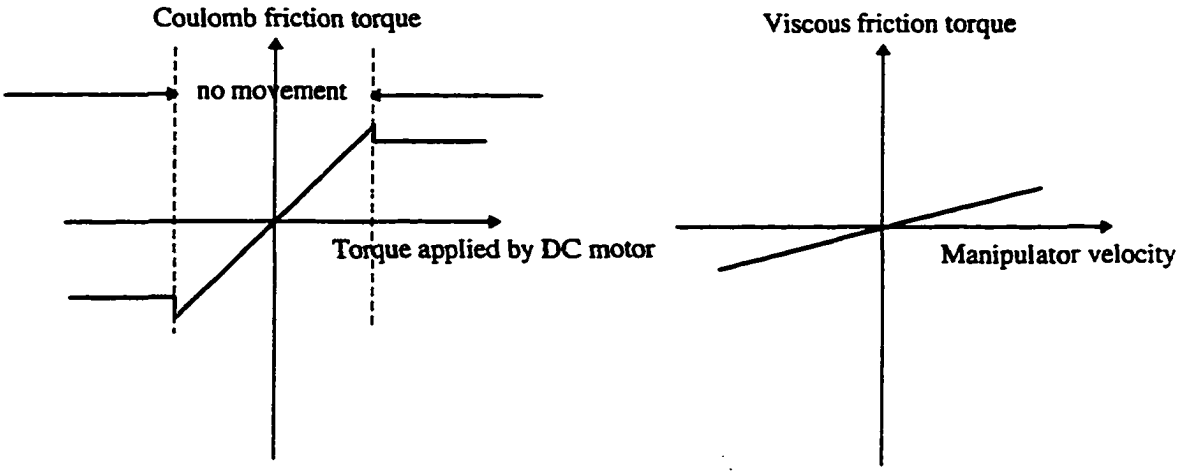

Figure 2-25 Illustration of Coulomb friction and viscous friction

Putting the two friction (viscous and Coulomb) together, the total controller effort applied on manipulator is:

$$u_T = u - u_C - u_V = u - u_C - K * \frac{d\theta}{dt} \qquad (2\text{-}19)$$

where θ is the shaft angle, u_T is the controller effort (motor current) actually applied to the manipulator to accelerate it after friction is taken into account, u is the motor current supplied to the DC motor, and u_C, u_V are the motor current required to overcome the Coulomb friction and viscous friction respectively. Value of u_V is proportional to angular speed.

As experimentally identified in the apparatus, the motor current required to overcome the Coulomb friction (u_C) is 0.32A before moving and 0.22A after moving. The motor current required to overcome viscous friction (u_V) is chosen as a proportional ratio K of 0.1A/(rad/s). K is artificially selected very small for simulation since viscous friction is already taken into account in linear system model.

By replacing u in the earlier simulation with u_T of Equation (2-19), new simulations are produced on both rigid body and strain gauge responses. Figure 2-26 is an updated version of Figure 2-10, comparing simulated and experimental rigid body response, using gain setting of P=1.2 and D=0.62:

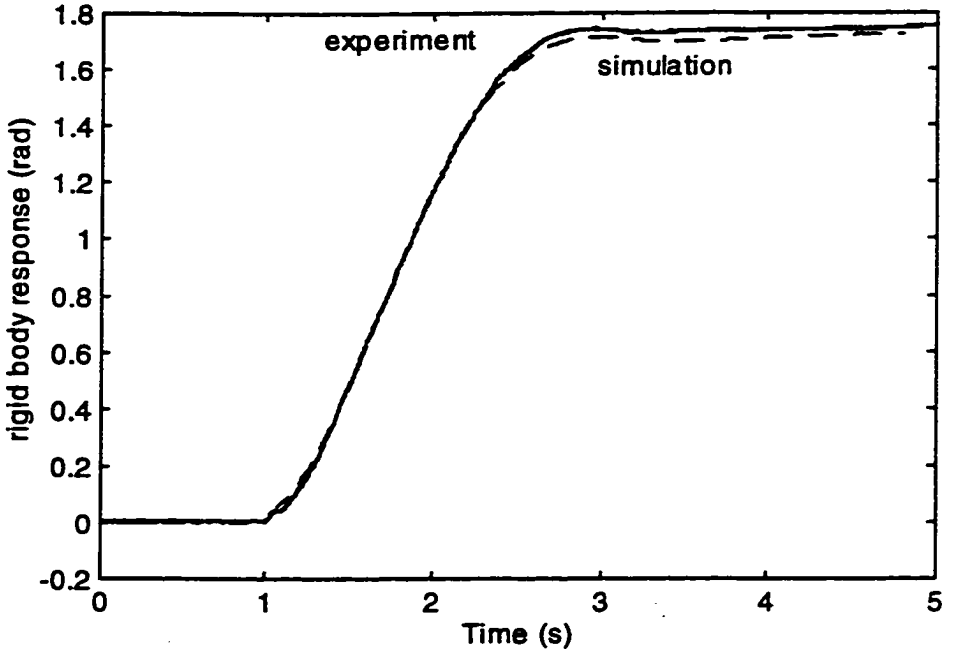

Figure 2-26 Comparison of simulated(--) and experimental(-) rigid body response, taking friction into account

As shown in above figure, simulation and experiment results overlap each other very well, and the mismatch of overshoot disappears.

Also the simulation of second strain gauge output, which takes friction effects into account, is compared with experimental results in Figure 2-27:

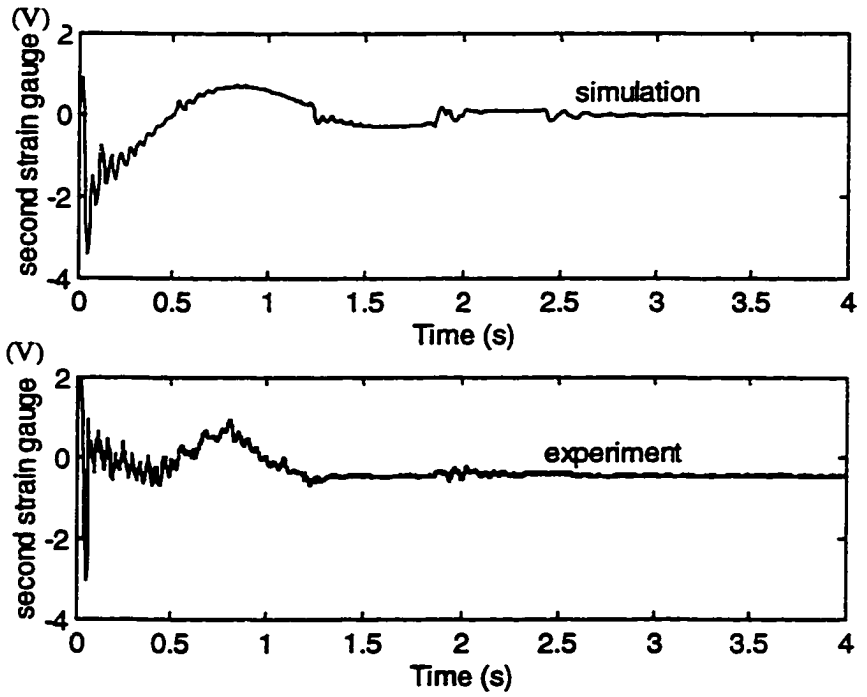

Figure 2-27 Comparison of simulated and experimental second strain gauge response, taking friction into account

By taking friction into account, simulation is able to predict the 22 Hz vibration behavior of second strain gauge. The difference between experimental measurement and simulation before 0.5s is caused by the gear hitting effects (due to backlash) at the very beginning of the setpoint change.

Based on this friction model, simulation is also performed on base strain gauge measurement, Figure 2-28 is an updated version of Figure 2-15. By taking friction effects into account, simulation is now able to predict the measurement jump around 1.9 s before system settles down. This could not be explained by the linear model alone as shown in Figure 2-15.

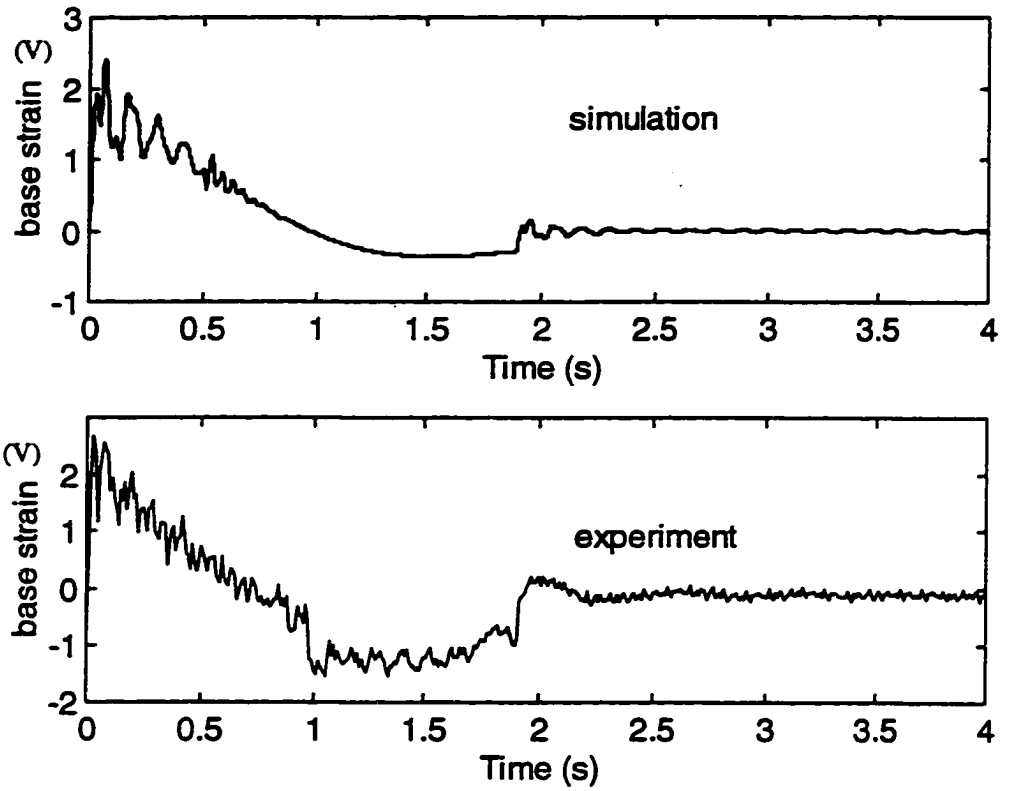

Figure 2-28 Comparison of simulated and experimental base strain gauge response, taking friction into account

2.2.3.2 Gear Hitting Caused by Backlash

The gear chain (one pair of gears in our case) in any mechanical system will unavoidably have backlash. The modeling of the effect of backlash [25] on our system is described in this section. The backlash existing in apparatus is illustrated in Figure 2-29:

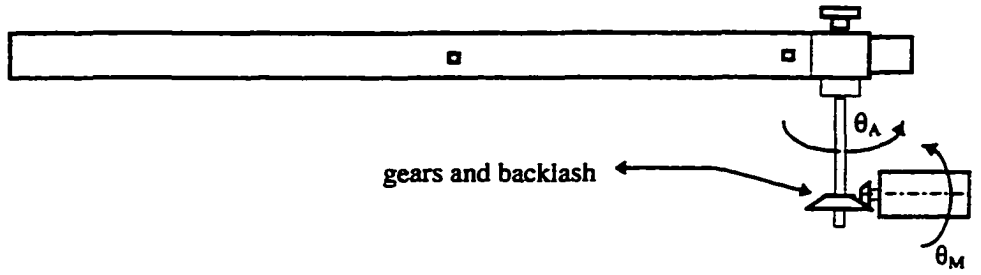

Figure 2-29 Backlash in the gear chain

In Figure 2-29, θ_M is the angle of the driving gear (DC motor) and θ_A is the angle of the driven gear (arm). It is assumed in the following that the angles and inertia involved are reflected to the arm side. When two gears are not engaged, θ_M is different from θ_A. In this case, there is no interaction between the DC motor and the arm shaft. And until engaging, they are developing their own angles obeying the following two independent equations:

$$J_M \ddot{\theta}_M = T_M \tag{2-20}$$

$$J_A \ddot{\theta}_A = -T_F \tag{2-21}$$

where J_M is the inertia of motor (reflected to the arm side) and J_A is the inertia of manipulator arm. T_M is the driving torque offered by motor and T_F is the friction torque at the shaft (we neglect the friction in the motor). Since J_M is smaller than J_A, θ_M may develop fairly large velocity before it engages with the driven gear. This is the natural cause of gear hitting, which results in a velocity jump of both θ_M and θ_A, as shown in Equation (2-22) when the gears finally engage. [25]:

$$\dot{\theta}_{MA} = \frac{J_M}{J_M + J_A}\dot{\theta}_M + \frac{J_A}{J_M + J_A}\dot{\theta}_A \tag{2-22}$$

In Equation 2-22 $\dot{\theta}_{MA}$ is the common velocity after the two gears are engaged.

After the two gear are engaged, the system can be treated as $\dot{\theta}_{MA} = d\theta_M/dt = d\theta_A/dt$ and $\theta_M = \theta_A$. The differential equation governing the dynamics of the whole system becomes:

$$(J_A + J_M)\ddot{\theta}_{MA} = T_M - T_F \tag{2-23}$$

In simulation, the initial values of θ_A and θ_M are respectively selected as -50° and -53° (full backlash is 3°.). And the J_A and J_M are selected as 0.027Kgm^2 and 0.003 Kgm^2 respectively. The schematic used to calculate this backlash nonlinearity is illustrated in Figure 2-30:

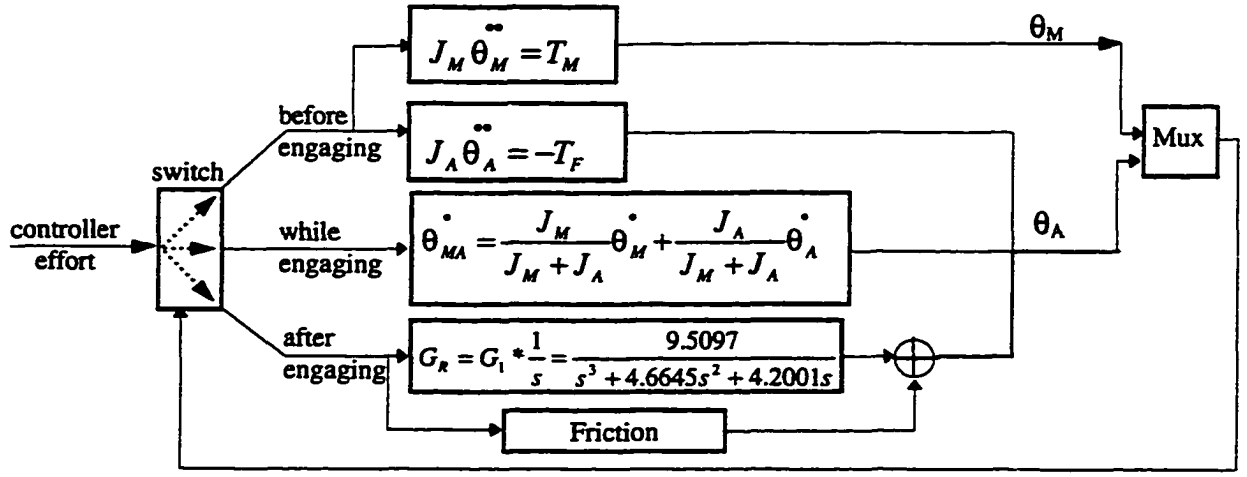

Figure 2-30 schematic used to present backlash nonlinearity

When setpoint change is made, gears start from being unengaged to being engaged, the backlash causes a substantial velocity hitting on the arm. Furthermore when control effort switches direction, the backlash causes a switch of gear engagement from positive to negative or vice versa. This causes the 22 Hz oscillatory behavior after 0.5s in the strain gauge measurement. If this nonlinear hitting is taken into account by combining Equation 2-20 2-21 2-22 2-23 into the entire system model as per Figure 2-30, a new simulation of second strain gauge response is produce in Figure 2-31, which better predicts the experimental behavior:

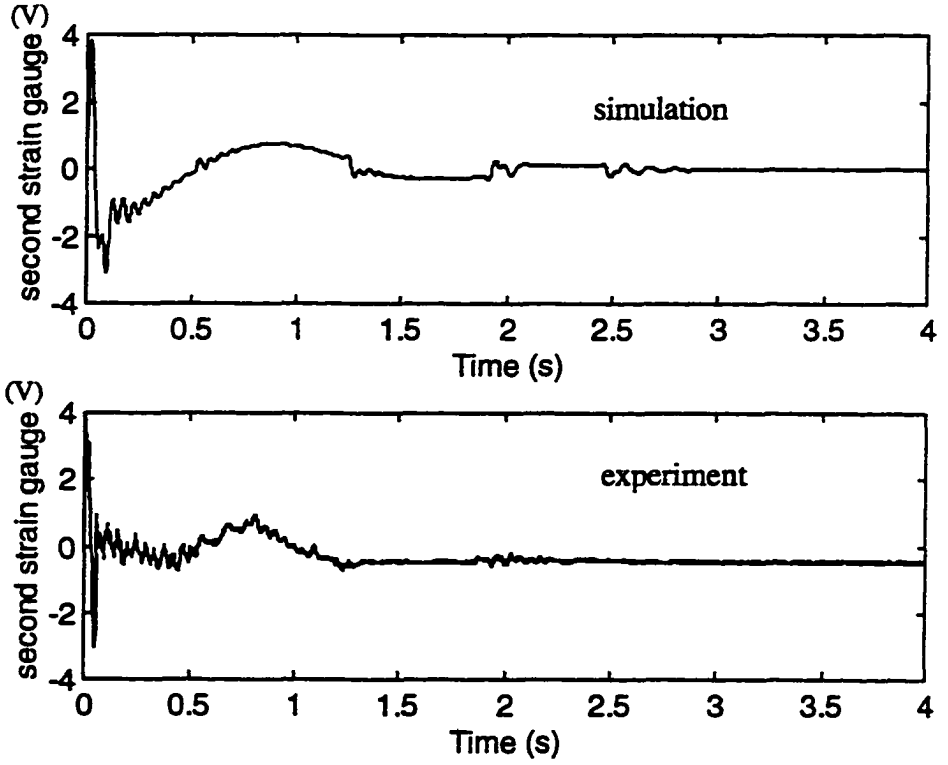

Figure 2-31 Comparison of simulated and experimental second strain gauge response, taking hitting into account

2.2.4 Comparison and Conclusions

The linear models obtained in previous sections are summarized below.

Without payload on the manipulator tip, G_L (linear part of whole model) in Equation (2-1) is identified as Equation 2-24:

$$G_L = \begin{bmatrix} G_R \\ G_2 \\ G_3 \end{bmatrix} = \begin{bmatrix} \dfrac{9.5097}{s(s^2+4.6645s+4.2001)} \\ \dfrac{1025.1}{s^2+6.6s+2852.3} + \dfrac{6758.3}{s^2+19s+19108} + \dfrac{7802.3}{s^2+44s+83536} \\ \dfrac{-1419}{s^2+9.154s+2852.3} + \dfrac{4434.3}{s^2+21.6129s+17410} \end{bmatrix} \quad (2\text{-}24)$$

This transfer function matrix will be used throughout this thesis and will contribute to the design of appropriate controllers.

How the parameters of the three elements of G_L (G_R G_2 and G_3) vary in the presence of payloads has also been studied in the previous sections. With the presence of different payloads, transfer function G_R (from controller effort u to rigid body shaft angle position) is listed in Table 2-1.

Comparison of G_R: transfer function from controller effort u to shaft angle position				
Payload	**Transfer function (G_R=1/s*G_1)**	**dc gain (db) of G_1**	**pole 2**	**pole 3**
none	$\dfrac{9.5097}{s(s^2+4.6645s+4.2001)}$	7.0981	-3.4455	-1.2190
75g	$\dfrac{5.6070}{s(s^2+3.5981s+4.1295)}$	2.6567	-1.7990 - 0.9449i	-1.7990 + 0.9449i
150g	$\dfrac{3.9938}{s(s^2+3.1329s+3.6671)}$	0.7413	-1.5664 - 1.1015i	-1.5664 + 1.1015i
380g	$\dfrac{1.0463}{s(s^2+1.5837s+1.7737)}$	-4.5845	-0.7919 - 1.0708i	-0.7919 + 1.0708i

Table 2-1 Comparison of transfer function G_1 under various payloads

Several conclusions can be drawn on the change of G_R under payloads:

1. When payload increases, the dc gain of G_1 decreases;

2. When payload increases, the poles of G_1 move towards the origin;

3. When payload increases, natural frequency of G_1 decreases;

4. When payload increases, damping factor of G_1 decreases;

G_1's frequency responses with and without payloads are illustrated in Figure 2-32, where line 0 represents no payload, line 1 represents payload of 75g, line 2 represents payload of 150g and line 3 represents payload of 380g.

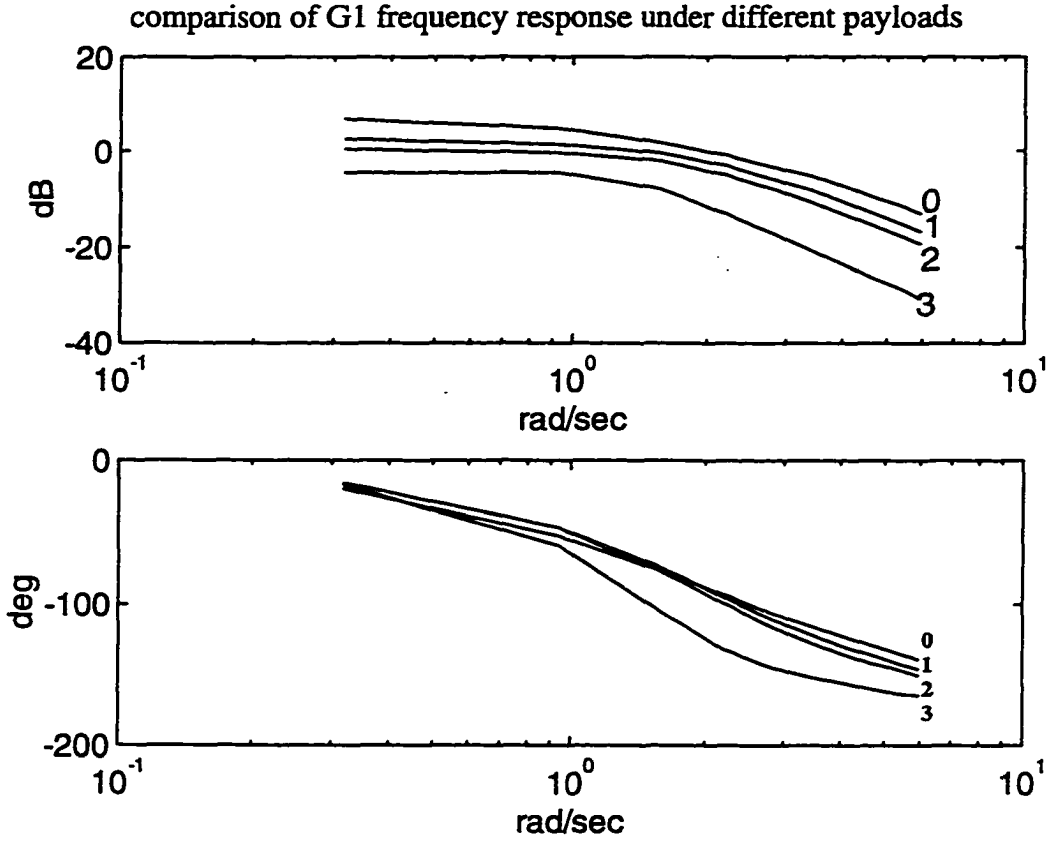

Figure 2-32 Comparison of G_1 frequency response under various payloads, 0g(0) 75g(1) 150g(2) and 380g(3)

G_2 (the transfer function from effort u to base strain gauge measurement) is represented in the form of 3 oscillation modes as per Equation 2-11. By comparing the change of natural frequency, mode magnitude and damping factors, the influence of payloads can be observed. Table 2-2 shows the variation of these parameters.

Some rough conclusions can be drawn on the change of G_2 under payloads:

1. When payload increases, the damping factors of all three modes decrease.

2. When payload increases, the gains of all three modes increase.

Comparison of G_2: transfer function from effort u to base strain gauge measurement									
	1st oscillation mode			2nd oscillation mode			3rd oscillation mode		
Payload	ω_1	A_1	ξ_1	ω_2	A_2	ξ_2	ω_3	A_3	ξ_3
0	2*π*8.5	0.3594	0.0616	2*π*22	0.3537	0.0681	2*π*46	0.0934	0.0766
75g	2*π*8.5	0.8464	0.0394	2*π*22	0.3508	0.0263	2*π*42	0.1203	0.0147
150g	2*π*8	1.0688	0.0359	2*π*23	0.3901	0.0233	2*π*40	0.0950	0.0290
380g	2*π*8	0.7330	0.0457	2*π*23	0.7163	0.0346	2*π*42	0.2292	0.0539

Table 2-2 Comparison of transfer function G_2 under various payloads

G_3 (the transfer function from effort u to second strain gauge) is represented in the form of 2 oscillation modes as per Equation 2-16. By comparing the change of natural frequency, gains and damping factors, the influence of payloads can be observed in Table 2-3:

Comparison of G_3: transfer function from effort u to second strain gauge						
	1st oscillation mode			2nd oscillation mode		
Payload	ω_1	A_1	ξ_1	ω_2	A_2	ξ_2
0	2*π*8.5	-0.4975	0.0857	2*π*21	0.2547	0.0819
75g	2*π*8	-1.4220	0.0435	2*π*22	0.8525	0.2011
150g	2*π*8	-1.4010	0.0426	2*π*23	0.8336	0.2071
380g	2*π*7.5	-2.0682	0.0406	2*π*23	0.3669	0.0607

Table 2-3 Comparison of transfer function G_3 under various payloads

The trend how payloads influence on G_3 parameters is similar to the one on G_2, although not as obvious:

1. Roughly speaking, when payload increases, damping factor of two modes decrease.
2. When payload increases, absolute magnitude of gains of two modes increase.
3. The gain of first mode takes negative value while the gain of second mode takes positive value (this is different from G_2);

Nonlinearities, particularly Coulomb friction, viscous friction and gear hitting caused by backlash, are presented to supplement the linear transfer function. Models taking friction section into account produce better prediction of rigid body response and strain gauge response. Hitting model due to backlash also helps to explain system behavior which cannot be explained by linear model alone.

Chapter 3

Exploration of PIDP Control

In this chapter, PD controllers are considered for the flexible link manipulator control, based on the model obtained in Chapter 2. The controllers are optimized in the sense of minimizing rigid body step response error and suppressing strain gauge measurements of vibration (to zero). The whole control structure is described as a PIDP combination: PD controller plus conditional I controller for rigid body tracking, and P controller using noise-filtered and lowpass-filtered information for vibration suppression. The use of low-pass filter on second strain gauge measurement feedback is detailed. This controller is implemented experimentally and the system performance is shown. Also some other related issues, like sensor signal prefiltering (noise filters), dither to reduce friction effects are discussed in this chapter.

3.1 Optimized PID Controller for Rigid Body Tracking

In Chapter 2, a PD controller is experimentally implemented to serve as the platform for system identification. The rigid body system performance under that PD controller is good: the arm tracks the reference step input well, reaches steady state within 2 seconds and hardly produces any overshoot (see experimental results in Figure 2-10). This performance shows the promise of PD controllers on flexible-link manipulator. In this chapter we explore design of optimized PD controllers using the identified linear and nonlinear models and study their experimental performance.

The optimal PD gains for the rigid body tracking are designed using the integral absolute error (IAE) method for input step of 100 degree. (IAE value is calculated from simulation results based on system model obtained in Chapter 2.) In addition to the minimization of the IAE criterion, practical issues and constraints are also penalized in the optimization. Thus the function minimized is:

$$F = IAE + Penalty\_function \tag{3-1}$$

The practical issues considered in penalty function are:

1. The motor current in the apparatus is limited to a certain maximum value (5A in current case), any controller effort requiring more than this amount of current (for a 100 degree slew in current case) will be not be feasible. The penalty function takes a high value in this case. (higher flat area in following Figure 3-1.)

2. Any performance which shows more than 35% overshoot is eliminated by assigning penalty function a high value.

3. Any performance which cannot settle down within 10 seconds (slow response) is eliminated by a high penalty function.

To perform global searching for the PD gains, a surface of the Function F of Equation (3-1) is plotted and shown in Figure 3-1. The lower the F value, the better the system performance.

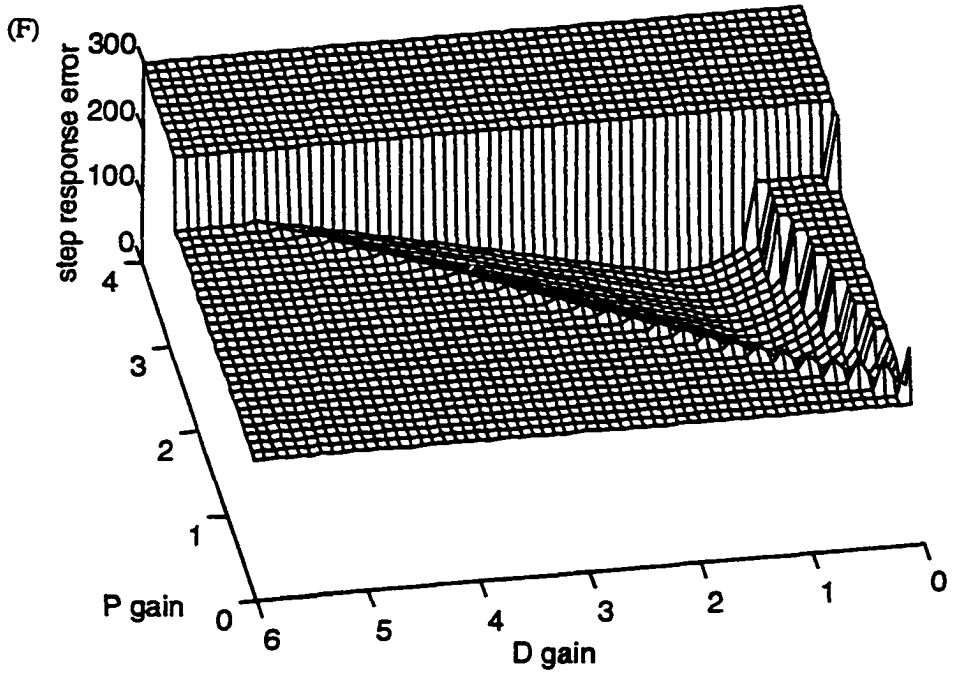

Figure 3-1 Global searching of optimized P and D gains for PD controller

Figure 3-1 provides an overall idea about the PD gain effects on F value of Equation (3-1). The flat areas are eliminated by the penalty function because controller effort is too large or system response is too slow etc., and only the inner triangle area is the acceptable gain area for PD controller design. See Figure 3-2 for a close-up view of the inner triangle area:

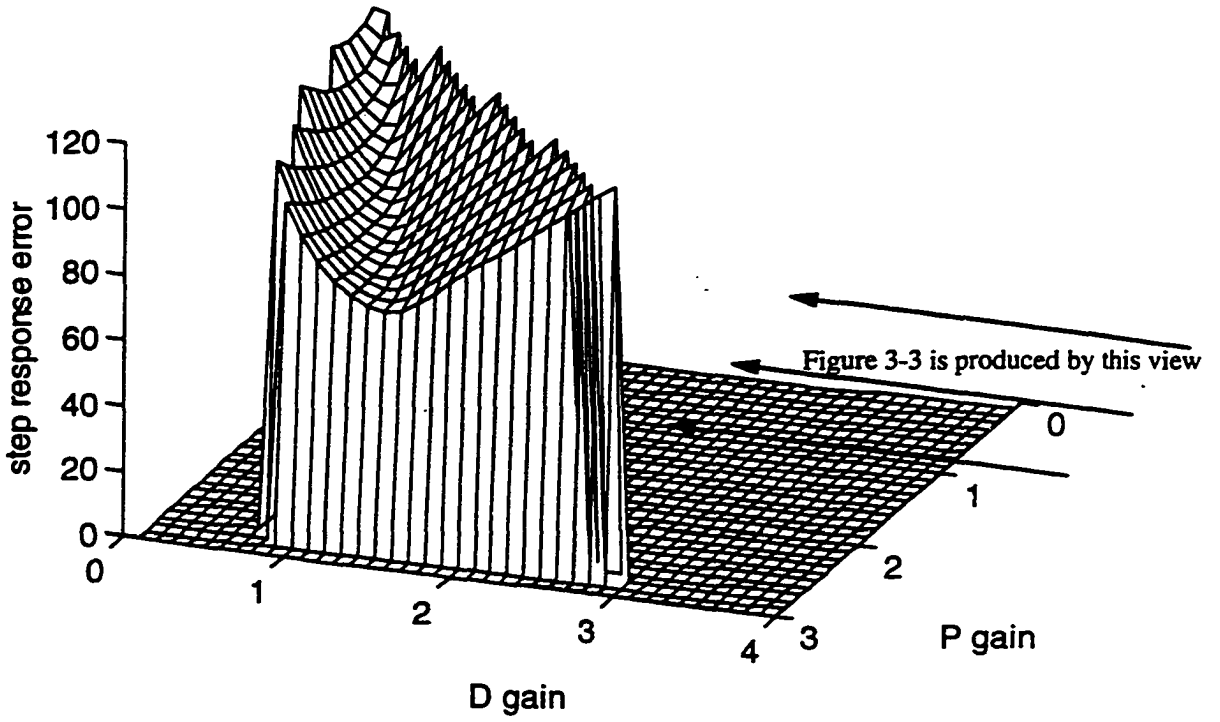

Figure 3-2 The acceptable P D gain area forms a valley

The inner area with small F function value appears like a triangular valley as shown in above figure. Valley bottom (minimal errors) is on the middle line of this triangle, and the bottom tends to go down while P D gains are increasing. This indicates that higher well-selected P D gains produce better system response. (However, it is also revealed that valley bottom decreases down fast before P=3 and slow thereafter, correspondingly system performance is not significantly improved as we increase P and D gains to much higher values.). Figure 3-3 takes another profile of the above figure and shows the decreasing trend with P gain of the valley (IAE alone was used).

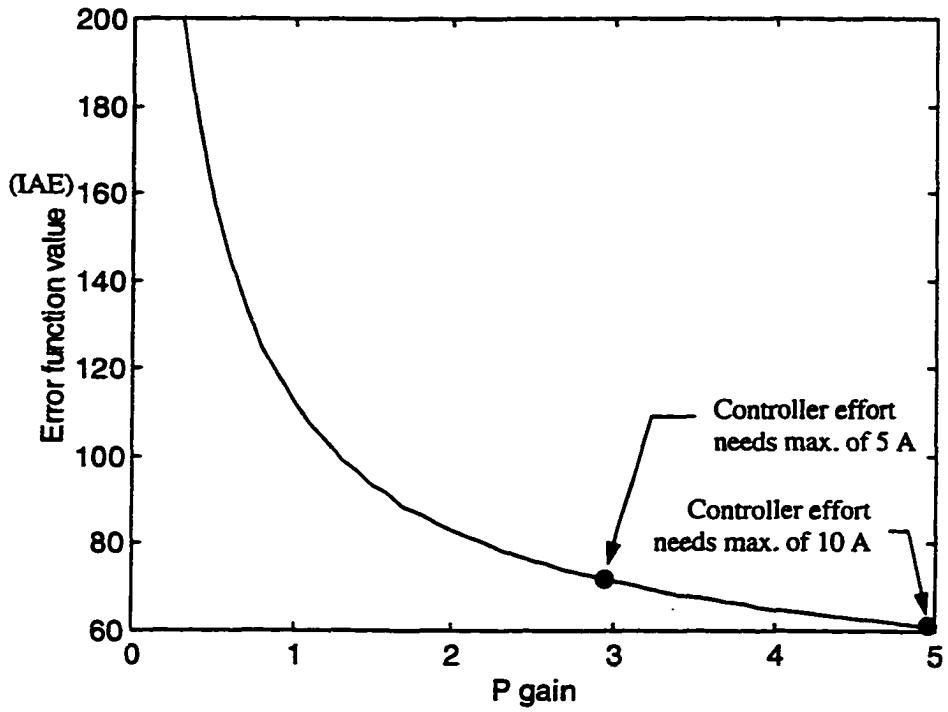

Figure 3-3 The valley bottom shown in Figure 3-2 tends to go down while P gain is increasing

Figure 3-4 shows a top view of the triangular valley of Figure 3-1 and its surrounding areas, it illustrates how this triangle is located in PD gain domain:

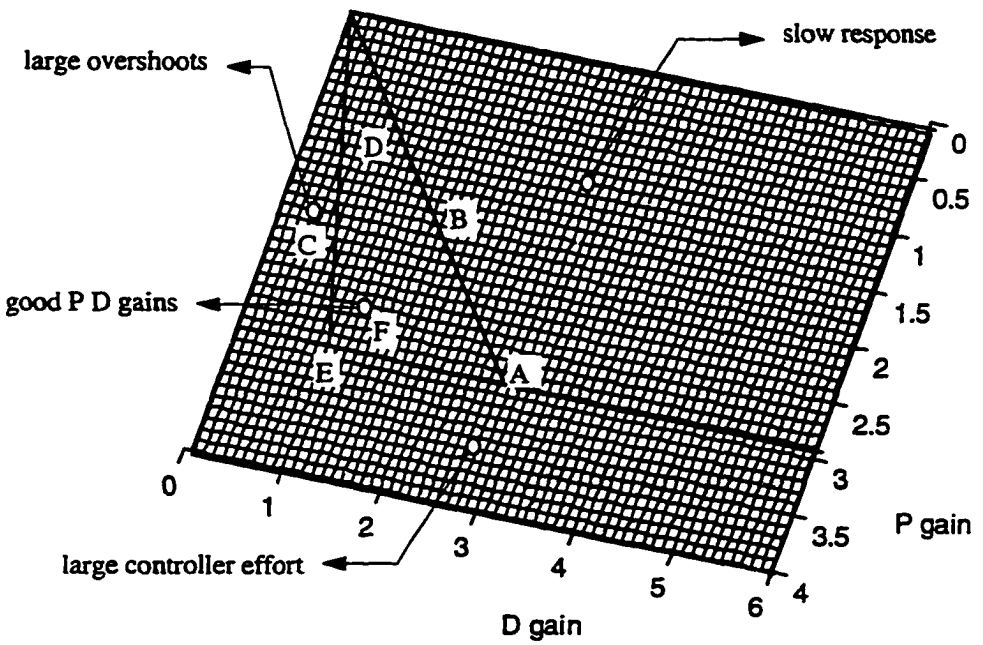

Figure 3-4 A top view of good P D gain area and surrounding areas

As shown in Figure 3-4, the left area covers where response has large overshoot and the right area has sluggish response. On the bottom, a solid line located at P=2.9 indicates P gain cannot go over 2.9, because higher P gain will cause more than 5 A controller effort at the very beginning of the bump (with 100 degree slew: 5/(100/180*pi)=2.9). The methods to overcome this constraint include increasing motor current limit, or feeding in softer reference (trajectory) and so on.

Several cases, A B C D E F points shown in Figure 3-4, have been simulated using rigid body model obtained in Chapter 2 to illustrate the effects of P D gains on system performance. (To be consistent with experimental results, all the following simulations are using 100 degree slew.):

Case A: P=3 D=3. Since this point covers both right and bottom areas (see Figure 3-4), it has demerits of both slow response and large controller effort. The reference input, rigid body system response and controller effort are shown in Figure 3-5:

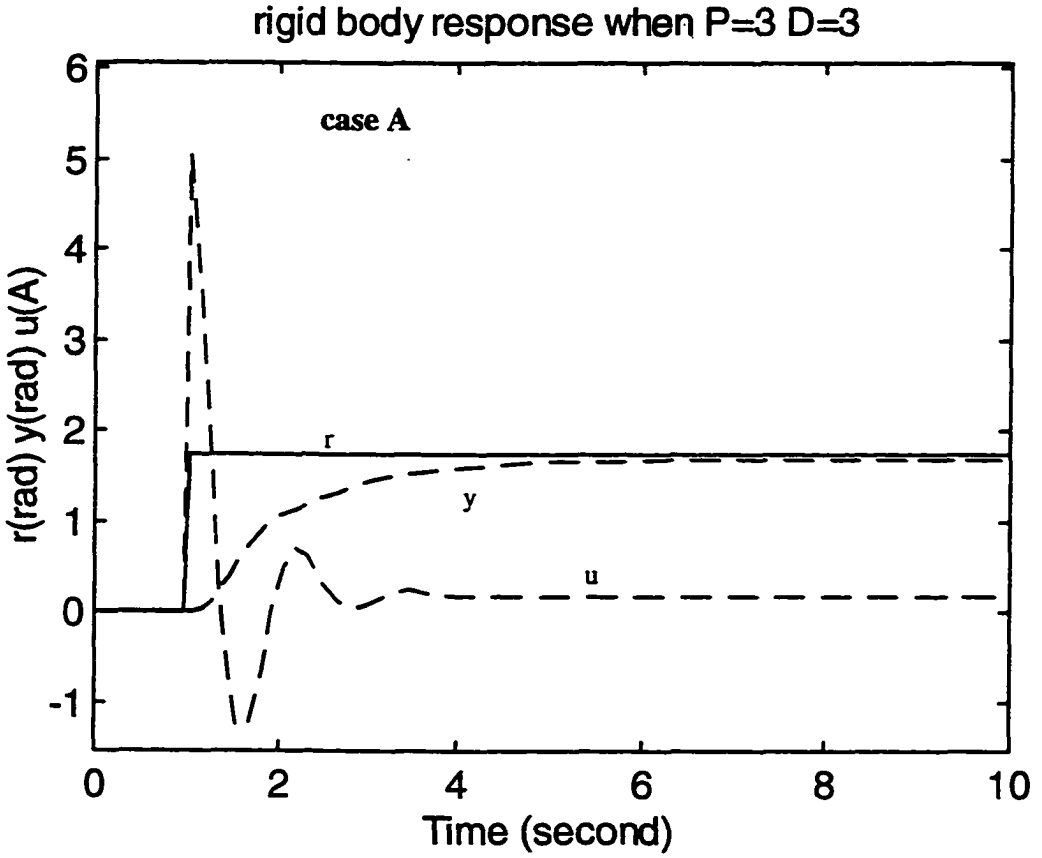

Figure 3-5 System performance and controller effort under P=3.0 and D=3.0

Case B: P=1.5 D=2. This point is at the right area (see Figure 3-4) and has slow system response as it is evident in Figure 3-6:

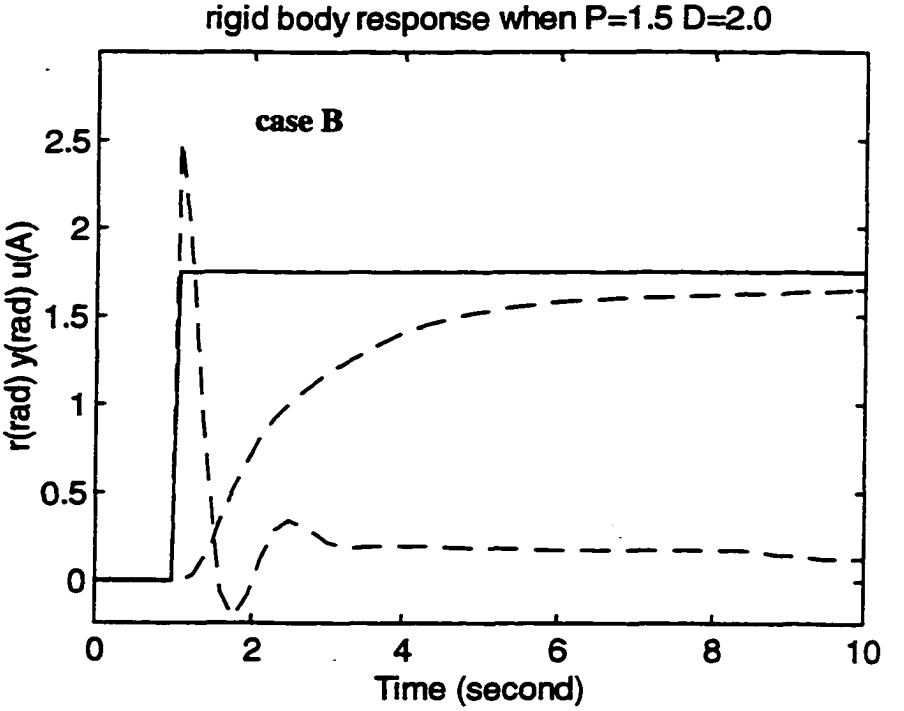

Figure 3-6 System performance and controller effort under P=1.5 and D=2.0

Case C: P=2.0 D=0.6. This point has large overshoot and the simulation results are shown in Figure 3-7:

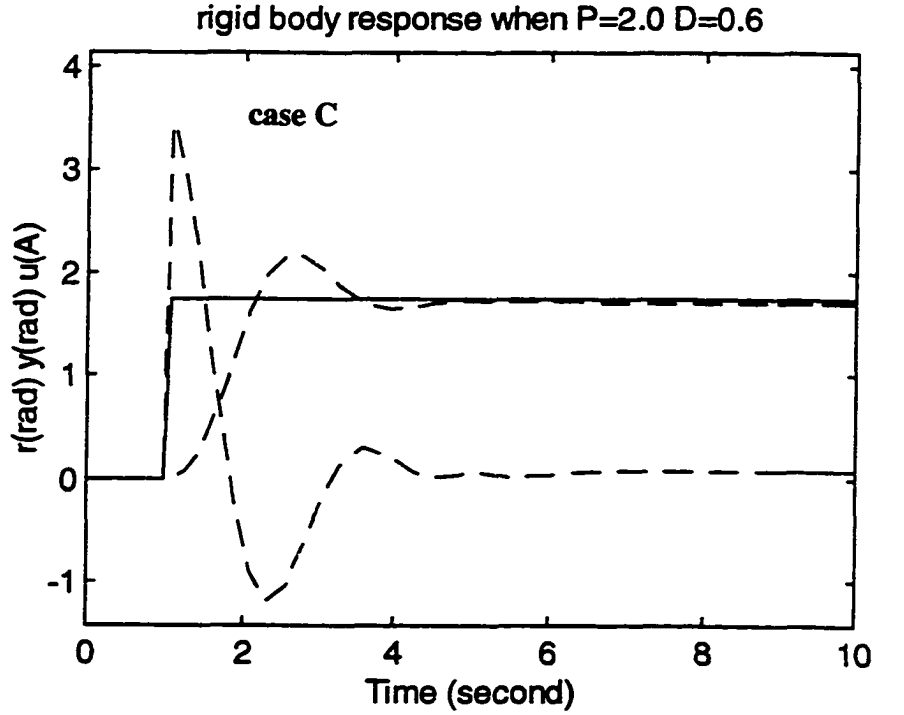

Figure 3-7 System performance and controller effort under P=2.0 and D=0.6

Case D: P=1.3 D=0.62. We used this point in Chapter 2 to identify the closed-loop rigid body system model. This point is within the triangle in Figure 3-4 and has reasonable performance, the controller effort is small as well. This simulation is shown in Figure 3-8.

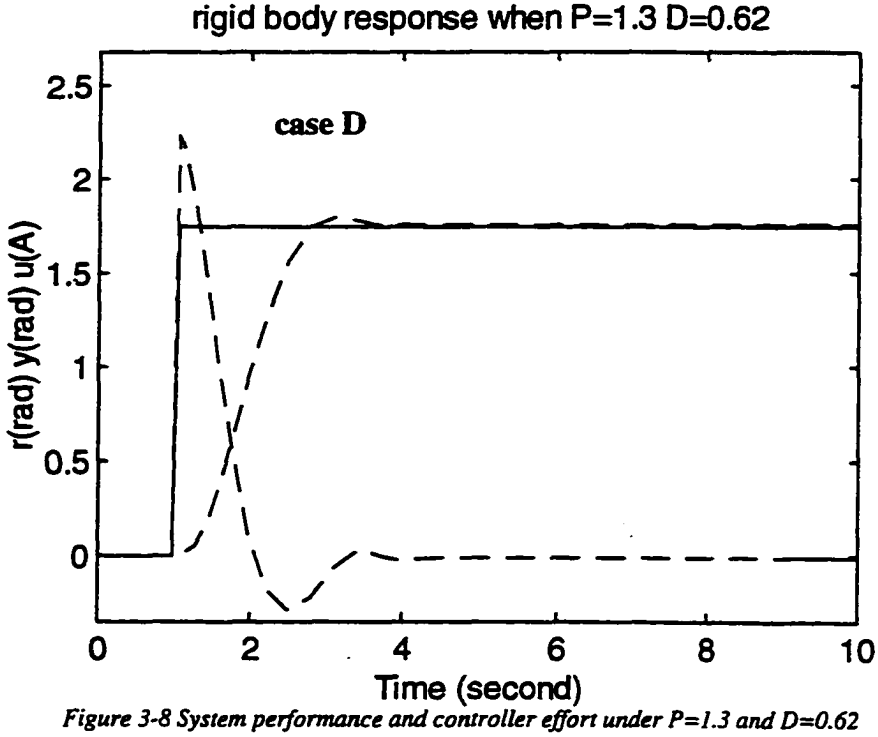

Figure 3-8 System performance and controller effort under P=1.3 and D=0.62

Case E: P=3.0 D=1.0. This point covers both the bottom and the left area in Figure 3-2, and has the performance of both high overshoots and high controller effort, as shown in Figure 3-9:

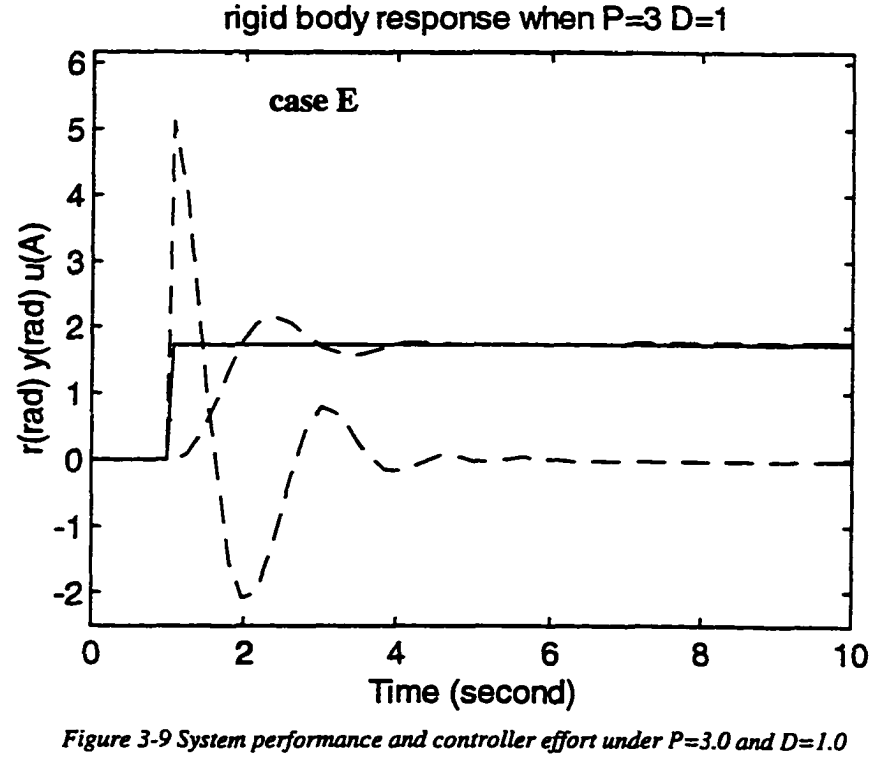

Figure 3-9 System performance and controller effort under P=3.0 and D=1.0

Case F: P=2.9 D=1.4. This point is the global minimum of all feasible areas. The controller effort takes a peak at exactly 5A, and step response error is very small, as seen in Figure 3-10.

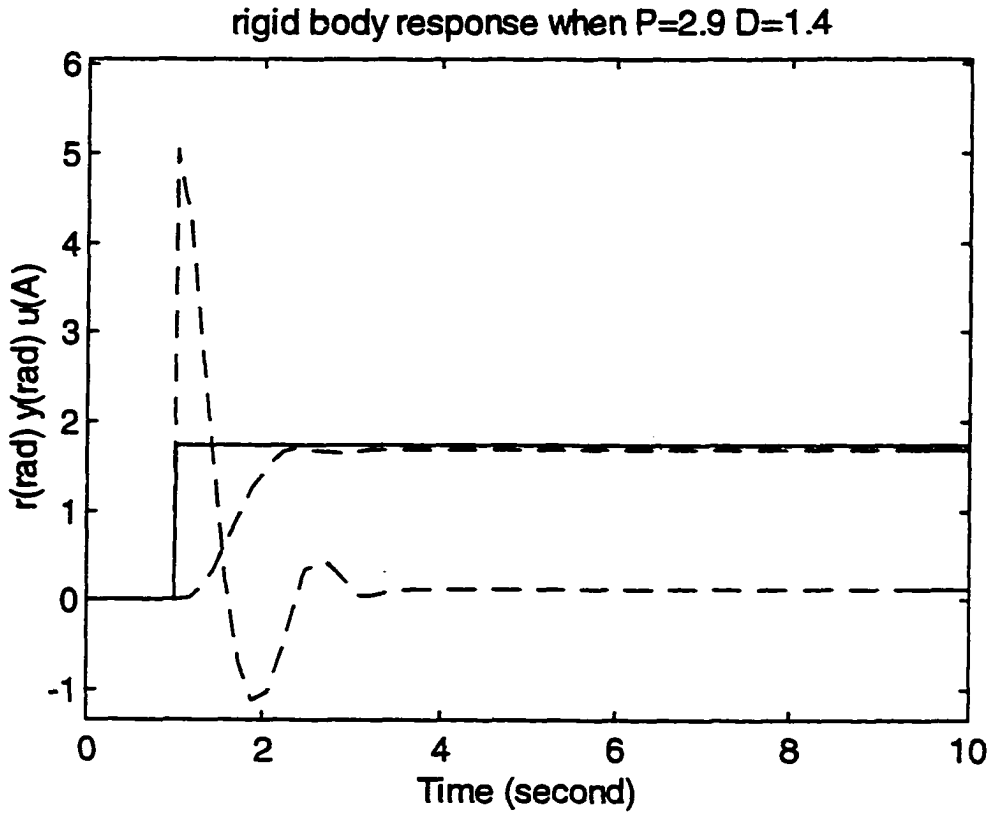

Figure 3-10 System performance and controller effort under P=2.9 and D=1.4,(global feasible minimum)

By comparing the Figure 3-10 with Figure 3-8 (P=1.3 D=0.62 used in Chapter 2), it can seen that system response is about 30% faster in this case. Since this gain setting shows promise for practical implementation, an experiment is conducted and compared with simulation results in Figure 3-11. The experiment uses the same P and D gain setting [2.9 1.4] as in simulation, a 100 degree reference step and 3 ms sampling period. The angle position and velocity measurements are noise-filtered before being fed back (the noise filter is detailed later in Equation 3-2.).

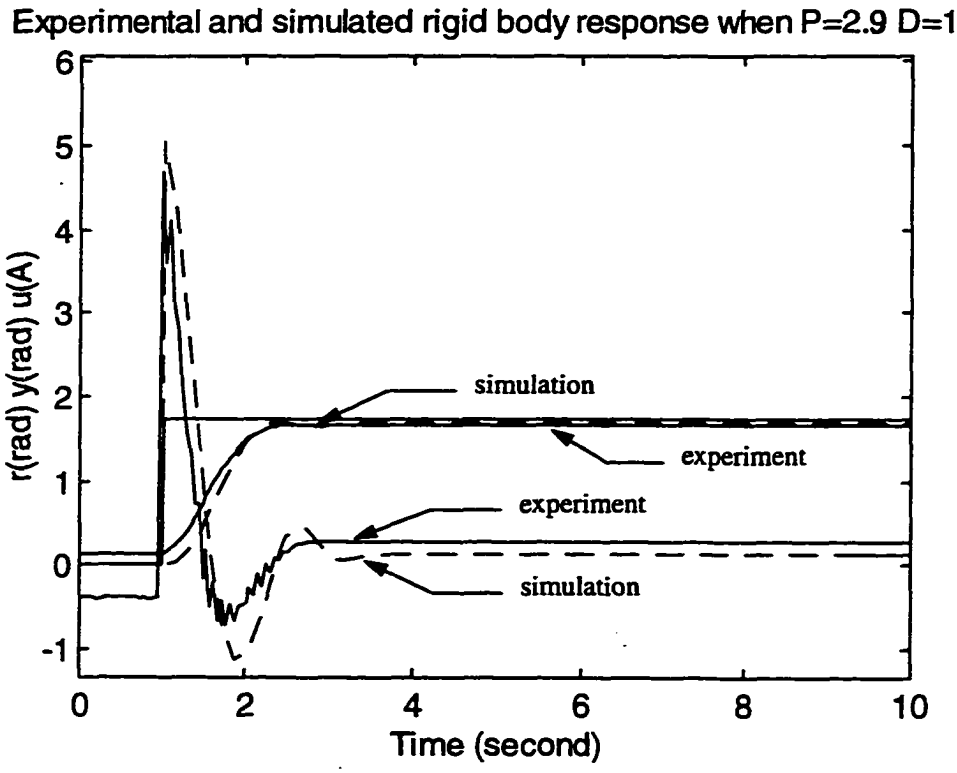

Figure 3-11 Comparison of simulated and experimental step response under P=2.9 and D=1.4

The experimental results shown in Figure 3-11 indicates PD gain setting of [2.9 1.4] produces very good system performance, for rigid body tracking. It confirms the global PD gain optimization. The PD gain setting [2.9 1.4] for rigid body control will be used in most cases hereafter in this thesis.

Next, various PD settings are compared in the frequency-domain. Figure 3-12 shows the difference in frequency response from reference input to controller effort under different PD gain settings. It is obvious in this figure that greater PD gains have larger amplification of high harmonics. Also it is noticed that frequency response peaks of feasible P, D gains (up to [5 2]) are still far away from first-mode resonant frequency (around 8 Hz as studied in Chapter 2), therefore too weak to cause substantial first-mode resonance of manipulator beam deflection.

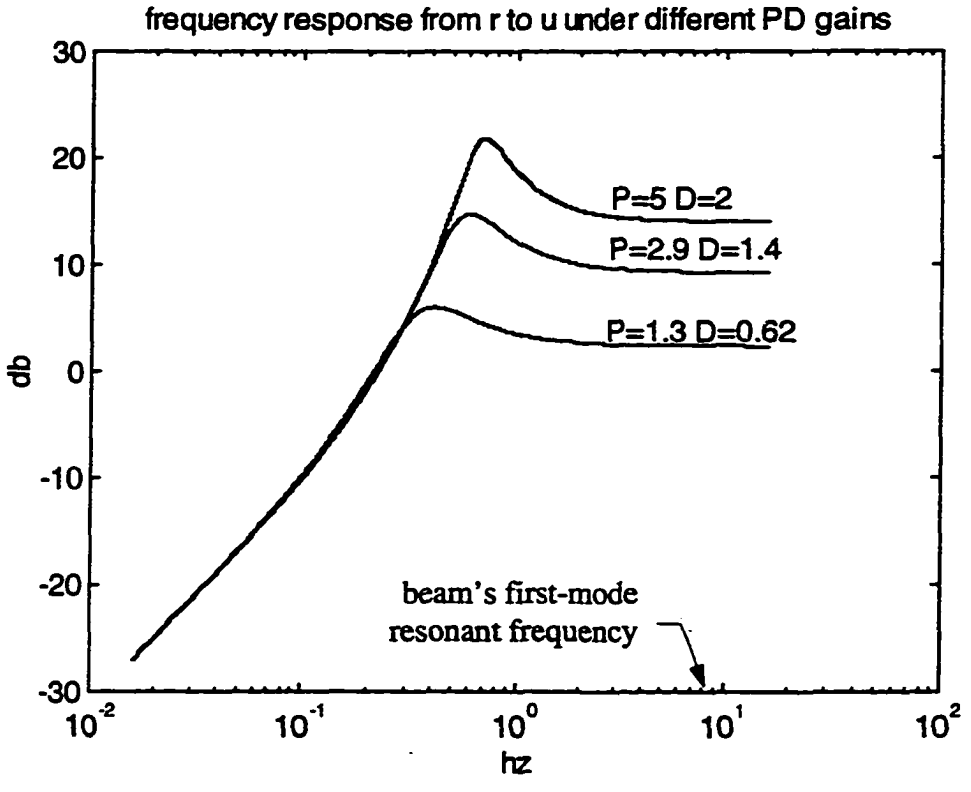

Figure 3-12 Comparison of frequency response from reference input to controller effort under different PD gains

It can be noticed in Figure 3-11 (and in most experimental PD controlling cases) that there is a steady state error which is due to Coulomb friction effects. A compromise for this problem could be to adjust P and D gains to make controller more aggressive. Suitable P and D gain settings can be found such that rigid body is stopped by Coulomb friction exactly at steady state. For example, adjustment of P D gain setting from [2.9 1.4] to [2.9, 1.2] completely cancels the steady state error shown in Figure 3-11 for the step of 100°. However, it is not a good solution in the sense that different reference input magnitudes need different adjustments of P and D gain setting (see Figure 3-15 where D=1.2 does not ensure good tracking for 60 degree slew).

It is usually possible to cancel this error by using an additional integral controller (I gain). However, demerits of using "double integrators" (system model has its own integrator) have to be considered.

After studying the nonlinear Coulomb friction model obtained in Chapter 2, a possible solution for this problem is a conditional I gain, i.e., the I gain and I effort are activated only when the error of the loop is within a certain small range, beyond which the error will be compensated by the P controller alone. This conditional I gain only handles the small error when corresponding P effort is too small to overcome Coulomb friction, which is the primary cause of steady state error. As experimentally identified in Chapter 2 (see Figure 2-25), Coulomb friction can only be overcome by any motor current beyond [-0.32 0.32] A, thus a reasonable error range would be [-0.32 0.32]/P_gain=[-0.11 0.11].

Experimental results in Figure 3-13 show how the conditional I gain (1.5 in this case) compensates steady state error caused by static friction for a step reference of 100°.

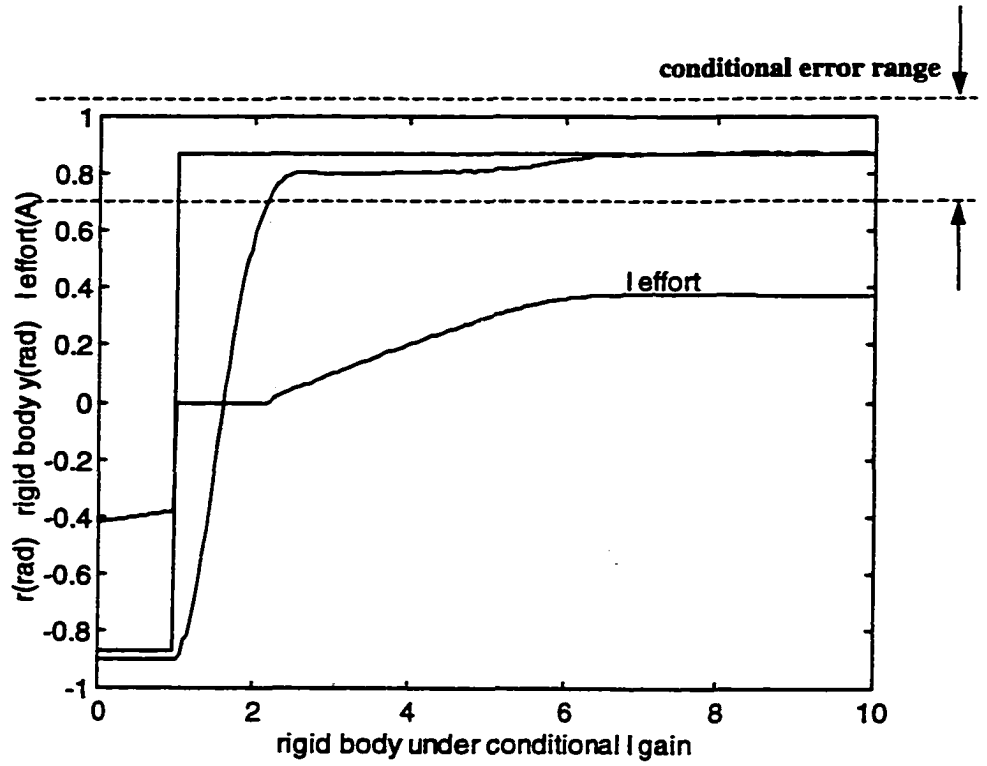

Figure 3-13 PD control with conditional I gain to cancel static error caused by friction

Figure 3-14 shows that the error eventually goes to zero over an extended time horizon. Small limit cycles due to Coulomb friction however are present.

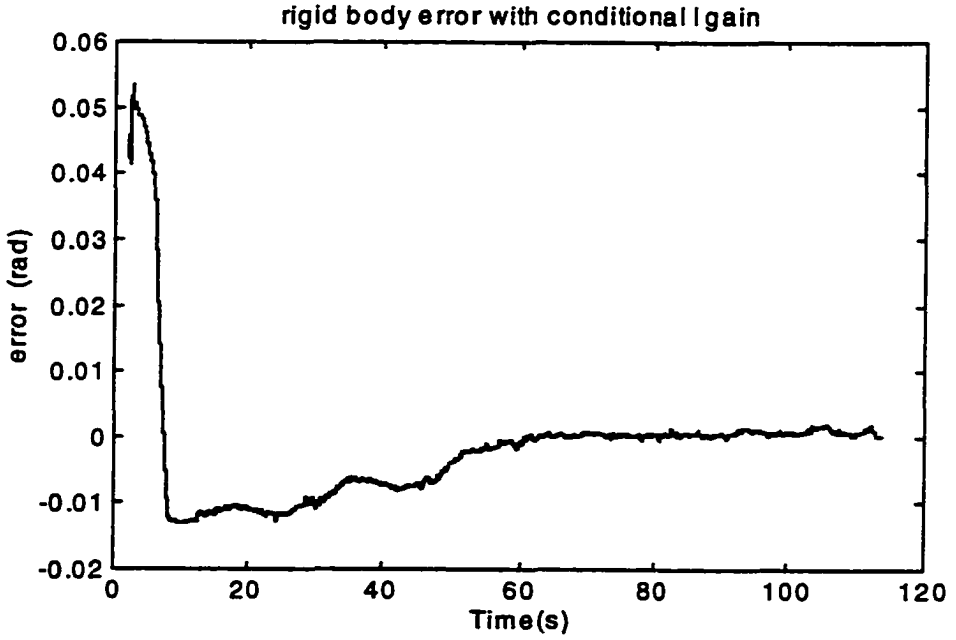

Figure 3-14 Steady state error compensation under conditional I gain

One advantage of conditional I gain is that it suits various reference input magnitudes. Figure 3-15 is the experimental results for a 60 degree step reference input.

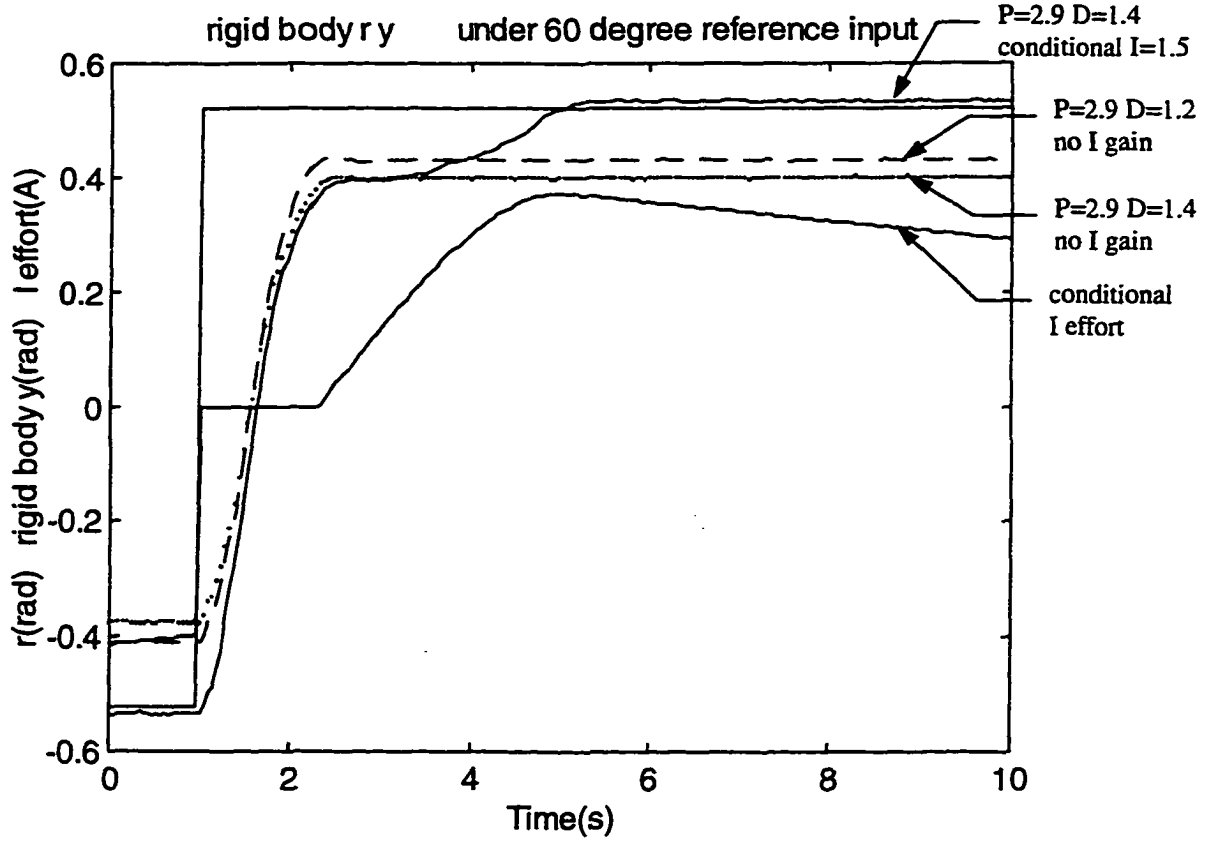

Figure 3-15 Experimental system response under 60 degree reference input, with different gain settings

Figure 3-15 shows that, the old P D gain setting of [2.9 1.4] with no I gain has steady state error, and adjusted P D gain setting of [2.9 1.2] can not solve that steady error in the case of 60° slew although it works for 100 ° case. On the other hand conditional I gain works for both cases. (Note that in the case of 60 ° reference input, one can select P gain higher than 2.9 as motor current limit is not reached and therefore system could have even faster response than shown in Figure 3-15.)

Another supplementary option, also an efficient method, for steady state error compensation in the smaller reference input cases is the addition of dither [23], i.e. add a periodic signal with certain magnitude and frequency on the controller effort. This method proves to be helpful especially when reference slew is small, and has the side-effect of causing small beam oscillations (which is picked up by the strain gauges.).

In Figure 3-16, an experiment is conducted to show how dither improves system performance. P and D gains are 2.9 and 1.4 in this case, reference input is 30 degree slew and dither is added as a sine wave with magnitude of 0.35A and frequency of 11 Hz. The dither frequency is selected between the first and second resonant frequencies of beam

oscillations (see Chapter 2 Figure 2-14 2-19), a point where dither's effect on the strain picked up by the strain gauges is minimized.

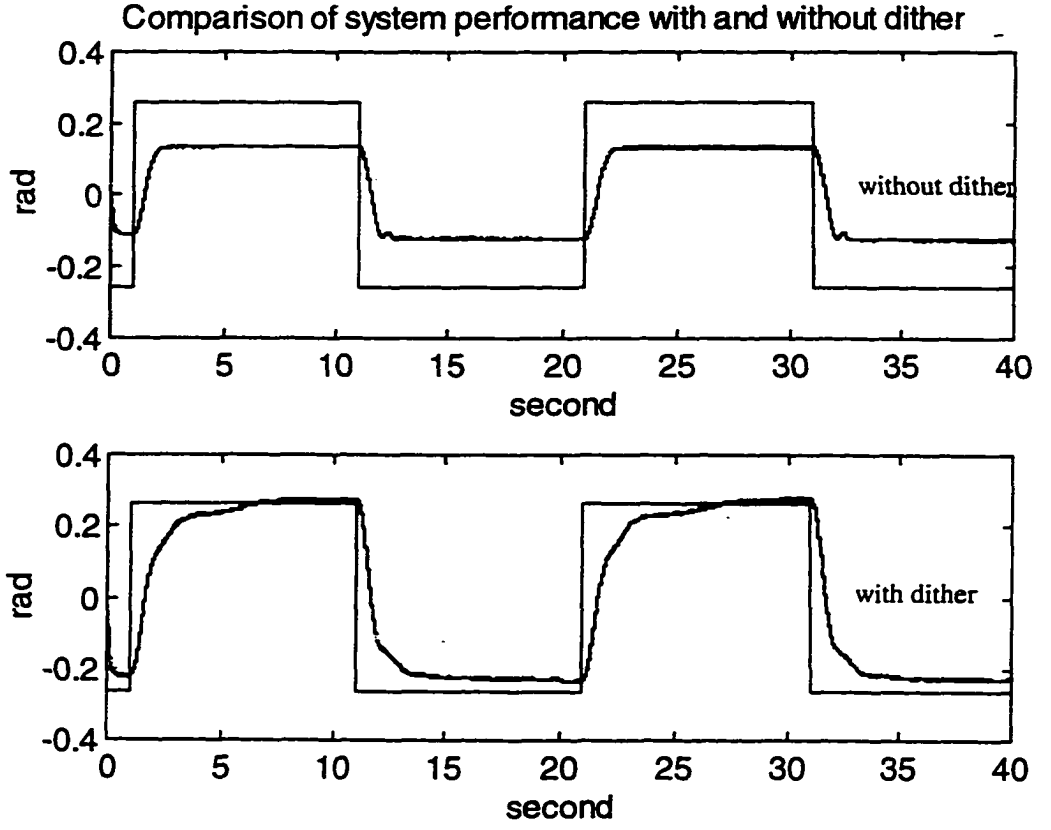

Figure 3-16 Comparison of system performance with and without dither

Dither is a good solution to eliminate steady state error especially at the upper direction of trajectory, as shown in Figure 3-16.

3.2 P Controller for Deflection Suppression

In Chapter 2, the goal of flexible-link manipulator control is defined as not only to ensure rigid body tracking, but also that tip deflections due to manipulator flexibility be suppressed. In most industrial cases, it is particularly desired that flexible tip deflection should settle down quickly after rigid body reaches its steady state, in order to improve work efficiency (and avoid possible physical damage). From an experimental point of view, the problem is to suppress base/second strain gauge measurements, which reflects stress on the beam, to zero. Section 3.1 partially solves the control problem by searching for high P and D gains for rigid body control, on the other hand, it also poses some severe problem on deflection control because high P and D gains increase oscillations. This is revealed by strain gauge measurements in Figures 3-17 and 3-18:

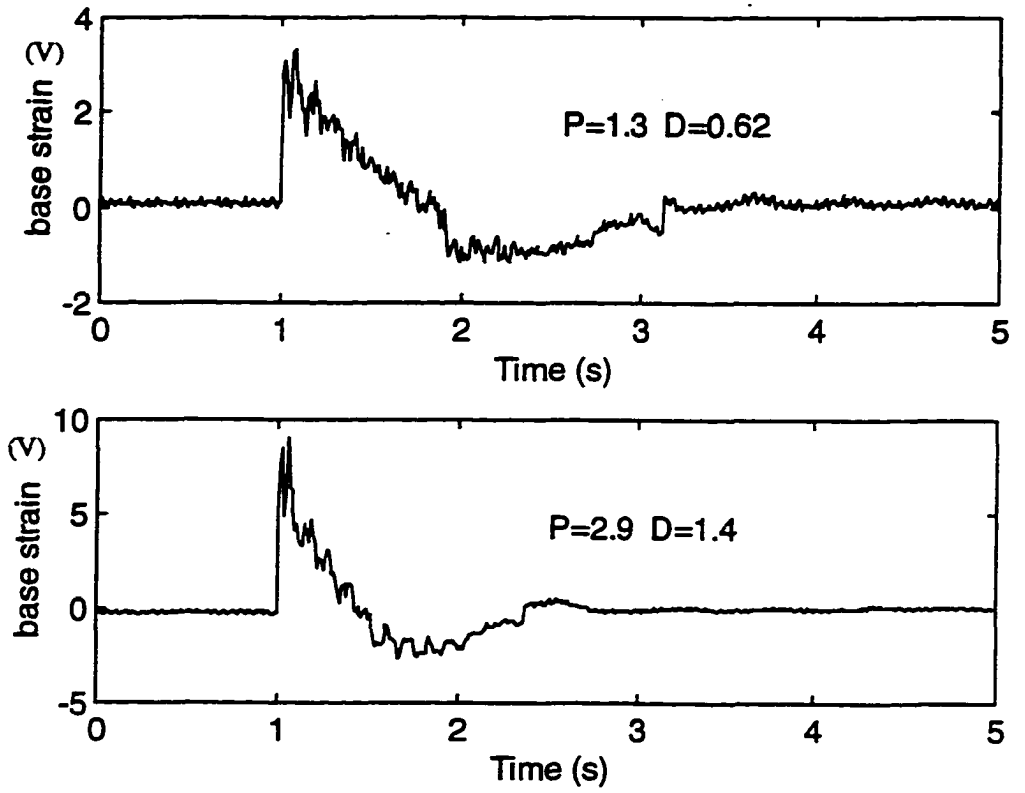

Figure 3-17 Comparison of base strain gauge measurement under different rigid body gain settings

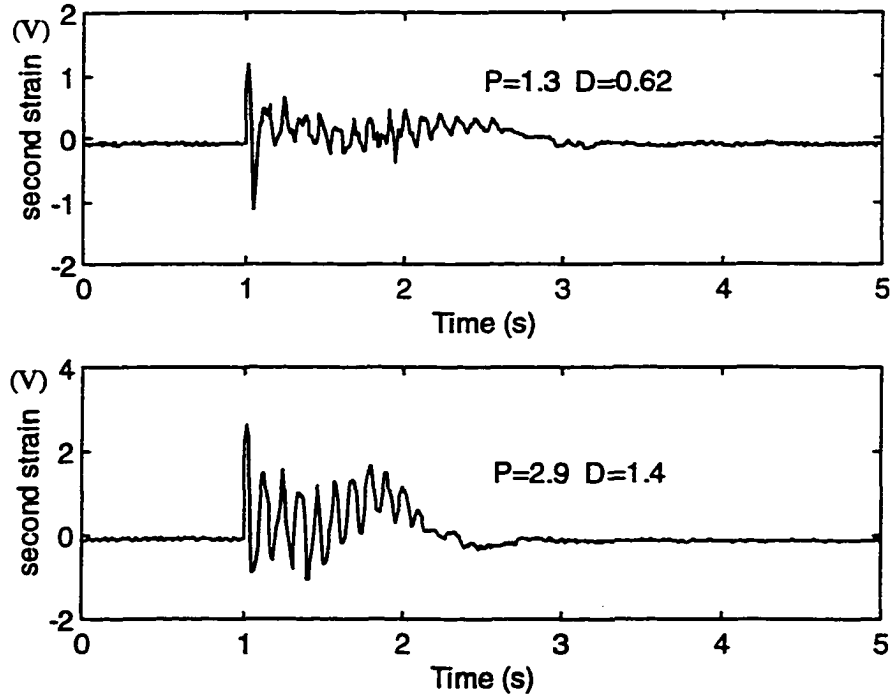

Figure 3-18 Comparison of second strain gauge measurement under different rigid body gain settings

The PD gain of [2.9 1.4] makes second strain gauge measurement 2 times greater than the [1.3 0.62] gain setting, and even 3 times greater at base strain gauge measurement, as shown in above figures. An effective control to suppress beam tip deflection/vibration is highly demanded.

Previous research [3] has found that tip acceleration proportional feedback is appropriate for tip deflection/vibration suppression. In our case beam strain measurements used for feedback performs acceleration feedback: strain gauges pick up information of strain at the surface of manipulator beam, which is proportional to stress inside the beam, which is in turn proportional to flexible body acceleration. Thus a proportional feedback of base/second strain gauge measurement is in fact proportional feedback of acceleration, and will be effective in suppressing tip deflection/vibration.

However, in most flexible-link manipulator control studies [2, 3, 4, 5, 6, 7, 12, 19, 20, 21], feedback of strain information is either not applied or the feedback gains are very small because high feedback gains on strain measurements would destabilize the whole system. As a result, the beam deflection/vibration suppression control obtained in previous literature is fairly weak. How to increase beam strain feedback gains (without reducing the stability of the system) to achieve high suppression of beam tip deflection/vibration has been a complicated problem in flexible-link control.

An efficient solution to increase strain measurement feedback gains is offered in this thesis by using a second-order low-pass filter on second strain gauge measurement before it is

fed back. So the entire control design developed for the flexible-manipulator is a PIDP combination, as illustrated as Figure 3-19:

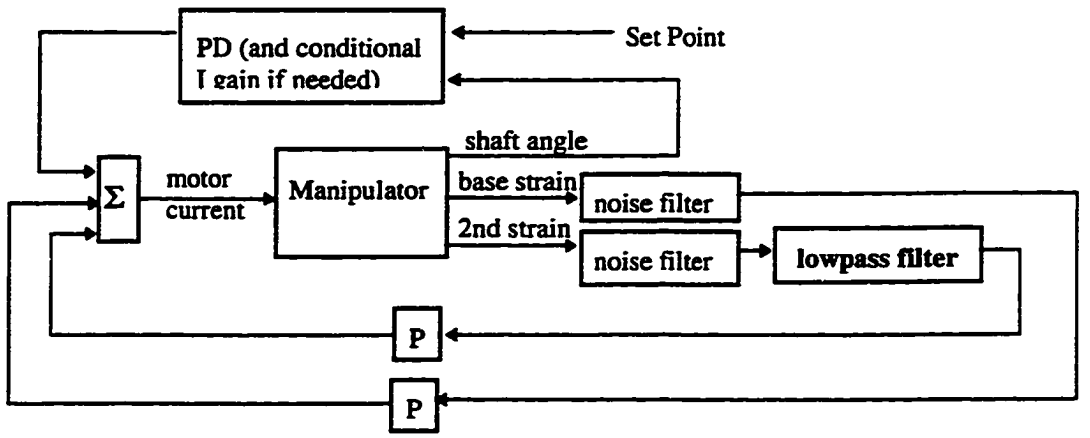

Figure 3-19 The schematic of the whole PIDP controller

Under such a PIDP controller, feedback gains on strain gauge measurements can take much higher values, and both deflection and oscillation of manipulator are greatly suppressed (without reducing the performance and stability of rigid body). An experiment is conducted on PIDP control with low-pass filter to illustrate its improvement over PID control as used in Section 3.1. Figures 3-22, 3-23 and 3-24 show system performance under the PIDP controller (with strain gauge feedback) and under PID controller (no strain gauge feedback).

In the PIDP control case, proportional gain on base strain feedback is 0.7 and proportional gain on second strain gauge feedback is 1.3, both base and second strain gauge measurements are noise-filtered before being fed back (see noise filter detailed later in Equation 3-2). And a second-order low-pass filter is used before feeding back second strain gauge measurement. PD controller applied on rigid body has gain setting of [2.9 1.2], conditional I gain is 1.5 and sampling period is 3ms. The gain setting for the experiment is as shown in Figure 3-20:

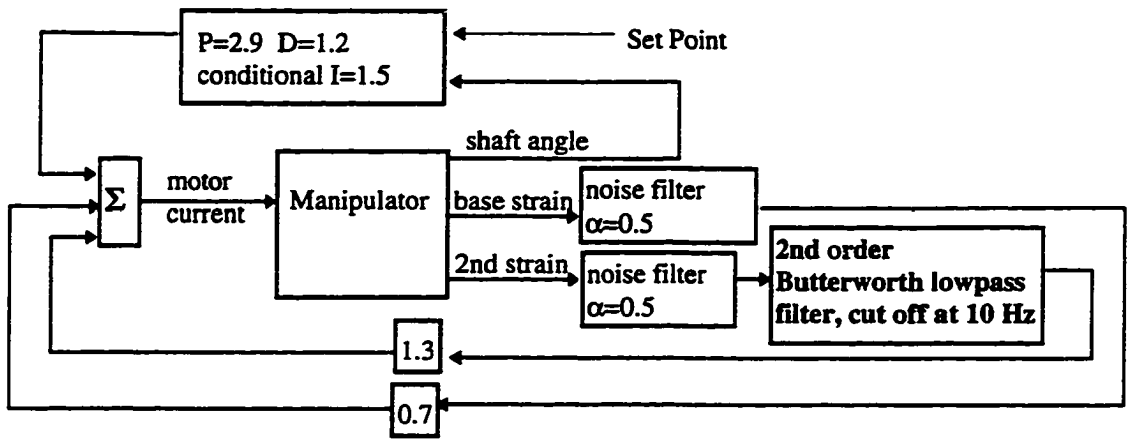

Figure 3-20 Gain settings for PIDP control experiment

In the PID control case, PD controller and conditional I controller have the same gain settings as PIDP, except proportional gains on base/second strain are not applied. Its gain setting is as shown in Figure 3-21:

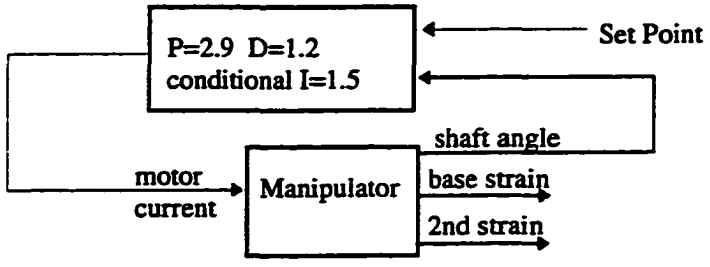

Figure 3-21 Gain setting for PID control experiment

It can be observed from the experimental data that both deflection and vibration of manipulator are greatly suppressed by adding strong P gains on strain measurements. Also the manipulator oscillations as picked up by the strain gauges takes less time to settle down in this case. It is also observed in experiments that the manipulator produces far less acoustical noise when using this kind of strain feedback.

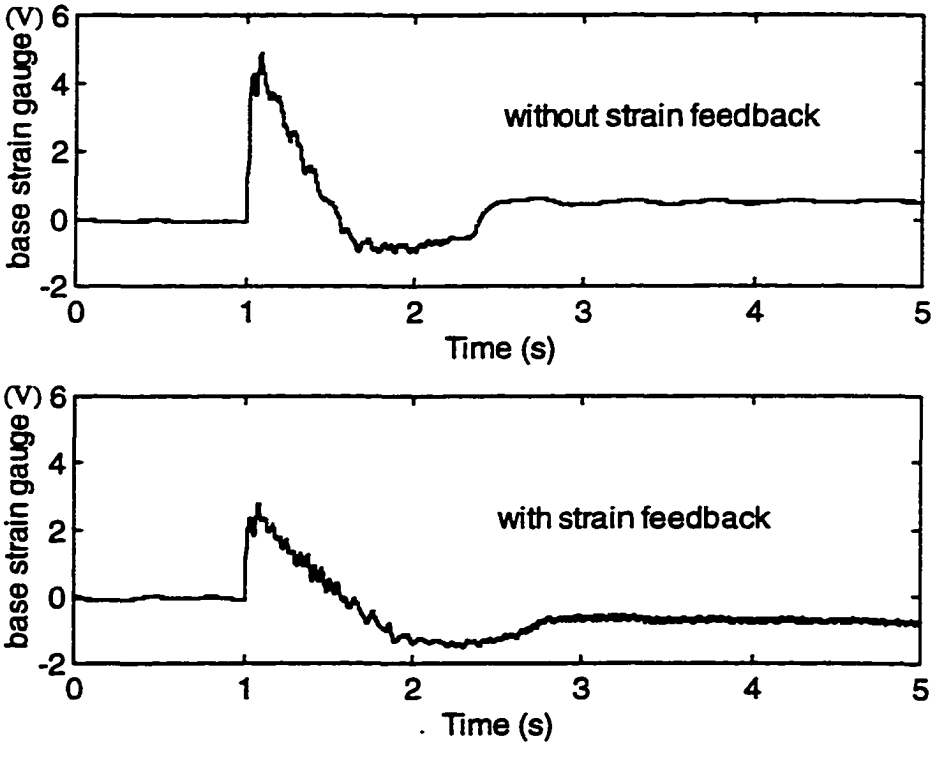

Figure 3-22 Comparison of base strain gauge measurements without (PID control) and with (PIDP) strain feedback

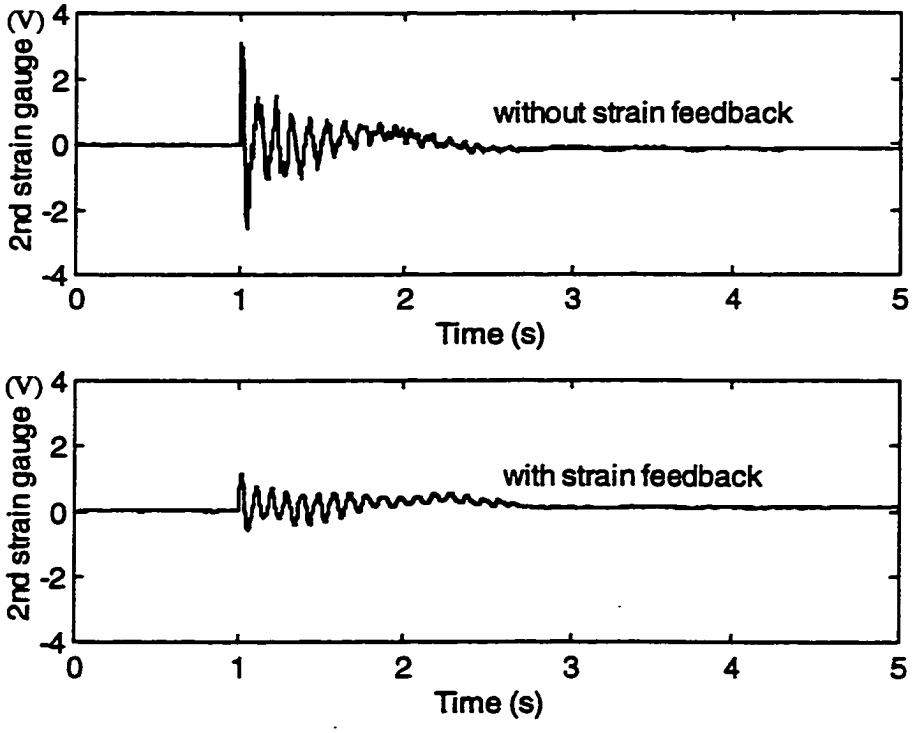

Figure 3-23 Comparison of 2nd strain gauge measurements without (PID control) and with (PIDP) strain feedback

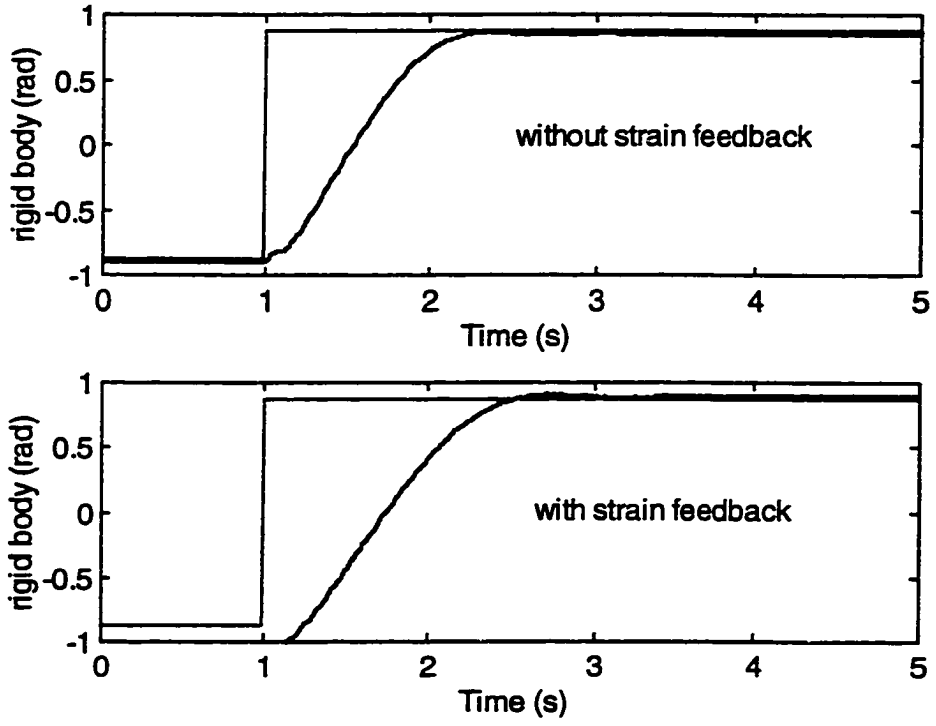

Figure 3-24 Comparison of rigid body response without (PID control) and with (PIDP) strain feedback

Figure 3-25 shows the result of processing of the second strain gauge measurements.

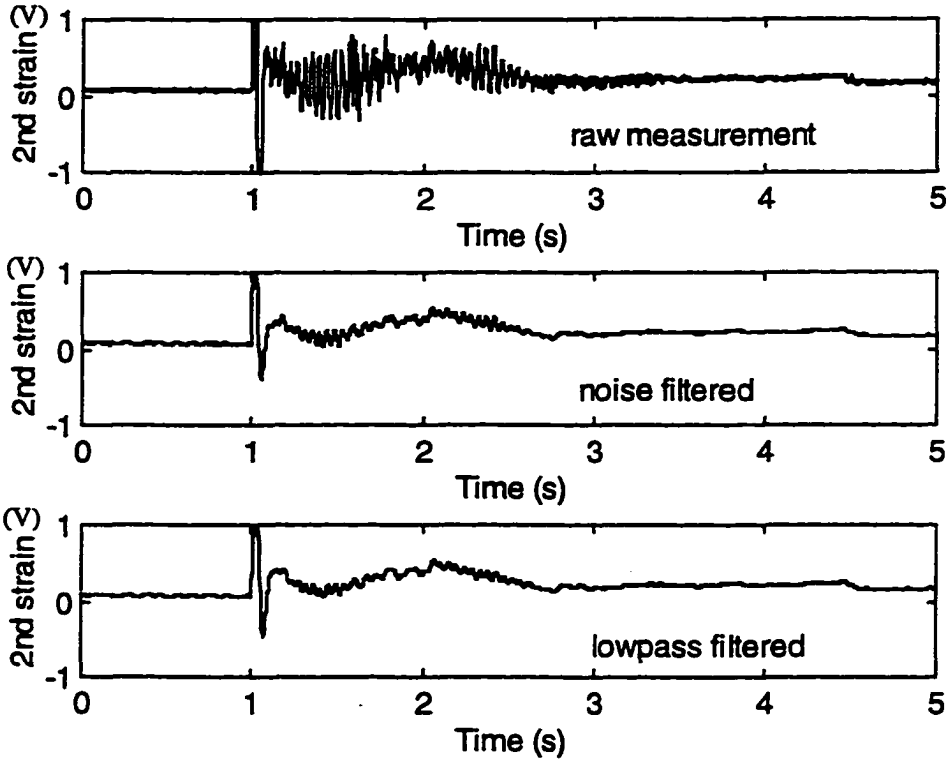

Figure 3-25 Information filtering of second strain gauge measurement before feeding back

PIDP control has visible advantages over PID control since it uses high P gains on strain feedback to suppress manipulator tip deflection/vibration, but it is also observed in the experiments that the low-pass filtering is essential for the entire control structure. As experiments prove, system loses stability under the same feedback gain setting without using the low-pass filter.

Why feedback gains on strain gauge measurements can be substantially increased by using a low-pass filter is now explained as follows:

With reference to Figure 3-19, the open-loop system frequency response consists of two parts: rigid body transfer function plus PD controller, and strain measurement transfer functions plus P controllers. Based on this open-loop model, system's Nyquist plots are compared in Figure 3-26 (without low-pass filter) and Figure 3-27 (with low-pass filter), the influence of low-pass filter in improving stability margins can be seen clearly. Without low-pass filter (i.e. proportional control is applied on strain measurements directly), system's Nyquist plot under P gain of 1.3 on second strain gauge measurement is given in Figure 3-26. The low phase margin in this plot is evident. Practical implementation causes the system to become unstable.

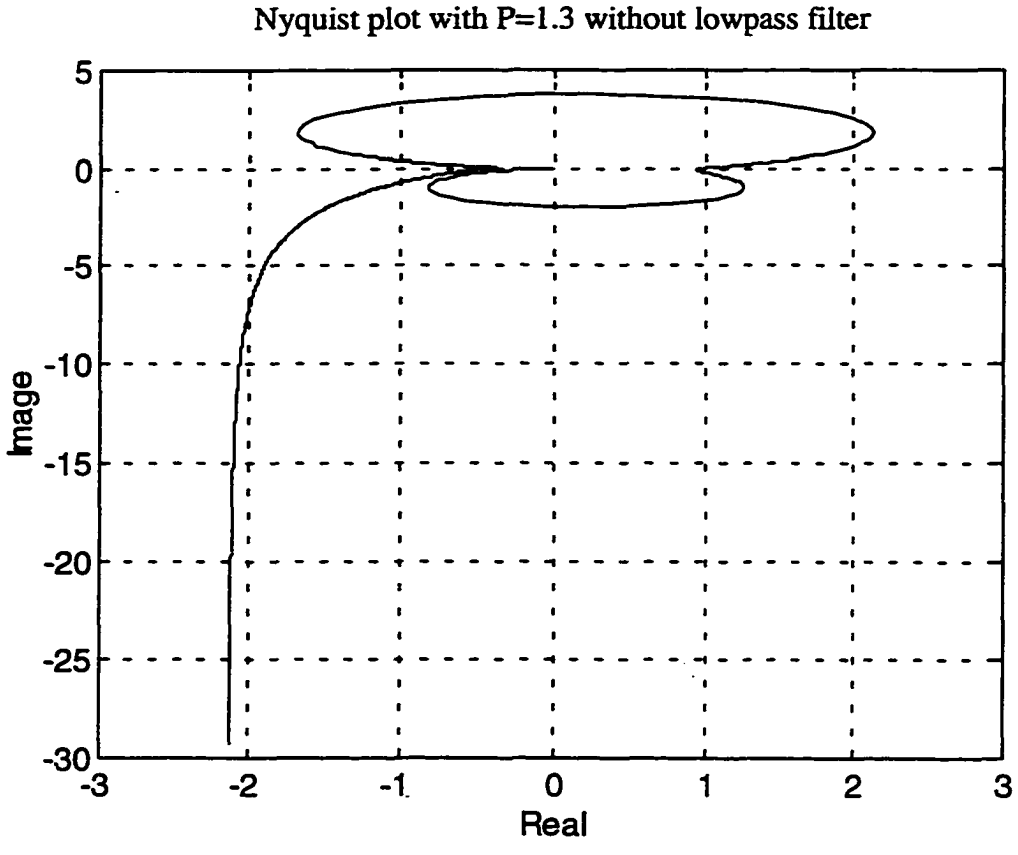

Figure 3-26 System's Nyquist plot under P=1.3 without low-pass filter

On the other hand, if the low-pass filter is used before the P gain of 1.3 is applied on the second strain gauge measurement, the system's Nyquist plot changes to Figure 3-27.

High phase margin and good gain margin are evident from Figure 3-27.

It is observed from experiment that higher base strain gauge feedback gain helps to suppress the initial peak amplitude of base/second strain (deflection magnitude), and higher second strain gauge feedback gain helps to suppress the oscillation magnitude of base/second strain after the arm begins to move. Although the Nyquist plots reveal that higher P gain may be used from stability point of view, the rigid body motion begins to slow down with higher P gains.

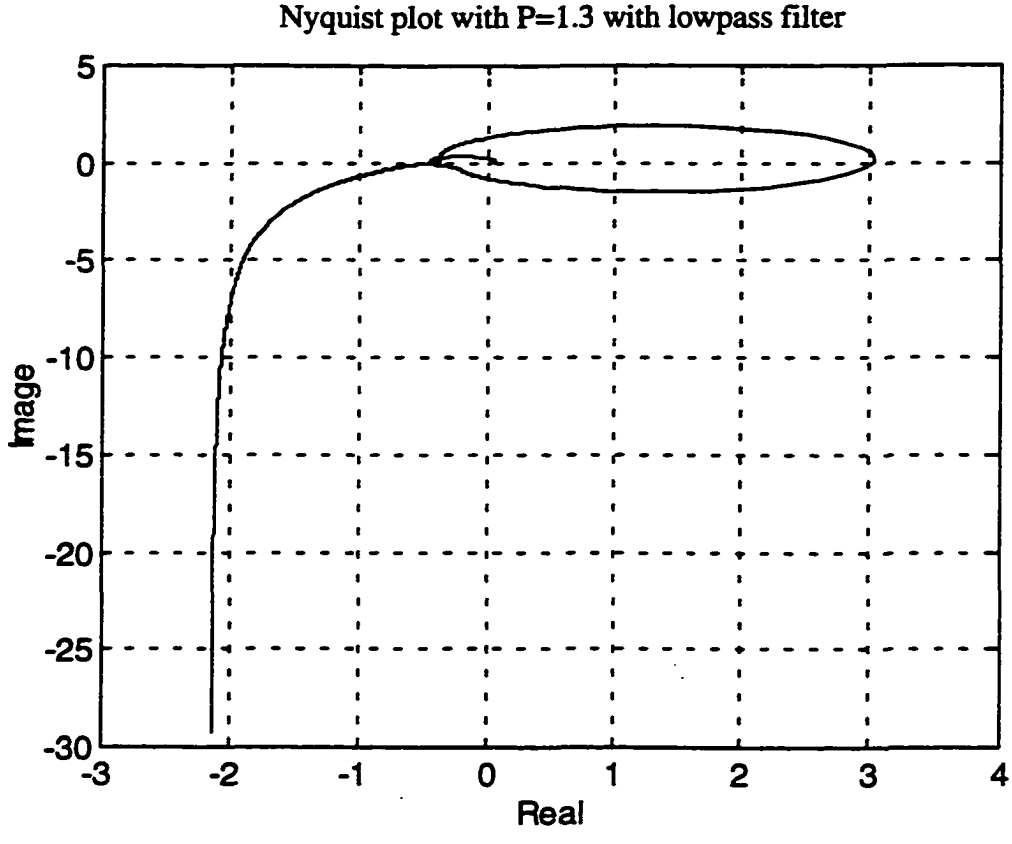

Figure 3-27 System's Nyquist plot under P=1.3 with low-pass filter

Also as shown in Figure 3-19, the information of base/second strain gauge measurements are noise-filtered before feeding back. Noise-filtering of sensor information, especially on strain gauges, helps greatly in reducing noise and improves system performance. The principle of these noise-prefilter is that the filter only partially accepts the new measurement as per Equation 3-2. The noise filter serves as a first-order lowpass filter.

$$X(k) = X(k-1) + \alpha*(X(k)-X(k-1)) \quad (3\text{-}2)$$

The updating coefficient α in Equation (3-2) is typically 0.5. High sampling frequency in experiments guarantees noise-filtered measurements do not lose "true information" albeit the phase shaft introduced by the noise filter can be destabilizing.

Figure 3-28 shows the appearance of unfiltered and noise filtered base strain gauge measurement with α=0.5:

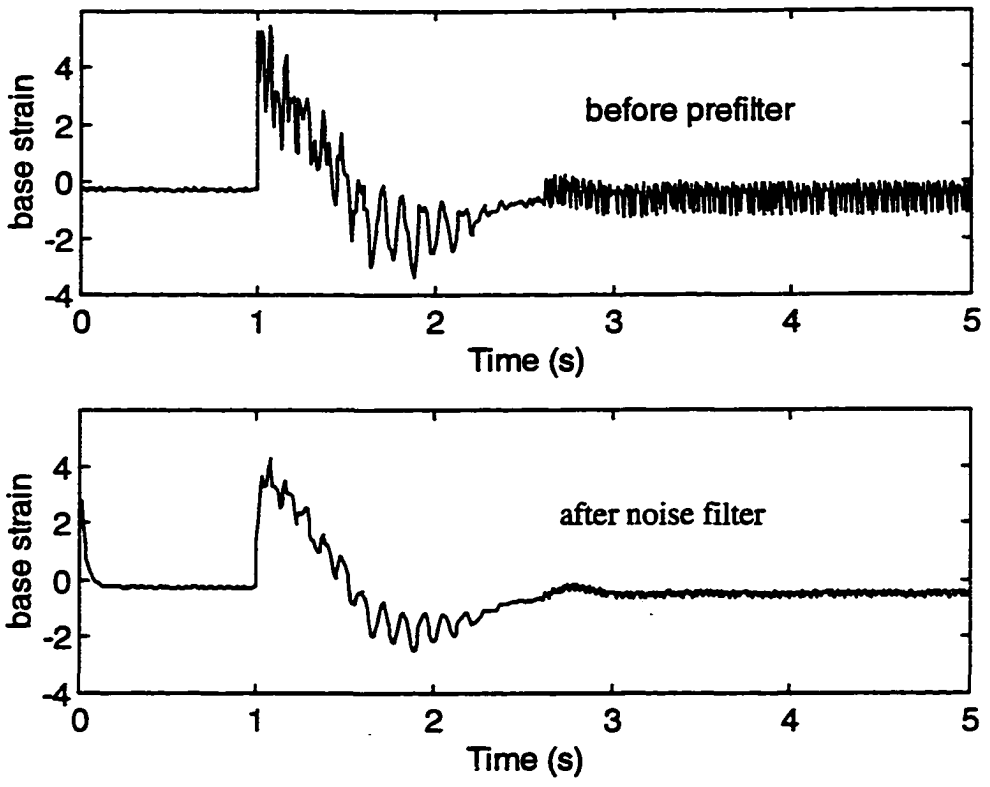

Figure 3-28 Comparison of unfiltered and filtered base strain gauge measurement

As shown in above figure, the noise-filtered sensor information (bottom figure) doesn't lose any "true" information from the direct measurement (upper figure).

3.3 Discussion and Conclusions

In this chapter, a PIDP controller is implemented, and its experimental performance is shown. Its merits include fast rigid body response, accurate rigid body trajectory tracking, low overshoot (if any) and substantial tip deflection/oscillation suppression without reducing rigid body response and system stability. This experimental behavior is better than most results in the previous literature [2, 3, 4, 5, 6, 7, 12, 19, 20, 21].

The key contribution of the studies conducted in this chapter is the use of lowpass filtering on the second strain gauge to improve stability robustness which allows increased P gains for strain feedback. Experimental work and theoretical study show that direct feedback of strain gauge measurements without prefiltering will constrain P gains applied and therefore has little effect on deflection/vibration suppression.

Other contributions of this chapter include global optimization of PD control for rigid body motion using IAE method; applying dither and conditional I control to overcome steady state error caused by mechanical friction, particularly in the case of small reference inputs.

Chapter 4

Exploration of LQR Control & VSSMC Control

In this chapter, LQR controller and VSSMC controllers are considered for the flexible link manipulator control, to seek better system performance than PIDP controller described in the last chapter.

4.1 Linear-Quadratic Regulator (LQR)

The PIDP controller described in Chapter 3 is very successful at rigid body trajectory tracking and beam strain suppression. One of its natural improvements is expected to be by a LQR controller. By feeding back not only direct measurements but also their derivatives, by designing stable controller based on the knowledge of model, LQR controller is expected to be more effective.

The term "linear-quadratic(LQ)" is shorthand for "optimal linear regulator for a quadratic performance index." The LQ regulator is one of the most important results of modern control. Many practical problems can be cast in the LQ framework, and there are excellent numerical algorithms for the solutions to obtain the controller.

Assuming the system is expressed in a state space form:

$$\dot{X} = AX + Bu$$

$$Y = CX + Du \tag{4-1}$$

In the LQR, full-state proportional feedback is applied by: u=-K*X, where K is designed by minimizing a scalar performance index, of the form

$$J = \int_0^\infty [X^T(t)QX(t) + u^T(t)Ru(t)]dt \tag{4-2}$$

where Q and R are symmetric matrices and positive semidefinite and positive definite respectively.

The problem to be solved is assumed to be a regulation problem where the objective is to drive the state from some initial value to zero. The term $X^T(t)QX(t)$ penalizes departures of X(t) from zero. The penalty is quadratic, so large errors are penalized much more than small ones, and the integral term in Equation (4-2) accumulates the errors over time, so long-lasting departures from X(t)=0 are penalized more than short-lived ones. The term $u^T(t)Ru(t)$ is included to ensure that controller effort is not too high. Full-state proportional feedback gain matrix K is selected under the criterion of minimizing Equation (4-2).

In our case of flexible-link manipulator LQR control, state space X in Equation (4-1) and (4-2) is chosen to be ninth-order, which includes the linear transfer functions of rigid body, base strain and lowpass-filtered second strain of Equation (2-24). The states are:

- three state space variables [X(1) X(2) X(3)] represent the third-order rigid body linear transfer function G_R, where X(1) is the shaft angle position, X(2) is shaft angle velocity and X(3) is the acceleration;
- two state space variables [X(4) X(5)] represent the second-order base strain gauge linear transfer function G_2 (first mode only), where X(4) is middle strain gauge measurement and X(5) is its derivative.
- four state space variables [X(6) X(7) X(8) X(9)] represent the fourth-order second strain gauge linear transfer function which is obtained by the combination of the first mode of G_3 and the second-order lowpass-filter, where X(6) is the lowpass-filtered second strain gauge measurement, X(7) X(8) X(9) are its first-order, second-order, third-order derivatives, respectively.

The lowpass filter is included in this LQR description as it enhanced the performance of the PIDP controller described in Chapter 3 (see Section 3.2 for detailed discussion on lowpass filter on second strain gauge feedback). The objective of continuing to use it in this chapter is to further improve on the PIDP controller by using LQR.

The A, B, C, D matrixes in Equation (4-1) are calculated from Equation (2-24) and the knowledge of second-order lowpass-filter, their numerical values are shown in Equation (4-3):

$$\overset{*}{X}=\begin{bmatrix}\overset{*}{X}(1)\\ \overset{*}{X}(2)\\ \overset{*}{X}(3)\\ \overset{*}{X}(4)\\ \overset{*}{X}(5)\\ \overset{*}{X}(6)\\ \overset{*}{X}(7)\\ \overset{*}{X}(8)\\ \overset{*}{X}(9)\end{bmatrix}=AX+Bu=\overbrace{\begin{bmatrix}0&1&0&0&0&0&0&0&0\\0&0&1&0&0&0&0&0&0\\0&-4.2&-4.665&0&0&0&0&0&0\\0&0&0&0&1&0&0&0&0\\0&0&0&-2852&-6.6&0&0&0&0\\0&0&0&0&0&0&1&0&0\\0&0&0&0&0&0&0&1&0\\0&0&0&0&0&0&0&0&1\\0&0&0&0&0&-11259125&-289681&-7614&-98\end{bmatrix}}^{A}*\begin{bmatrix}X(1)\\X(2)\\X(3)\\X(4)\\X(5)\\X(6)\\X(7)\\X(8)\\X(9)\end{bmatrix}+\overbrace{\begin{bmatrix}0\\0\\9.5097\\0\\1025\\0\\0\\0\\5601928\end{bmatrix}}^{B}*u$$

$$Y=\begin{bmatrix}Y(1)\\Y(2)\\Y(3)\\Y(4)\end{bmatrix}=\begin{bmatrix}shaft\_angle\_position\\shaft\_angle\_speed\\base\_strain\\lowpass\_filtered\_second\_strain\end{bmatrix}=CX+Du=\overbrace{\begin{bmatrix}1&0&0&0&0&0&0&0&0\\0&1&0&0&0&0&0&0&0\\0&0&0&1&0&0&0&0&0\\0&0&0&0&0&1&0&0&0\end{bmatrix}}^{C}*\begin{bmatrix}X(1)\\X(2)\\X(3)\\X(4)\\X(5)\\X(6)\\X(7)\\X(8)\\X(9)\end{bmatrix}+0*u$$

(4-3)

where X is the combined 9 state space variables described above. The above system was discretized at 3ms and with Q and R matrices selected as:

$$Q=\begin{bmatrix}8.4&0&1.6&0&0&0&0&0&0\\0&0&0&0&0&0&0&0&0\\1.6&0&0.4&0&0&0&0&0&0\\0&0&0&0&0&0&0&0&0\\0&0&0&0&0&0&0&0&0\\0&0&0&0&0&6&0&0&0\\0&0&0&0&0&0&0&0&0\\0&0&0&0&0&0&0&0&0\\0&0&0&0&0&0&0&0&0\end{bmatrix}\quad\text{and}\quad R=[1]$$

(4-4)

The gain K suggested by the discrete LQR algorithm is:

K=[2.72 1.29 0.40 0.0000 0.0000 1.03 0.05 0.0008 0.0000]

(4-5)

Q matrix plays an important role to obtain K matrix, it is selected by trial and error such that obtained K matrix will not require controller effort (motor current) larger than feasible limit (5A).

The first three elements of obtained K indicates feedback gains on rigid body, it differs from the PIDP controller studied in Chapter 3 in the sense that the third element indicates an acceleration feedback. The fourth and fifth elements of K are feedback gains on base strain gauge measurements. Since corresponding elements in Q are assigned as zero and system is adequately decoupled, they are both zero. The last four elements of K are feedback gains on lowpass-filtered second strain gauge measurements and its derivatives, it differs from the PIDP controller in the sense that it feeds back the filtered strain and its derivatives as well. It can be seen that this LQR controller is an extension of the PIDP controller.

In experiments, the initial state X(1) is set as (shaft_position-reference_input), and initial states of all other 8 elements are set as zero. The final steady states of 9 state space variables are all zeros. Thus the rigid body is designed to follow the reference input trajectory and beam strain is driven to zero.

Figure 4-1 illustrates the schematic of LQR control in experiments:

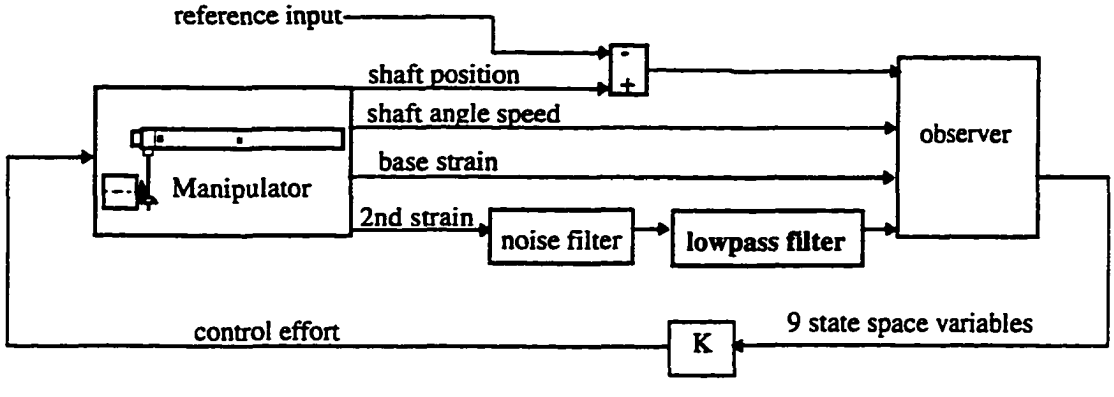

Figure 4-1 Schematic of LQR control

In above Figure 4-1, the noise filter and second-order lowpass filter are the same as used on PIDP control in Chapter 3 (see Figure 3-20).

The LQR controller usually requires a full-state observer to estimate the states of the system. However from Equation 4-3 it is seen that only states X(3) (rigid body acceleration), X(4) (derivative of base strain gauge measurement), X(7) (derivative of second strain gauge measurement) are not directly available. States X(8) and X(9) are available as they are states of the second order lowpass filter which is implemented in the computer. Since the base strain gauge measurements are not weighted by the controller gains, X(5) need not be estimated. Therefore only 2 states need to be estimated and these are expeditiously derived as approximate derivatives of X(2) and X(6) by computing the

difference of current measurement from previous measurement and dividing by sampling period. The sampling frequency for the LQR control system is 333 Hz (as before).

Figure 4-2 shows the experimental response of rigid body (shaft angle position) under LQR controller described above.

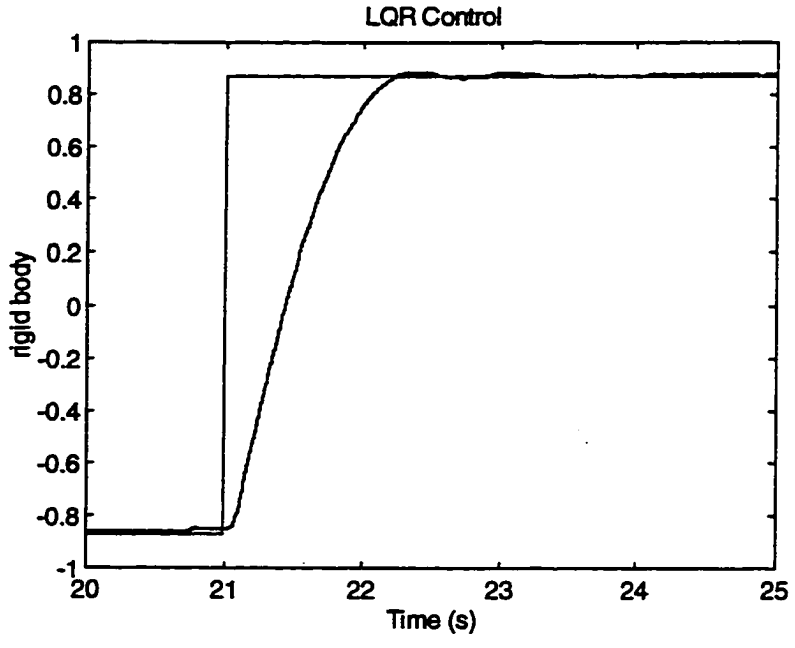

Figure 4-2 Rigid body response under LQR control

The speed of this response is slightly faster than that obtained under PIDP controller described in Chapter 3.

Under LQR control, the beam deflection/vibration is better suppressed than under PIDP controller in the same circumstance. Figure 4-3 shows the comparison of experimental second strain gauge measurements under LQR control and PIDP control:

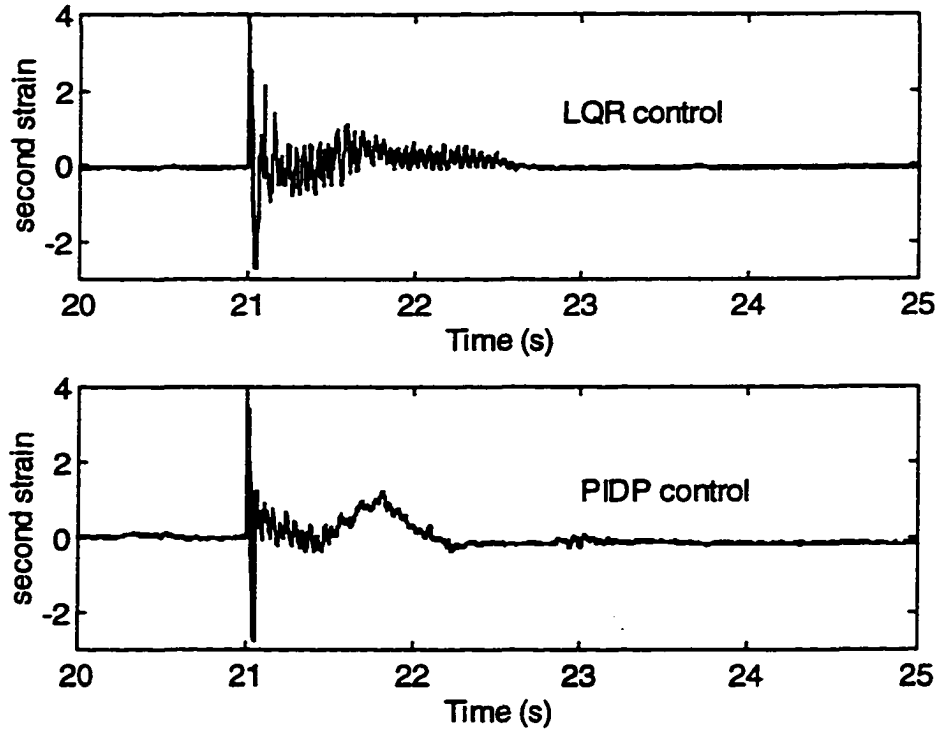

Figure 4-3 Comparison of second strain gauge measurements under LQR and PIDP controllers

It can be seen in Figure 4-3 that beam deflection under LQR control settles down earlier than that under PIDP control. To settle down beam tip deflection before or at least when rigid body settles is one of the demanding requirements in industrial applications.

As we learned in Chapter 2 and confirmed in all experiments, beam vibrations are visually comprised of first mode (8 Hz) and second mode (22 Hz) oscillation behaviors. It can be noticed in Figure 4-3 that 8 Hz oscillation behavior is greatly suppressed since we take the first mode transfer function into account while constructing LQR control structure. On the other hand, since the second mode transfer function is omitted in LQR control structure to reduce complexity, second mode (22 Hz) oscillation behavior is still active. This is obvious in Figure 4-3. In future research of LQR control, taking second mode transfer function into account to make a more elaborate LQR controller to suppress 22 Hz oscillation as well could be a challenging topic.

The effect of signal procesing on the second strain gauge measurement is shown in Figure 4-4:

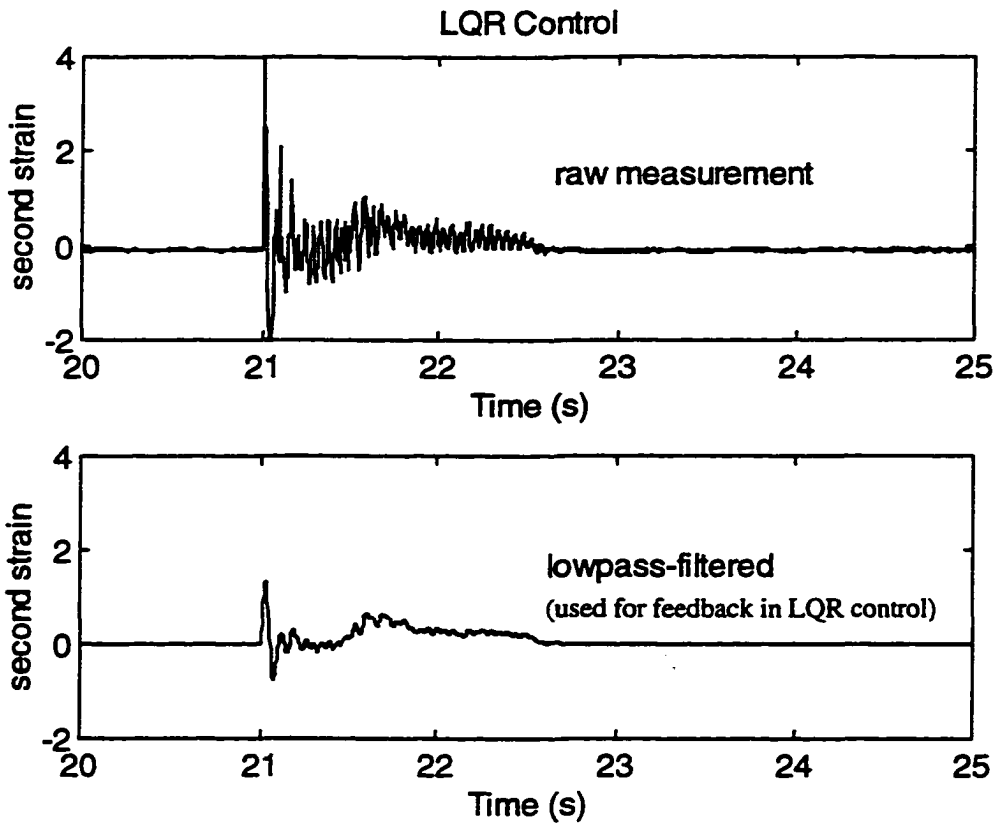

Figure 4-4 Signal processing of second strain gauge measurement before feeding back in LQR control

4.2 Variable Structure Sliding Mode Control (VSSMC)

The design principle of VSSMC [5, 6] is to establish a sliding surface in the state space of the system, and drive the system state space to 'hit' the sliding surface, and make it go down to origin (usually the final steady state) along the sliding surface (refer to Figure 4-7 for this process).

The design of VSSMC is divided into two steps:

1. design a stable sliding surface;
2. design a full state feedback gain setting to make sure $S\dot{S} < 0$ everywhere in the state space, so that system can be driven to this stable sliding surface from anywhere in the state space.

In step 1, a stable sliding surface may be designed by one of these two methods:

- calculate a sliding surface with the help of LQR theory;
- suggest a sliding surface by minimizing certain performance index and later prove this surface is stable;

The second method is chosen to design a sliding surface in this thesis since it gives us more freedom to optimize system performance. A preliminary design using rigid body transfer functions was carried out. The sliding surface S is a hyperplane in the variables shaft angle - reference, shaft angular velocity and shaft acceleration of the arm. The gains for the controller, to ensure the hitting of the sliding surface from any initial conditions, are generated in the usual manner [5, 6]. The approach taken herein is to use the integral absolute error (IAE as used in Chapter 3) on rigid body time-domain response to simultaneously design the sliding surface and the gains by a similar penalty function approach as in Chapter 3. Two issues are penalized in the algorithm :

- if any eigenvalue of sliding surface design is located on the right half plane (i.e. the sliding surface is not stable), the penalty function provides a high value;
- if value of $S\dot{S}$ is greater than or equal to zero at any state space (i.e. the system may not hit the sliding surface), the penalty function provides a high value.

A sliding surface (for rigid body VSSMC design only) is suggested by the algorithm as:

$$S = 1.0508*X(1)+0.2830*X(2)+0.0152*X(3) \tag{4-6}$$

where X(1) X(2) X(3) represent shaft angle position - reference input, angle speed, and angle acceleration respectively. The eigenvalues of this surface can be found from the characteristic equation $0.0152s^2+0.2830s+1.0508=0$ and are -13.496 and -5.1223 indicating a stable sliding surface. The gain settings in $u = KX$, as suggested by the algorithm are:

$$K(1) = \begin{cases} -0.0951 & SX(1) > 0 \\ 0.0987 & SX(1) \le 0 \end{cases}$$
$$K(2) = \begin{cases} -14.0131 & SX(2) > 0 \\ 1.4196 & SX(2) \le 0 \end{cases} \tag{4-7}$$
$$K(3) = \begin{cases} -9.7031 & SX(3) > 0 \\ 7.0533 & SX(3) \le 0 \end{cases}$$

Using this full state feedback strategy, simulated rigid body response is shown in Figure 4-5, where 100 degree reference step is applied:

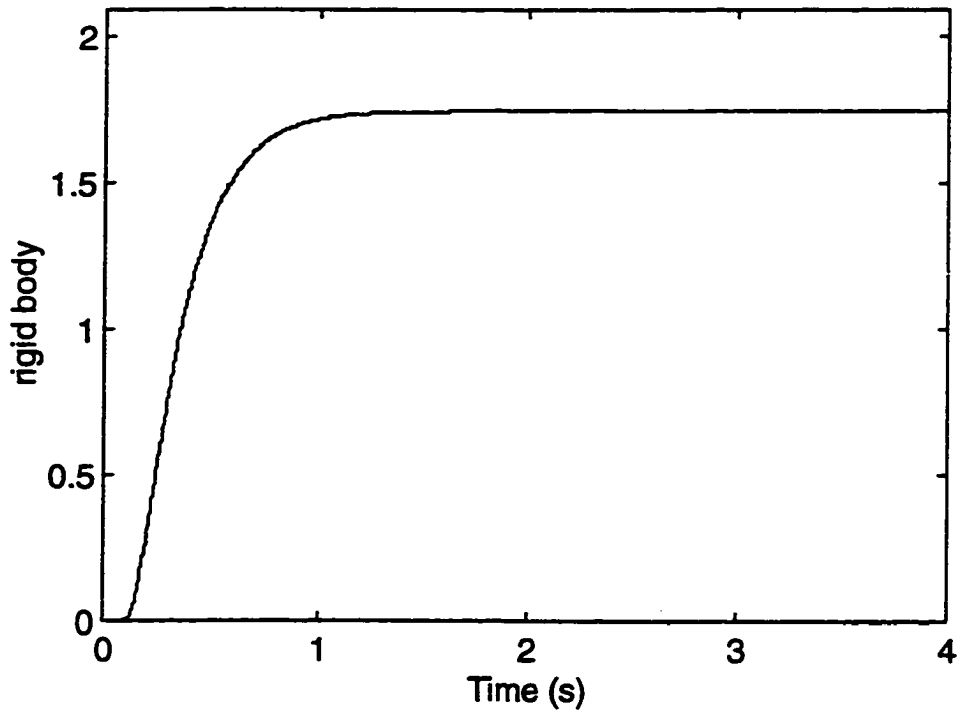

Figure 4-5 Simulated rigid body response under VSSMC control

Figure 4-6 shows that sliding surface value S decreases to and stays at zero, which indicates the system state space hits sliding surface and stays on it.

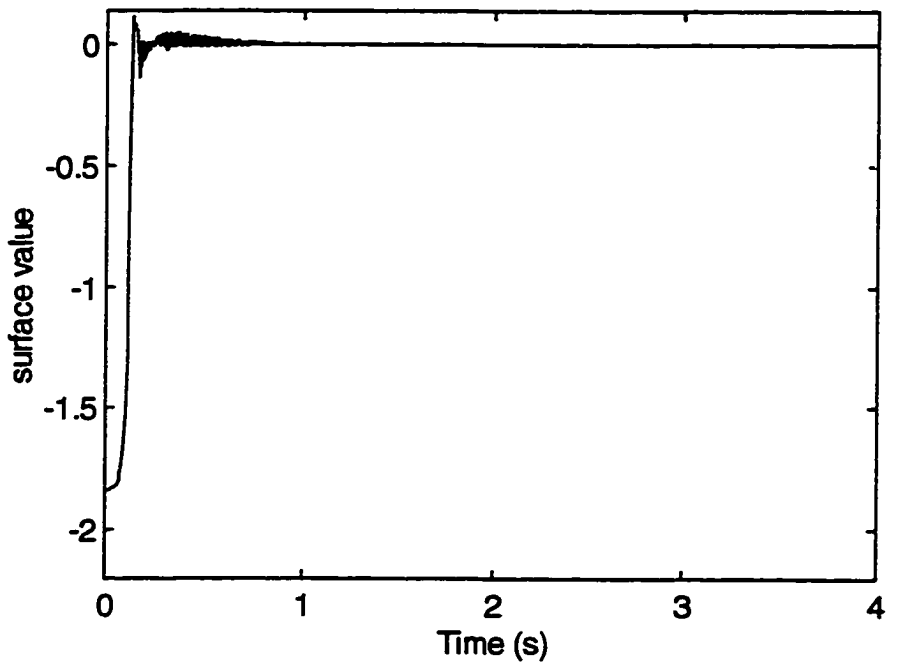

Figure 4-6 Sliding surface value decreases to and stays at zero in the VSSMC control

And simulation in Figure 4-7 shows how the VSSMC control design is realized in state space:

the system state starts from initial state (100° slew, both speed and acceleration are zeroes) and is driven to hit the sliding surface S as described in Equation 4-6, then it slides down to the origin (steady state) along the sliding surface.

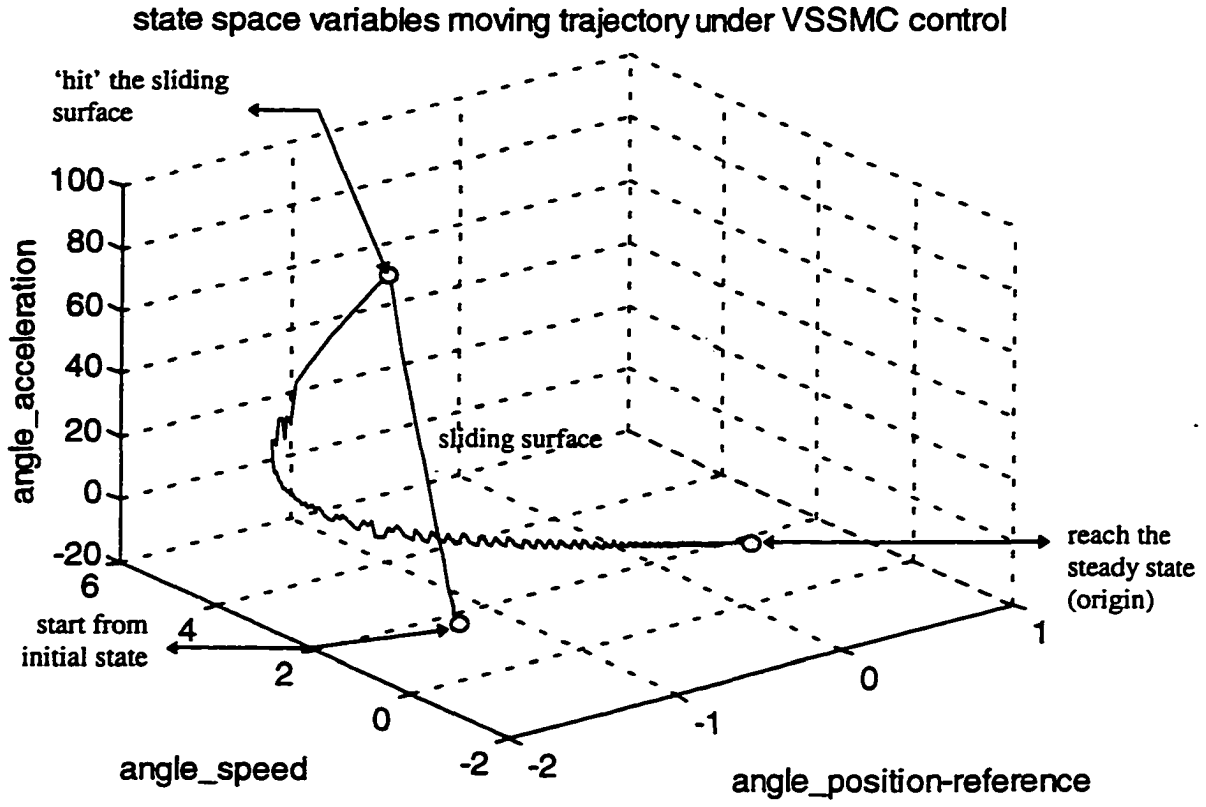

Figure 4-7 State space variables moving trajectory under VSSMC control

As Figure 4-5 indicates, rigid body reaches the steady state within about 1 second (faster than obtained by PIDP and LQR control) and develops no overshoot. This VSSMC design would have been a successful controller if the controller effort was feasible. Figure 4-8 shows the controller effort required to perform this control:

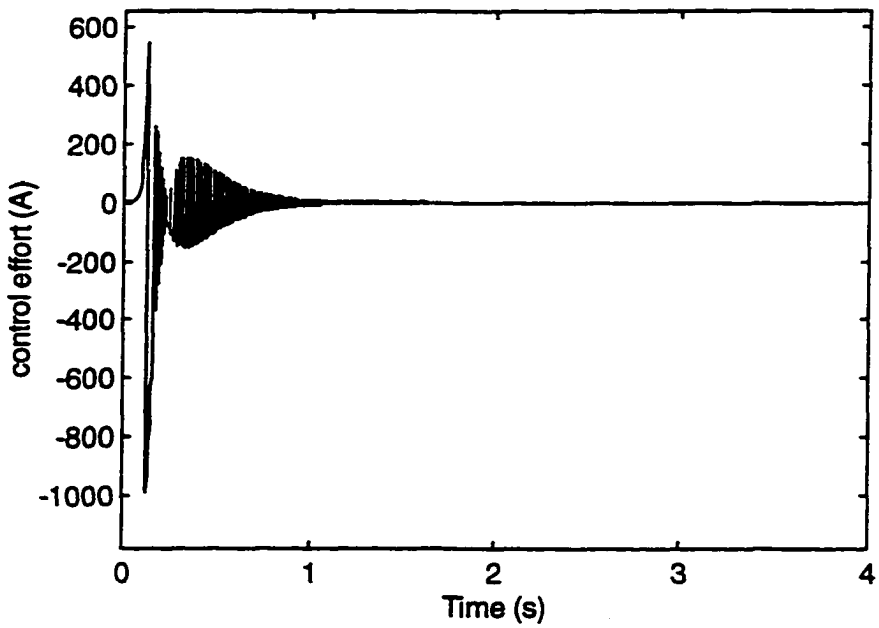

Figure 4-8 Simulated controller effort in VSSMC control

It can be seen in Figure 4-8 that the controller effect required is far beyond the motor current limit in our experimental apparatus. Since VSSMC does not show promise for experiments in our setup, it was not further developed for tip deflection/vibration control and was not experimentally implemented.

Chapter 5

Summary and Future Work

This thesis discusses the modeling and control of an experimental single flexible-link manipulator, and explores some important aspects which are not covered in the previous literature.

In this thesis, the model for flexible-link manipulator is developed. It describes both linear and nonlinear behaviors of the entire system. By comparing experimental results with simulations, this model is shown to be predictive of experimental results. More detailed exploration also reveals the change of model parameters in the presence of various payloads. This model's structure and the methods used to obtain this model can serve to model general cases of single flexible-link manipulators.

Based on this model obtained, PIDP control is presented in this thesis as a successful control strategy for rigid body trajectory tracking and deflection/vibration suppressing. This control method is based on the optimization of PD gains, conditional I gain and the use of a lowpass-filter before strain feedback. Experimental system performance under this PIDP controller shows better performance than obtained on such structures in previous literature.

A further improvement on PIDP control is considered by using LQR control. LQR algorithm suggests more stable and effective gains on 9 feedback variables. The experimental behavior is improved compared to PIDP control, particularly in the first mode deflection/vibration suppression.

Suggestions for future work:

- Improving system performance in terms of eliminating nonlinear effects, like gear backlash induced hitting and static friction, by using the nonlinear models obtained in this thesis;

- Fast and effective system identification for flexible-link manipulator to identify the presence of payloads. Typical changes of model parameters under payloads are revealed in Chapter 2. The results of Chapter 2 can also be used to design a simple robust PIDP controller or LQR controller or H-infinity controller over the entire range of payloads.

- If the performance obtained from the above while using a simple robust controller is not satisfactory then adaptive control in the form of gain scheduling should be tried. If the performance is still not satisfactory then further improvements using full adaptive control may be performed.

Bibliography

1. Tarn, T. J., Bejczy, A. K., and Ding, X., "On the Modeling of Flexible Robot Arms", *Technical Report SSM-RL-88-11*, Washington University, 1988 (Robotics Laboratory Report).

2. Cannon, R. H., and Schmitz, Jr. E., "Initial Experiments on the End-Point Control of a Flexible One-Link Robot", *The International Journal of Robotics Research*, Vol. 3, No. 3, Fall 1984.

3. Kotnik, P. T., Yurkovich, S., and Ozguner, U., "Acceleration Feedback for Control of a Flexible Manipulator Arm" *Journal of Robotics Systems*, 5(3), 1988.

4. Aoustin, Y., Chevallereau, C., Glumineau, A., and Moog, C. H., "Experimental Results for the End-Effector Control of a Single Flexible Robotics Arm", *IEEE Transactions on Control Systems Technology*, Vol. 2, No. 4, December 1994.

5. Thomas, S., and Bandyopadhyay, B., "Comments on 'A New Controller Design for a Flexible One Link Manipulator'", *IEEE Transactions on Automatic Control*, Vol. 42, No. 3, March 1997.

6. Qian, W.T. and C. C. H. Ma, "A New Controller Design for a Flexible One Link Manipulator", *IEEE Transactions on Automatic Control*, Vol. 37, No.1, January 1992

7. Smith, R. S., Chu, C.-C., and Fanson, J. L., "The Design of H_∞ Controller for an Experimental Non-Collocated Flexible Structure Problem", *IEEE Transaction on Control Systems Technology*, Vol. 2, No. 2, June 1994.

8. Marshall, B,, and Currie, K., "Flexible Robotics Arm" *B. Eng. Degree Project*, Lakehead University, 1997.

9. Yurkovich, S., Pacheco, F. E. and Tzes, A. P., "On-line Frequency Domain Information for Control of a Flexible-Line Robot with Varying Payload", *IEEE Transaction on Automatic Control*, Vol. 34, No. 12, December 1989.

10. Tzes, A. P. and Yurkovich, S., "Application and Comparison of On-line Identification Methods for Flexible Manipulator Control", *The International Journal of Robotics Research*, Vol. 10, No. 5, October 1991.

11. Tzes, A. P. and Yurkovich, S., "A Frequency Domain Identification Scheme for Flexible Structure Control", *Journal of Dynamic Systems, Measurement, and Control*, Vol. 112, September 1990.

12. Yurkovich, S. and Tzes, A, P., "Experiments in Identification and Control of Flexible-Link Manipulators", *IEEE Control Systems Magazine*, February 1990.

13. Doyle, J. C. et. al. "State-Space Solutions to Standard H_2 and H-infinity Control Problems", *IEEE Transaction on Automatic Control*, Vol. 34, No. 8, August 1989.

14. Yurkovich, S. and Pacheco, F. E., "On Controller Tuning for a Flexible-Link Manipulator with Varying Payload", *Journal of Robotics Systems*, 6(3), September 1989.

15. Natarajan, K. & Gilbert, A.F., "System Identification and PID Controller Tuning Using Bandpass filters", Canadian Journal of Chemical Engineering, Vol. 75, No.4, August 1997.

16. Canudas, C. de Wit, Olsson, H., Astrom, K.J., Lischinsky, P., "A New Model for Control of Systems with Friction", *IEEE Transactions on Automatic Control*, Vol. 40, No. 3, March 1995.

17. Hatch, J. E., "*Aluminum: Properties and Physical Metallurgy*", March 1984.

18. Omega Engineering, "*The Pressure, Strain and Force Handbook*", Vol 29, 1995.

19. Rovner, D.M. and Cannon, R.H., "Experiments toward on-line identification and control of a very flexible one-link manipulator", *International Journal of Robotics Research*, 6(4), 1987.

20. Rovner, D.M. and Franklin, G.F, "Experiments in load-adaptive control of a very flexible one-link manipulator", *Automatica*, 24(4), 1988.

21. Hastings, G.G and Book, W.J., "Experiments in optimal control of a flexible arm", *Proceedings of the 1985 American Control Conference*, Boston, MA, June 1985.

22. Hastings, G.G. and Book, W.J., "Verification of a linear dynamic model for flexible robotic manipulators", *Proceedings of the IEEE International Conference on Robotics and Automation*, San Francisco, CA, April 1986.

23. Atherton, P., "*Nonlinear Control Engineering*", ISBN 0-442-30486-2, Van Nostrand Reinhold Co. Ltd., 1982.

24. Nelder, J.A. and Mead, R., "A Simplex Method for Function Minimization", Computer Jou., 7, 1965.

25. Taylor, J. H. and Lu, J., "Robust Nonlinear Control System Synthesis Method for Electro-Mechanical Pointing Systems with Flexible Modes", Journal of Systems Engineering, May 1995.

ABOUT THE AUTHOR

Sicheng Yu was born in P.R.China in May 1974. He obtained Bachelor degrees majoring in both Electrical Machinery Engineering and Computer Science in July 1994. He came to Lakehead University as a MSc.Eng. candidate in September 1996. This thesis is submitted after 15 months in the Control Engineering Master program under Dr. Natarajan's supervision.

IMAGE EVALUATION TEST TARGET (QA-3)

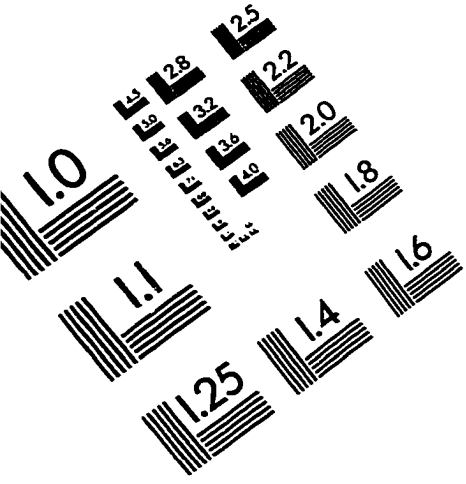

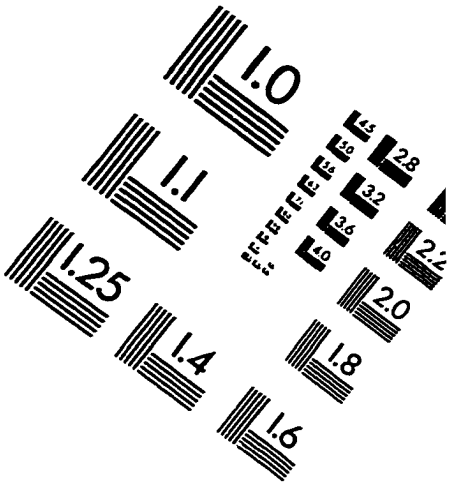

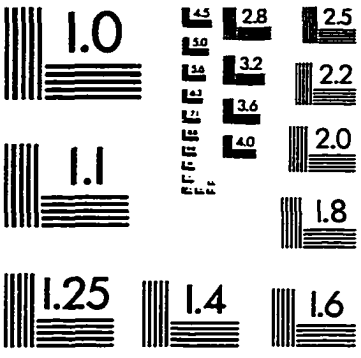

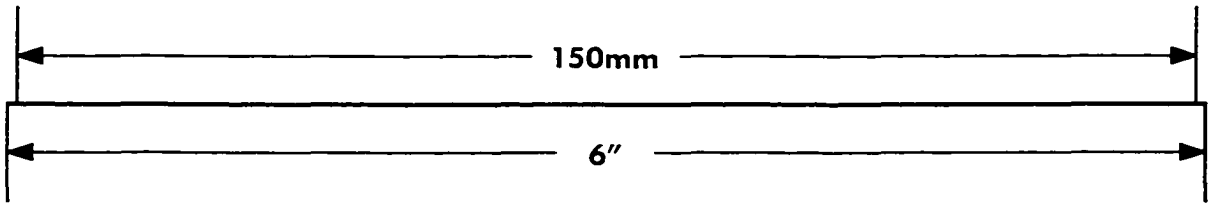

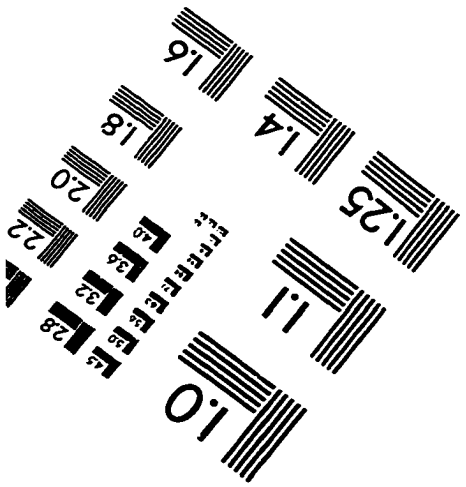

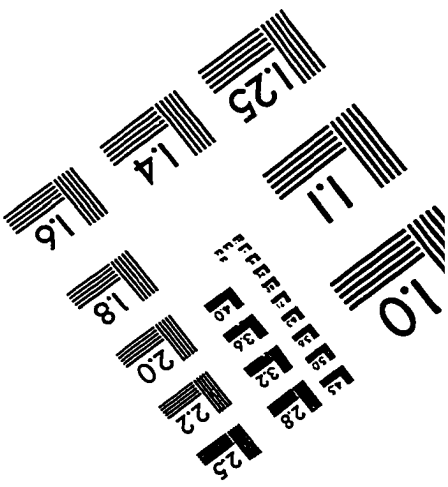

APPLIED IMAGE, Inc
1653 East Main Street
Rochester, NY 14609 USA
Phone: 716/482-0300
Fax: 716/288-5989